Improved Infrastructure Assessment through the Integration of Nondestructive Evaluation and Structural Health Monitoring Paradigms

PUBLICATION NO. FHWA-HRT-21-011

JANUARY 2021

U.S. Department of Transportation
Federal Highway Administration

Research, Development, and Technology
Turner-Fairbank Highway Research Center
6300 Georgetown Pike
McLean, VA 22101-2296

FOREWORD

Load rating, whereby the capacity of individual members is compared to dead-load and live-load demands, is one of the most common methodologies for evaluating the load-carrying performance of a bridge. This report provides methods for integrating both nondestructive evaluation data and field data from structural health monitoring to improve the accuracy and reliability of load ratings.

Cheryl Allen Richter, Ph.D., P.E.
Director, Office of Infrastructure
Research and Development

TECHNICAL REPORT DOCUMENTATION PAGE

1. Report No. FHWA-HRT-21-011	2. Government Accession No.	3. Recipient's Catalog No.
4. Title and Subtitle Improved Infrastructure Assessment through the Integration of Nondestructive Evaluation and Structural Health Monitoring Paradigms		5. Report Date January 2021 6. Performing Organization Code 1YX01
7. Author(s) Franklin Moon (ORCID: 0000-0003-3180-9120), John Braley (ORCID: 0000-0003-2058-3082), and Nenad Gucunski (ORCID: 0000-0003-3487-2782)		8. Performing Organization Report No.
9. Performing Organization Name and Address Engineering & Software Consultants, Inc. 14123 Robert Paris Court Chantilly, VA 20151 Rutgers, The State University of New Jersey 57 US Highway 1 New Brunswick, NJ 08901		10. Work Unit No. 11. Contract or Grant No. DTFH61-14-D-00011
12. Sponsoring Agency Name and Address Office of Infrastructure Research and Development Federal Highway Administration 6300 Georgetown Pike McLean, VA 22101		13. Type of Report and Period Covered Final Report; March 2019−June 2020 14. Sponsoring Agency Code HRDI-20
15. Supplementary Notes The Contracting Officer's Representative was Hoda Azari (HRDI-20; ORCID: 0000-0002-7340-0035).		

16. Abstract

This report provides recommendations for integrating both nondestructive evaluation (NDE) data and field data from structural health monitoring (SHM) to obtain load ratings that reliably represent a bridge's load-carrying performance. Modern NDE techniques, which provide accurate location and characterization of deteriorations, enable more reliable estimates of capacity. The existing *LRFD Bridge Design Specifications* provide detailed equations for determining the capacity of a given bridge member (AASHTO 2017). The dimensions or material properties used in these equations should be revised based on NDE results. Several common deterioration types are shown through analytical studies to have minor effects on the capacity of composite girder sections.

Demand estimates require structural analysis to translate globally applied loads to their corresponding member actions or force effects. The effects of local deterioration and defects on member demands were investigated through finite-element (FE) simulation and were shown to have negligible effect (<3 percent). However, an in situ structure may behave very differently than predicted by demand models. Field data from SHM may be leveraged to reduce the uncertainty associated with those demand models. The use of experimental distribution factors (introduced in this report) is shown to more reliably estimate demands compared to the methods provided by the *Manual for Bridge Evaluation* for incorporating results from diagnostic and proof-level load tests (AASHTO 2018). However, it is recommended that refined analysis with FE models be used when practical, as this method permits explicit consideration of all influential mechanisms.

17. Key Words	18. Distribution Statement
NDE, nondestructive evaluation, SHM, structural health monitoring, load rating, refined analysis, field data, diagnostic testing, proof testing, load testing	No restrictions. This document is available to the public through the National Technical Information Service, Springfield, VA 22161. http://www.ntis.gov

19. Security Classif. (of this report)	20. Security Classif. (of this page)	21. No. of Pages	22. Price
Unclassified	Unclassified	115	N/A

Form DOT F 1700.7 (8-72) Reproduction of completed page authorized.

SI* (MODERN METRIC) CONVERSION FACTORS

APPROXIMATE CONVERSIONS TO SI UNITS

Symbol	When You Know	Multiply By	To Find	Symbol
		LENGTH		
in	inches	25.4	millimeters	mm
ft	feet	0.305	meters	m
yd	yards	0.914	meters	m
mi	miles	1.61	kilometers	km
		AREA		
in^2	square inches	645.2	square millimeters	mm^2
ft^2	square feet	0.093	square meters	m^2
yd^2	square yard	0.836	square meters	m^2
ac	acres	0.405	hectares	ha
mi^2	square miles	2.59	square kilometers	km^2
		VOLUME		
fl oz	fluid ounces	29.57	milliliters	mL
gal	gallons	3.785	liters	L
ft^3	cubic feet	0.028	cubic meters	m^3
yd^3	cubic yards	0.765	cubic meters	m^3
	NOTE: volumes greater than 1,000 L shall be shown in m^3			
		MASS		
oz	ounces	28.35	grams	g
lb	pounds	0.454	kilograms	kg
T	short tons (2,000 lb)	0.907	megagrams (or "metric ton")	Mg (or "t")
		TEMPERATURE (exact degrees)		
°F	Fahrenheit	5 (F-32)/9 or (F-32)/1.8	Celsius	°C
		ILLUMINATION		
fc	foot-candles	10.76	lux	lx
fl	foot-Lamberts	3.426	$candela/m^2$	cd/m^2
		FORCE and PRESSURE or STRESS		
lbf	poundforce	4.45	newtons	N
lbf/in^2	poundforce per square inch	6.89	kilopascals	kPa

APPROXIMATE CONVERSIONS FROM SI UNITS

Symbol	When You Know	Multiply By	To Find	Symbol
		LENGTH		
mm	millimeters	0.039	inches	in
m	meters	3.28	feet	ft
m	meters	1.09	yards	yd
km	kilometers	0.621	miles	mi
		AREA		
mm^2	square millimeters	0.0016	square inches	in^2
m^2	square meters	10.764	square feet	ft^2
m^2	square meters	1.195	square yards	yd^2
ha	hectares	2.47	acres	ac
km^2	square kilometers	0.386	square miles	mi^2
		VOLUME		
mL	milliliters	0.034	fluid ounces	fl oz
L	liters	0.264	gallons	gal
m^3	cubic meters	35.314	cubic feet	ft^3
m^3	cubic meters	1.307	cubic yards	yd^3
		MASS		
g	grams	0.035	ounces	oz
kg	kilograms	2.202	pounds	lb
Mg (or "t")	megagrams (or "metric ton")	1.103	short tons (2,000 lb)	T
		TEMPERATURE (exact degrees)		
°C	Celsius	1.8C+32	Fahrenheit	°F
		ILLUMINATION		
lx	lux	0.0929	foot-candles	fc
cd/m^2	candela/m2	0.2919	foot-Lamberts	fl
		FORCE and PRESSURE or STRESS		
N	newtons	2.225	poundforce	lbf
kPa	kilopascals	0.145	poundforce per square inch	lbf/in^2

*SI is the symbol for International System of Units. Appropriate rounding should be made to comply with Section 4 of ASTM E380. (Revised March 2003)

TABLE OF CONTENTS

LIST OF FIGURES

LIST OF TABLES

LIST OF ABBREVIATIONS AND SYMBOLS

Abbreviations

AASHTO	American Association of State Highway and Transportation Officials
BEAST	Bridge Evaluation and Accelerated Structural Testing
DF	distribution factor
DOF	degrees of freedom
ER	electrical resistivity
FE	finite element
FEA	finite-element analysis
FEM	finite-element model
FHWA	Federal Highway Administration
GPR	ground penetrating radar
HCP	half-cell potential
IE	impact-echo
LiDAR	light detection and ranging
LRFD	Load and Resistance Factor Design
LTBP	Long-Term Bridge Performance
MBE	*Manual for Bridge Evaluation*
NDE	nondestructive evaluation
RAD	radiography
SHM	structural health monitoring
SLG	single-line girder
USW	ultrasonic surface wave

Symbols

#RatingLanes	number of lanes loaded for a load rating
A_d	area of deck
A_s	area of steel
A_{PS}	area of prestressing strands
C	capacity
D	girder depth
DC	dead-load effect due to structural components
$DF_{exp,i}$	experimental distribution factor for girder *i*
DW	dead-load effect due to wearing surface and utilities
Ec	concrete elastic modulus
EI	flexural rigidity
F_A	axial force
f'_c	compressive strength
F_u	ultimate tensile strength
F_y	yield strength
I	moment of inertia
IM	dynamic load allowance
K	adjustment factor

K_a	ratio of calculated strain to the strain recorded during load test
K_b	reduction factor
LL	live-load effect
M	applied moment
m	total number of design lanes loaded during load test
M_1	principle bending moment
M_C	composite moment
M_n	nominal moment capacity
$Multi\_Presence$	multiple presence factor
$Multi\_Presence_m$	multiple presence factor for m lanes loaded
M_y	moment at first yield of the bottom strands
n	the number of girders
P	permanent loads other than dead loads
P_d	plastic force in deck
P_{PS}	plastic force in prestressing strands
P_s	plastic force in steel
RF	rating factor
RF_C	theoretical rating
RF_T	revised load rating based on test results
R_i	the response of girder i during a test which loaded all lanes
$R_{i,j}$	the response of girder i during a test which loaded lane j
SB_{st}	short-term composite-section modulus for the bottom fiber
t_D	deck thickness
β	concrete property related to the depth of the stress block
γ_{DC}	load factor for structural components
γ_{DW}	load factor for wearing surface and utilities
γ_{LL}	live-load factor
γ_P	permanent-load factor
ε_C	strain at which concrete is assumed to crush
ε_c	calculated strain
ε_t	recorded strain
σ	stress
ϕ	curvature that results from an applied moment
ϕ_c	condition factor
ϕ_y	section curvature at yield
0.4L	location at a distance of 40 percent of span length from abutment

EXECUTIVE SUMMARY

Load rating, which compares the capacity of individual members to dead-load and live-load demands, is one of the most common methodologies for evaluating the load-carrying performance of a bridge. This report introduces methods for integrating both nondestructive evaluation (NDE) data and field data from structural health monitoring (SHM) to improve the accuracy and reliability of load ratings.

Modern NDE techniques, through accurate location and characterization of deteriorations, enable more reliable estimates of capacity. The existing *AASHTO LRFD (Load and Resistance Factor Design) Bridge Design Specifications* provides detailed equations for determining the capacity of a given bridge member (AASHTO 2017). The dimensions or material properties used in these equations should be revised based on NDE results. This approach contrasts with the *Manual for Bridge Evaluation* (MBE), which suggests reducing capacity by a factor that accounts for general condition (AASHTO 2018). Analytical studies have shown that several common deterioration types have minor effect on the capacity of composite girder sections.

Demand estimates require structural analysis to translate globally applied loads to their corresponding member actions or force effects. The influences of local deterioration and defects on member demands were investigated through finite-element (FE) simulation and were shown to have negligible effect (<3 percent). However, an in situ structure may behave very differently than predicted by demand models. Field data from SHM may be leveraged to reduce the uncertainty associated with those demand models. The MBE offers guidance for incorporating results from diagnostic and proof-level load tests (AASHTO 2018). However, its methods cannot account for any differences between observed and expected responses and fail to provide conservative estimates of load rating in cases where unreliable mechanisms are carrying load or causing a significant change in stress distribution. The use of experimental distribution factors (introduced in this report) is a preferred alternative as it only revises the load distribution assumptions inherent to the approximate analysis methods recommended by the *LRFD Bridge Design Specifications* (AASHTO 2017). However, even this method cannot always account for the effect of unreliable mechanisms on load distribution. Therefore, it is recommended that refined analysis with FE models be used when practical, as this method permits explicit consideration of all influential mechanisms.

CHAPTER 1. INTRODUCTION

Over the past two decades, as the bridge engineering profession has moved toward more objective and quantitative approaches to structural assessment, two complementary paradigms that focus on quantifying local and global condition and performance have emerged. In general, the local techniques fall under the nondestructive evaluation (NDE) umbrella and aim to characterize local material properties and identify material-level forms of deterioration or damage. The more global techniques are commonly referred to as "structural testing" or "structural health monitoring" (SHM) and generally focus on quantifying or identifying changes in system- and component-level behaviors, such as those associated with global load path, the distribution of component actions, or the distribution of stresses within critical cross sections. Although these two assessment strategies appear quite complementary in nature, there are few examples of how this complementary nature can be exploited to improve the accuracy and comprehensiveness of bridge assessment.

The overarching objective of the research reported herein was to develop, evaluate, and ultimately validate one or more integration strategies to leverage both NDE and SHM to improve bridge assessment. Currently, the most common approach for assessing the structural performance of a bridge is by performing a load rating, whereby the expected demands are compared to an estimated capacity. Due to its importance within current practice, this research adopted load rating as the guiding scenario for the research.

The *Manual for Bridge Evaluation* (MBE) is the current authority on bridge structural evaluation and load rating (AASHTO 2018). While these guidelines recommend that experimental data be considered in the load-rating process, the methods for integrating those data are arguably ill-defined and can result in ratings that are inaccurate and even nonconservative. A load rating would be considered nonconservative if the bridge it describes were to surpass limit-state conditions (e.g., yielding, failure) if subjected to the load for which it was rated. This could result in a dangerous scenario in which loads greater than the bridge can safely handle are permitted on the structure, possibly resulting in failure. This report highlights the inadequacies of the current methods as provided by the MBE and recommends alternative approaches for integrating NDE and SHM data to reduce uncertainty in demand and capacity models. This study also demonstrates these alternative methods in case studies of structures on which both NDE and SHM were performed.

CHAPTER 2. OVERVIEW OF APPLICATION SCENARIO

Load rating is the most common quantitative assessment activity undertaken by State transportation agencies throughout the United States and is required for every bridge per the "National Bridge Inspection Standards" (23 CFR 650 C). As such, it is highly relevant to current bridge engineering practices. Prior to embarking on research to integrate NDE and SHM data to improve load rating, it is first necessary to review common practices to better understand which aspects may benefit from specific data. Toward that end, it is useful to break bridge load rating into two activities: estimation of member demands and estimation of member capacities.

ESTIMATION OF MEMBER DEMANDS (FORCE EFFECTS)

Although it is common practice for demands to be defined at the system level (e.g., live loads, dead loads), load rating is generally carried out at the member, or component, level. This disconnect between scales requires the ability to relate globally applied loads to their corresponding member actions or force effects (e.g., moment, shear, axial, torsion, or stress). These activities fall within the realm of structural analysis and focus primarily on the quantification of load paths, which are influenced by applied loads (spatial distribution and location), boundary and continuity conditions, and member properties (material and geometric).

Given the uncertainty associated with these characteristics, many structural testing and SHM applications are geared toward improving the accuracy of this translation through various model updating schemes. These efforts often necessitated developing and validating various model calibration approaches. Over the last decade, significant advances have occurred in the areas of probabilistic methods (Cheung 2009; Asgarieh 2014; Christodoulou 2007) and multiple model methods (Dubbs 2015; Goulet 2010, 2013), but many are not compatible with current bridge engineering practices as they require specialized expertise and tools that are not economically feasible to deploy on a broad scale (e.g., load rating common bridge types). As a result, this research focused on evaluating the current state of the practice for model calibration as well as simple techniques that bridge engineering professionals may readily implement.

ESTIMATION OF MEMBER CAPACITY

The second requirement is to estimate member capacity, which is generally developed at the ultimate-strength limit state. Equations to compute member capacities are provided in the *LRFD (Load and Resistance Factor Design) Bridge Design Specifications* and are generally based on the mechanics of bridge materials (AASHTO 2017). Numerous destructive laboratory experiments have validated these equations over the last several decades. Although the uncertainty associated with these expressions (as well as variability in material properties) is addressed through resistance factors, guidance related to how to consider the influence of deterioration on a member's capacity is limited. One of the reasons for this is that assessments are generally carried out using visual inspection approaches as well as sounding, which are subjective in nature and may leave bridge engineers struggling to fully characterize deterioration.

Modern NDE techniques, however, have the potential to quantify the location and extent of common types of deterioration. These capabilities offer the opportunity to use state-of-the-art technologies to provide more accurate estimates of how deterioration influences capacity.

Importantly, because of the improved characterization of deterioration resulting from using these techniques, bridge engineering professionals may estimate capacity in a mechanistically consistent manner. That is, either the dimensions or material properties of the member can be updated to reflect the deterioration present and the capacity then calculated. This approach contrasts with the approach of reducing capacity by a factor that accounts for general condition, as discussed within the MBE (AASHTO 2018).

Furthermore, in many instances, construction documents, which typically provide member dimensions and material properties, are missing or fail to accurately represent the as-built conditions. In these cases, NDE techniques may assist bridge engineering professionals in quantifying both dimensions and material properties of the in situ structure.

CHAPTER 3. INTEGRATION OF FIELD DATA FOR DEMAND ESTIMATION

The integration strategies described in the following sections all aim to improve estimates of the demand (i.e., force effect) terms within the general load-rating equation shown in equation 1 (AASHTO 2018, section 6A.4.2.1):

$$RF = \frac{C - \gamma_{DC}DC - \gamma_{DW}DW \pm \gamma_P P}{\gamma_{LL}(LL + IM)} \quad (1)$$

Where:

RF = rating factor.
C = capacity.
DC = dead-load effect due to structural components.
DW = dead-load effect due to wearing surface and utilities.
LL = live-load effect.
IM = dynamic load allowance.
P = permanent loads other than dead loads.
γ_{DC} = load factor for structural components.
γ_{DW} = load factor for wearing surface and utilities.
γ_{LL} = live-load factor.
γ_P = permanent-load factor.

MANUAL FOR BRIDGE EVALUATION

The MBE allows for experimental data from a load test to be considered in the load-rating process by applying an adjustment factor (*K*) to the theoretical (a priori) rating as described by equation 2 (AASHTO 2018, section 8.8.2.3):

$$RF_T = RF_C K \quad (2)$$

Where:

RF_T = revised load rating based on load-test results.
RF_C = theoretical rating.
K = adjustment factor.

Adjustment factor *K* is given as the combination of two factors as described by equation 3:

$$K = 1 + K_a K_b \quad (3)$$

Where factor K_a is the ratio of the calculated strain (ε_c) to the strain recorded during the load test (ε_t), described by equation 4, and K_b is a reduction factor to account for the discrepancy between applied load levels and rating-load levels and the uncertainty in the assumption that the structure will behave linearly up to rating-load levels.

$$K_a = \frac{\varepsilon_C}{\varepsilon_t} - 1 \quad (4)$$

In short, this method compares measured test responses to predicted responses. The ratio of measured to predicted responses is assumed to be equal to the ratio of an initial load rating to the final updated load rating when K_b is equal to 1.0 (i.e., the test load is at least 70 percent of the gross rating load). Therefore, this method attempts to resolve inaccuracies in the demand model by assuming the error in experimental response predictions is directly proportional to the error in demand predictions at limit-state conditions. This method may be particularly nonconservative when the structure has mechanisms that contribute to its stiffness (and thus distribution of force effects), but such mechanisms may not always be active or their effectiveness may diminish over time or with increasing load levels, as demonstrated in this report. While reduction factor K_b is intended to account for mechanisms that cannot be depended upon at the rating-load level, it only considers the magnitude of the test load (relative to rating-load level). The MBE provides no means for identifying unreliable mechanisms or quantifying their load-carrying contribution.

The MBE allows for the theoretical rating (RF_C) of straight bridges to be determined using demands computed by the approximate methods as described by article 4.6.2 in the *LRFD Bridge Design Specifications* or by refined methods of analysis (AASHTO 2018, article 6A.3.2; AASHTO 2017). For common highway bridges, approximate methods would be employed. In such cases, member actions are determined by apportioning load to individual girders according to distribution factors and computing force effects (member actions) with a single-line girder (SLG) model. For the purposes of this report, SLG will signify demands or ratings computed using this method, while MBE will signify ratings that have been adjusted according to the manual's guidance for diagnostic load testing (AASHTO 2018).

REFINED ANALYSIS WITH CALIBRATED FINITE-ELEMENT MODEL

In some cases, the structure is too complex to be represented by single-girder behavior, or the measured responses are not strains due to known truck loads (e.g., natural frequencies) and therefore are unable to be used in the MBE methods for diagnostic load testing. In these cases, refined analysis with a finite-element model (FEM) is recommended. The process for refined analysis is well covered in the Federal Highway Administration (FHWA)-sponsored *Manual for Refined Analysis* (Adams 2019). The process for integrating SHM data through model calibration, however, is not covered.

Model calibration describes the process whereby parameters of an FEM are adjusted until simulated responses match measured responses (within a specified range). In many cases, the calibration process is more effectively performed with optimization algorithms. Parameters that are uncertain and influential to responses of interest should be chosen (e.g., material stiffness, element geometry, element connectivity, boundary conditions). In many cases, it may be beneficial to perform sensitivity studies to confirm that the chosen parameters appreciably influence responses of interest. The schematic shown in figure 1 describes the general steps for performing a refined analysis, including the model calibration and update process. Common response data used for model calibration and validation purposes include displacements,

rotations, strains, and dynamic characteristics such as frequencies and mode shapes that may be extracted from forced vibration testing or operational or ambient monitoring.

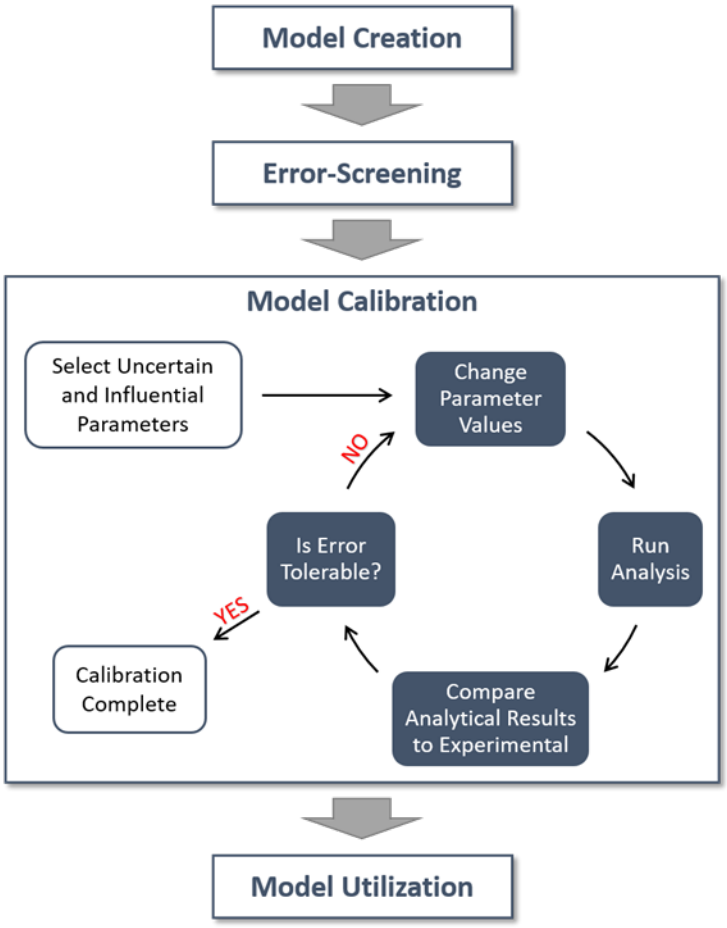

Source: FHWA.

Figure 1. Diagram. Activities and process for creating and applying a useful FEM.

The number of parameters to calibrate (e.g., material properties, dimensions, connections, boundary properties as well as their spatial variations) will always be greater than the number of measurements; therefore, the model is considered overparameterized, and, as a result, any number of calibrated models may be obtained. However, if a model is calibrated with data from a well-designed and executed field test, it may be expected to reduce the uncertainty associated with the estimation of load distribution and member-level demands.

The model-updating process may require multiple attempts and reconsideration of modeling decisions and included parameters. This trial-and-error process—reexamining the bridge system, reevaluating modeling decisions, and considering alternative parameters—can provide the most insight into the unique behavior of the structure.

There are numerous mechanisms that may provide stiffness and carry loads at the time of load testing that the owner may not wish to include in the load-rating analysis or whose effectiveness may diminish under different environmental conditions or after several years (e.g., composite

action between deck and girders, diaphragms, contributions of sidewalks and barriers, locked movement systems). Following calibration, the effects of these mechanisms may be excluded from simulations for the purposes of rating by negating the stiffness of corresponding elements or boundary conditions. Further discussion of the approach and methods of model calibration can be found in *Structural Identification of Constructed Systems: Approaches, Methods, and Technologies for Effective Practice of St-Id* (Çatbaş, Kijewski-Correa, and Aktan 2013).

EXPERIMENTAL DISTRIBUTION FACTORS (PROPOSED APPROACH)

For multigirder highway bridges, member demands are traditionally estimated by apportioning load to individual girders according to distribution factors (DFs) and computing force effects (member actions) with an SLG model. These factors are a function of bridge type, girder spacing, span length, and longitudinal stiffness. While this approach may be sufficient for design purposes as it offers conservative estimates, it presents challenges for how to use field-collected data to improve or validate its applicability.

For example, consider the situation where the LRFD DF for a specific girder estimates demands to be associated with 50 percent of a design lane. This estimate is likely conservative as the parametric studies used to generate the DF expressions could not address the specifics associated with all bridge configurations or load-carrying mechanisms and so were selected to represent an upper bound on demands. The problem arises when rating factors are corrected with field-collected data. In this case, let us assume that the measured responses indicated that the girder in question only experienced demands that would be expected from 25 percent of a design lane. Using the MBE method discussed previously, this would allow the engineer to double the load rating under the assumption that live-load demands can be reduced by a factor of two.

While this may appear reasonable at first, there is a significant danger in incorporating field-collected data in this manner. This danger arises from the lack of a requirement that would force the engineer to ensure the entire live-load demand considered for a bridge is accounted for. In the MBE method, the bridge is segmented into individual girders, but the sum total of demands on the girders is never checked to see if it indeed equals or exceeds the overall demands that arise from having each design lane loaded. In the example, this would occur if the bridge in question had two design lanes and five girders. In this case, the original demands accounted for 2.5 lanes loaded (i.e., 0.5 loaded lanes per girder times 5 girders), while the updated demands only account for 1.25 lanes loaded (i.e., 0.25 loaded lanes per girder times 5 girders). As illustrated in the case studies section of this report, lack of conservatism of this type is quite common when the current MBE approach to incorporating field-collected data is employed.

To mitigate these issues, the research team proposes an alternative approach that uses the field-measured data simply as a means of quantifying the relative load sharing between girders and then scales this distribution by the total demands considered for the bridge (as determined by the number of lanes and with appropriate multiple presence factors). Using this approach, the same rating calculations can be carried out, but with experimental DFs as opposed to theoretical DFs. Assuming linear behavior and loading locations similar to the load-rating scenario, these experimental DFs provide a much more reliable estimate of load distribution for an in situ structure as they ensure that the demands that arise from all design lanes (inclusive of appropriate multiple presence factors) are considered.

The way these factors are computed depends on the loading scenario under which the experimental data were obtained. If the data were obtained with all lanes loaded simultaneously (e.g., proof level), the experimental DF for each girder (*i*) would be computed according to equation 5:

$$DF_{exp,i} = \frac{R_i}{\sum_i^n R_i} * \#RatingLanes * Multi\_Presence \quad (5)$$

Where:

$DF_{exp,i}$ = experimental distribution factor for girder *i*.
n = number of girders.
R_i = response of girder *i* during a test which loaded all lanes.
#RatingLanes = number of lanes loaded for a load rating (AASHTO 2018, section 6B.6.2.2).
Multi_Presence = multiple presence factor (AASHTO 2017, section 3.6.1.1.2).

The ratio of girder *i*'s response to all girder responses (response ratio) shown in equation 5 must be multiplied by the number of lanes for which the bridge should be rated and the corresponding multiple presence factor.

If each lane is loaded separately (i.e., multiple load cases), $DF_{exp,i}$ may be computed by invoking linear superposition according to equation 6:

$$DF_{exp,i} = max\left[\sum_j^m \frac{R_{i,j}}{\sum_i^n R_{i,j}} * Multi\_Presence_m\right] \quad (6)$$

Where:

$R_{i,j}$ = response of girder *i* during a test which loaded lane *j*.
m = total number of design lanes loaded during load test.
$Multi\_Presence_m$ = multiple presence factor for *m* lanes loaded (AASHTO 2017, section 3.6.1.1.2).

Therefore, in the case of separate lane loading, the response ratios for each girder from the different load cases are summed to provide the total percentage of a single lane load that the girder would be expected to experience when all lanes are loaded (i.e., rating-load configuration).

These updated DFs retain all the conservatism built into the SLG approach to determining load rating and ensure 100 percent of the intended load is applied to the girders in the analysis. If the experimental DF of one or more girders differs significantly from other girders, there may be local loss of stiffness, and the structure should be investigated for damage.

CHAPTER 4. EVALUATION OF INTEGRATION STRATEGIES FOR DEMAND ESTIMATION

The goal of field-data collection for load rating is to characterize the distribution of stiffness and mass for the in situ structure accurately. However, in some cases, mechanisms that serve to stiffen the structure and carry load are not guaranteed to be reliable over the long term. It is therefore nonconservative to include these mechanisms in load ratings, and the MBE recommends that the stiffness contribution from nonstructural members not be relied on at ultimate load conditions (AASHTO 2018). The goal of this section is to evaluate how the three load-rating strategies discussed previously (i.e., the MBE approach for diagnostic load testing, refined analysis, and experimental DFs) perform in the presence of common, unreliable force-transfer mechanisms.

For illustrative purposes, the research team considered three common mechanisms. Depending on their specific details, barriers can have a significant impact on load distributions between girders, even though their contribution is generally ignored during rating calculations. Similarly, expansion bearings may be frozen and no longer permit longitudinal motion, but future events and large loading levels could free the bearings. Finally, a structure that is to be rated as noncomposite (between the deck and girder) will likely exhibit some level of composite action during field testing, even if only as a result of friction between the deck–girder interfaces.

These three mechanisms are not intended to be an exhaustive list of unreliable mechanisms; rather, they are some common examples that bridge engineering professionals might encounter on a multigirder highway bridge. Regardless of which mechanism might be encountered, its effect should be considered and excluded when performing a load rating. While this is relatively simple when estimating capacity, there is no clear guidance on how to do so when estimating demands.

The research team examined the effect of these mechanisms using a three-dimensional (3D) FEM. The team constructed element-level models for two notional designs (i.e., prestressed and steel multigirder) that were developed according to *LRFD Design Specifications* (2017) and have the following characteristics:

- Span length: 100 ft.
- Number of girders: 6.
- Girder spacing: 8 ft.

The research team load rated these notional structures for design-level loads (per HL-93, the current standard for design and evaluation) using both SLG analysis and refined analysis with element-level FEMs (AASHTO 2017, section Cl 3.6.1.2). The SLG analysis uses the methods outlined in the LRFD design manual, whereby the design load is apportioned to girders with DFs (AASHTO 2017). Rating factors were computed using this method for the strength and service-limit states (AASHTO 2018, section 6A.4.2.2) and for inventory and operating evaluation levels (AASHTO 2018, section 6A.4.3.2). The Strength I and Service II limit states were considered for the steel structure, while Strength I and Service III limit states were considered for the prestressed structure as recommended by the MBE (AASHTO 2018, section 6A.4.2.2). The

rating factors are summarized in table 1 and table 2 along with the DFs that were computed according to *LRFD Bridge Design Specifications* section 4.6.2.2 (AASHTO 2017). These DFs represent the portion of a lane load that should be applied to an individual girder in analysis for rating purposes.

Table 1. Base SLG rating factors for steel bridge.

Girder Location	Strength I: Inventory	Strength I: Operating	Service II: Inventory	Service II: Operating	DF
Interior	2.61	3.38	3.70	4.80	0.64
Exterior	1.85	2.40	2.62	3.41	0.90

Table 2. Base SLG rating factors for prestressed bridge.

Girder Location	Strength I: Inventory	Strength I: Operating	Service III: Inventory	DF
Interior	1.51	1.96	1.16	0.64
Exterior	1.37	1.78	1.06	0.71

The research team leveraged FEMs to investigate unreliable mechanisms by implementing or removing their effect in the models. Once the team had incorporated these mechanisms into the FEM, it was used to simulate a field test, and the resulting responses were treated as field-collected data. Table 3 shows the implemented configurations.

Table 3. Model configurations for studying the effects of unreliable mechanisms.

Case	Model Changes
Base FEM (in situ)	No changes (a priori)
Composite action released	Deck-girder links removed
Barrier stiffness turned off	Barrier modulus set to zero
Expansion bearings frozen	Longitudinal motion restrained at girder ends (pinned–pinned)

For each case, the team performed live-load simulations to produce maximum flexural response at midspan of the girders. These responses were assumed to be "field-collected" data and used to compute revised rating factors following each of the three methods described previously (MBE, refined analysis, and experimental DFs). Appendix C provides further information on FEM activities.

INFLUENCE OF NONCOMPOSITE STRUCTURE

To examine the influence of composite action, consider the situation where a bridge that one wishes to rate noncompositely is displaying composite action during field testing. As a result, the way the bridge resists loads during the test is different from what is assumed in the load-rating analysis. While the distribution of loads between girders is affected by this, the primary result is a significant drop in the force effects (e.g., bottom flange strain) for a given loading.

To examine the influence of this drop, the research team performed load ratings using the three methods outlined previously. The field-collected data (composite) responses were obtained from the base FEM (with composite links active and barrier stiffness on). Figure 2 through figure 4

present the resulting rating factors for each of the notional bridges (with the *x*-axis referring to the girder number). The refined analysis ratings shown in these figures are obtained with the FEM in which composite action was removed by releasing the links between the deck and girders in the longitudinal direction, permitting the nodes of the different elements to translate and rotate independently. Barrier stiffness was also removed from the FEM.

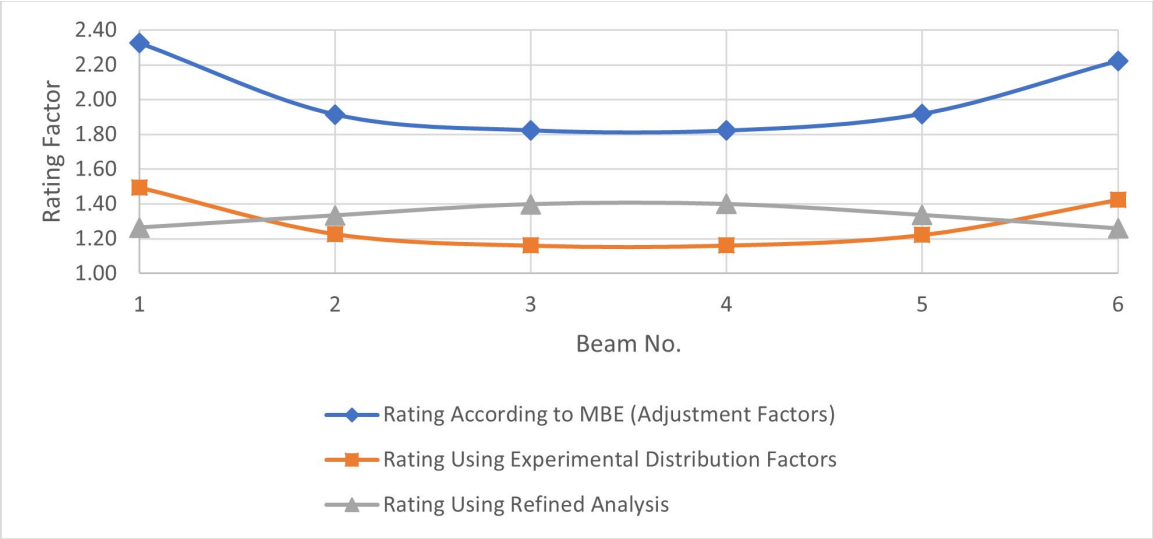

Source: FHWA.

Figure 2. Graph. Comparison of Strength I rating factors (inventory) for noncomposite prestressed bridge.

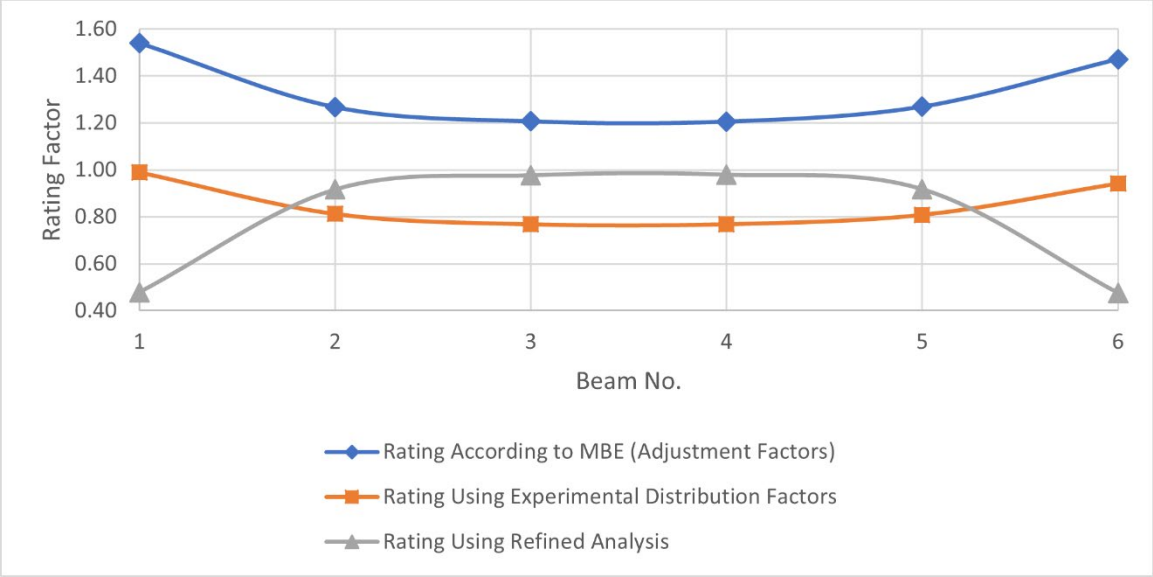

Source: FHWA.

Figure 3. Graph. Comparison of Service III rating factors (inventory) for noncomposite prestressed bridge.

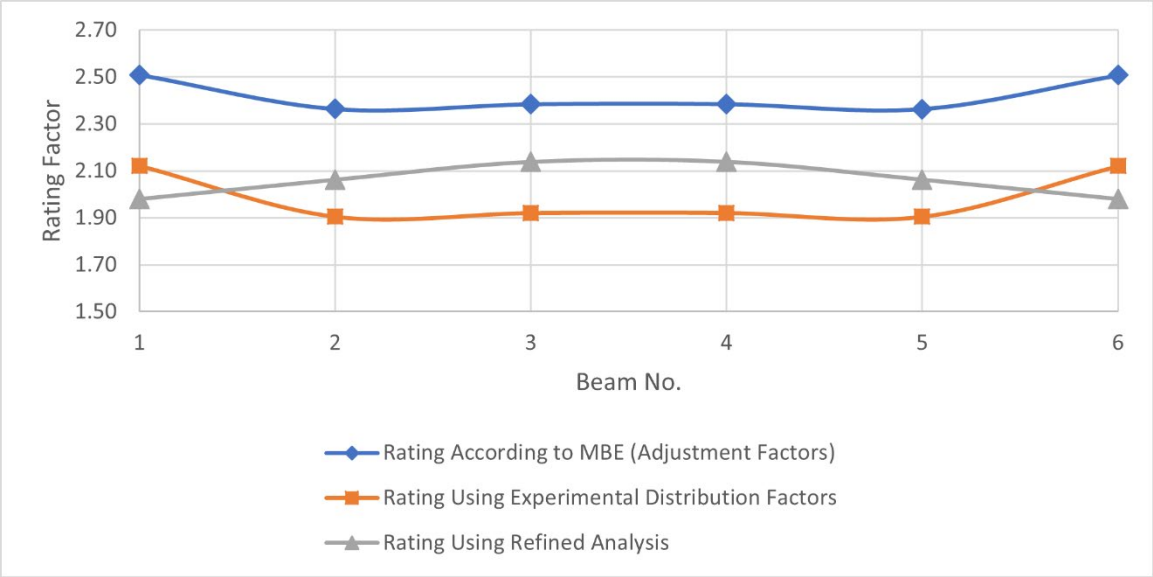

Source: FHWA.

Figure 4. Graph. Comparison of Strength I rating factors (inventory) for noncomposite steel bridge.

Figure 2 through figure 4 demonstrate the potential for the MBE method to overestimate the rating factors in this situation. While the change in load distribution does have some effect on load ratings (as evidenced by the difference between the refined-analysis rating and the experimental distribution-factor ratings) the majority of the nonconservatism of the MBE approach is due to the fact that a portion of the applied demands is not assigned to any of the girders. This over reduction of demands is due to the discrepancy between the assumed (noncomposite) strain distribution (through the height of the girder) used to compute theoretical responses and the actual (composite) strain distribution. The MBE approach has no ability to recognize or account for erroneous assumptions about the structure's behavior.

The discrepancy at exterior girders is due to the difference between barrier dead-load distribution of the FEM and the SLG assumptions. The SLG analysis assumes the barrier load is equally distributed to all girders, while FE simulation more realistically distributes the barrier load based on the stiffness of the structure. Therefore, the FE simulations will tend to apportion more of the barrier dead load to exterior girders. This effect is less pronounced with a structure that has other lateral-load-transfer mechanisms (e.g., diaphragms) that can more effectively distribute the barrier dead loads to interior girders, as seen in the steel ratings.

INFLUENCE OF INACTIVE BARRIERS

To examine the influence of barriers on the load-rating approaches, consider the situation where a bridge that one wishes to rate without the influence of barriers is experiencing barrier participation during field testing. As a result, the measured distribution and magnitude of responses are not consistent with the rating assumption that the barriers are inactive.

The research team performed a load-rating assessment to demonstrate the effect of barrier stiffness on load distribution and the ability of the integration methods previously discussed to

properly account for this effect. The in situ responses were obtained from the base FEM (i.e., fully composite and barrier stiffness on). The team computed ratings using the MBE method as well as with experimental DFs. The team also computed ratings by refined analysis, with responses obtained from a model in which the barriers were removed by setting their modulus of elasticity to 5 psi. Figure 5 through figure 7 illustrate the results.

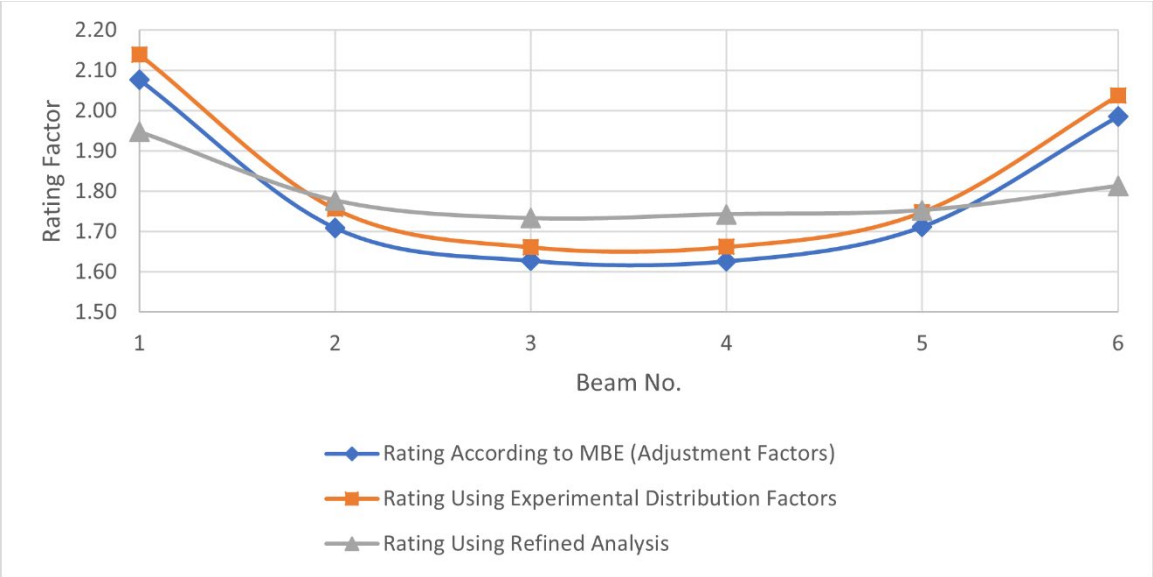

Source: FHWA.

Figure 5. Graph. Comparison of Strength I rating factors (inventory) for prestressed bridge with barriers.

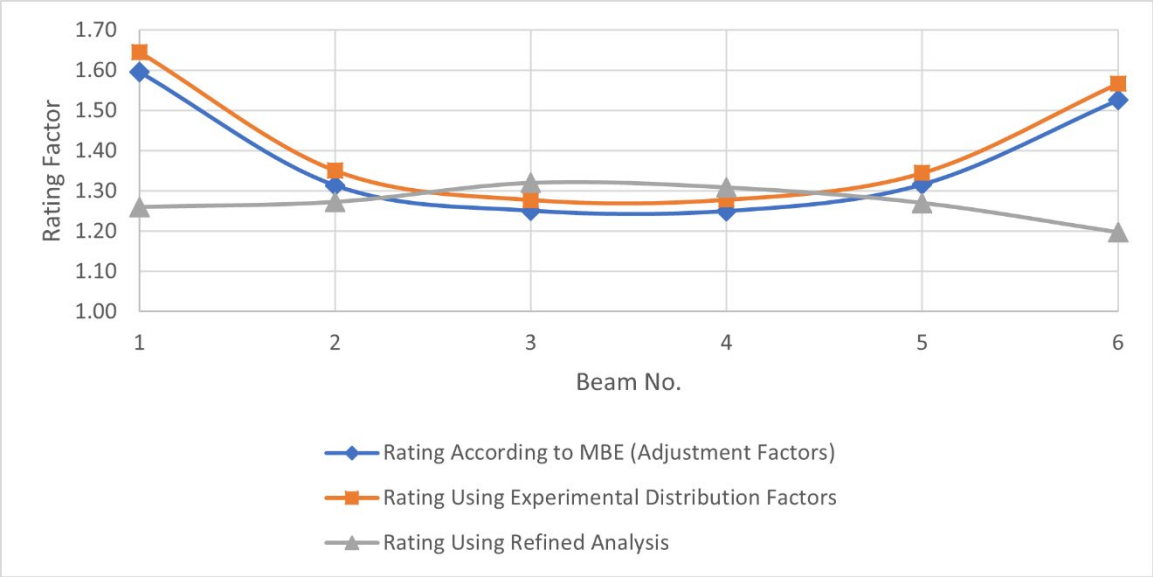

Source: FHWA.

Figure 6. Graph. Comparison of Service III rating factors (inventory) for prestressed bridge with barriers.

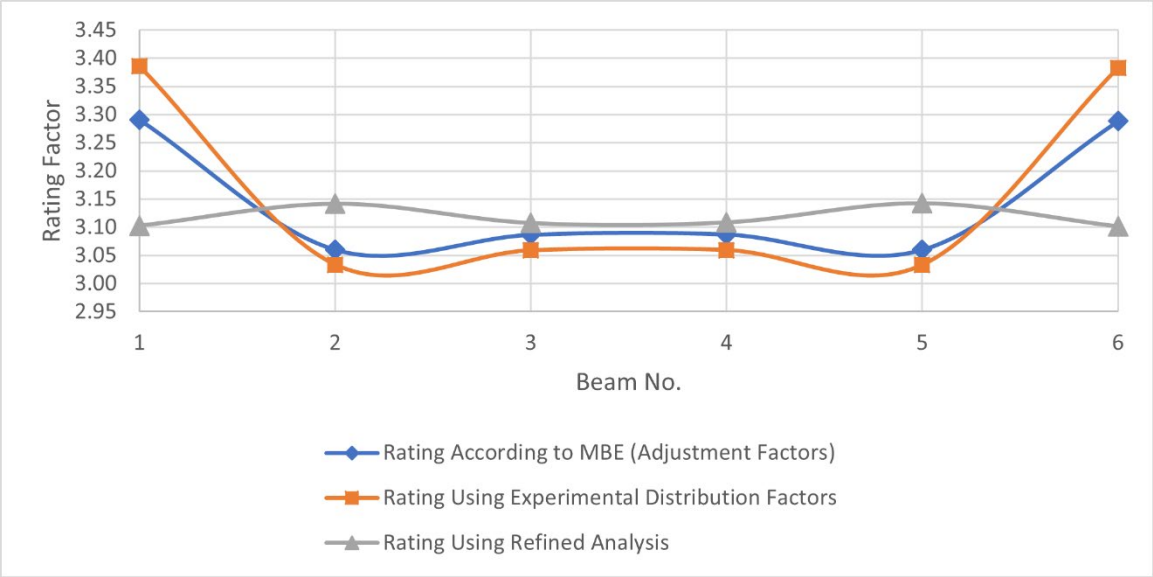

Source: FHWA.

Figure 7. Graph. Comparison of Strength I rating factors (inventory) for steel bridge with barriers.

Figure 5 through figure 7 reveal that barrier stiffness has a relatively minor effect on ratings for interior girders. The effect of exterior girders on the ratings is conflated with the assumption in SLG analysis that barrier dead load is equally distributed to all girders. This assumption has the potential to result in nonconservative ratings for exterior girders and slightly conservative ratings for interior girders for both the MBE method and the experimental DF method (assuming the FE representation is consistent with the actual performance of the bridge) as neither method is able to negate the effect of a component that is contributing stiffness at the time of testing. While these analyses used barriers of typical size and stiffness, the effect would be even more pronounced with larger, stiffer barriers.

INFLUENCE OF FROZEN BEARINGS

To examine the influence of frozen bearings on load-rating approaches, consider the situation where a bridge with idealized support conditions (both expansion and fixed) that one wishes to rate has frozen bearings that restrain longitudinal expansion due to bending. The primary challenge with this mechanism is that this restraint to longitudinal displacement results in a net compression on the girder cross section when it is loaded. As a result, bottom flange strain (which is the most common response captured and used for rating purposes) can be drastically reduced by the presence of this net compression.

Figure 8 shows the boundary conditions for minimal restraint. The research team implemented these conditions for ratings using refined analysis. Figure 9 depicts the boundary conditions implemented to simulate frozen bearings. In these conditions, all girders have longitudinal translation restrained (in addition to minimum restraints). Boundary conditions were applied to nodes located at the ends of the girders and at the bottom of the bottom flange to be consistent with bearing locations. The in situ (frozen bearings) responses were obtained from an FEM with fully composite action and fully active barriers (in addition to frozen bearing restraint).

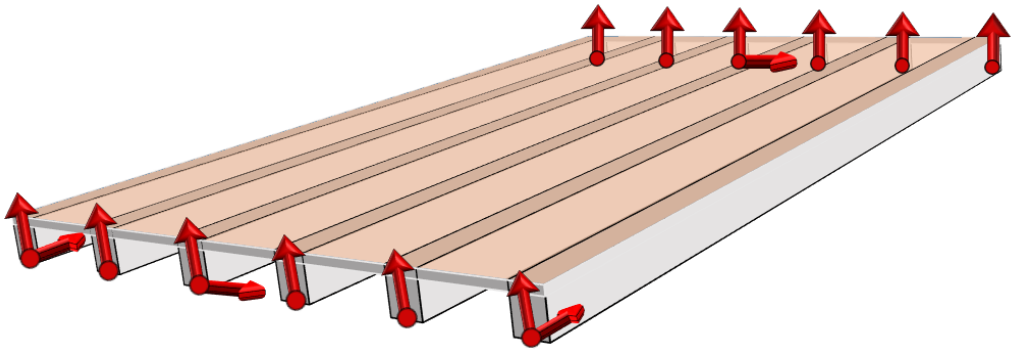

Source: FHWA.
Note: Arrows indicate direction of translational restraint.

Figure 8. Illustration. Boundary conditions for minimal restraint.

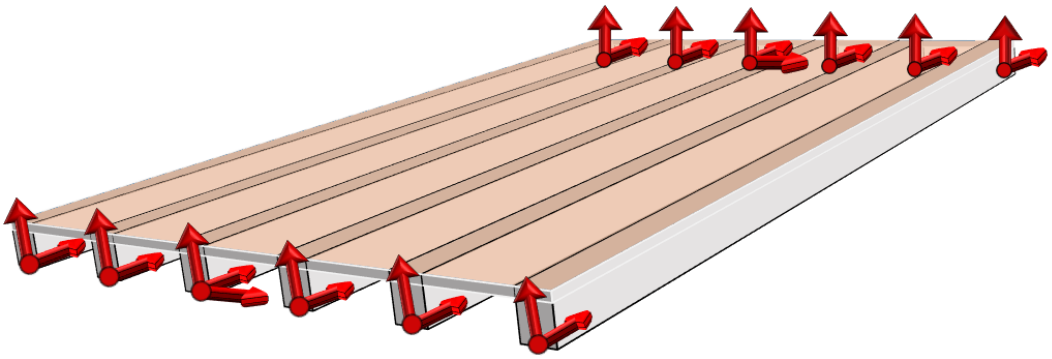

Source: FHWA.
Note: Arrows indicate direction of translational restraint.

Figure 9. Illustration. Boundary conditions for frozen bearings.

Figure 10 through figure 12 show the effects of frozen bearings on rating factors.

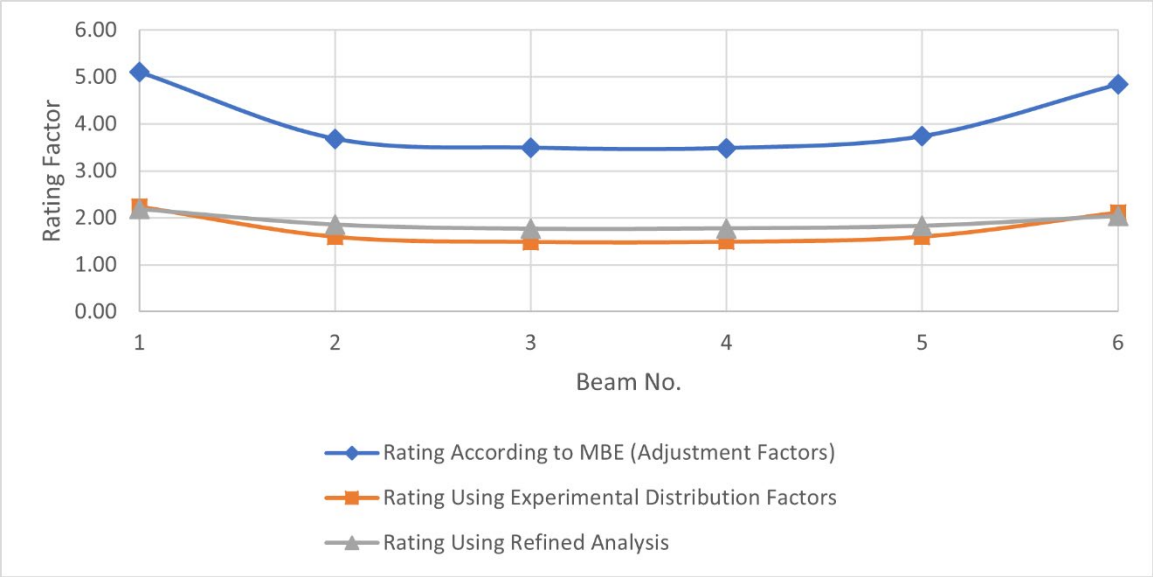

Source: FHWA.

Figure 10. Graph. Comparison of strength rating factors for prestressed bridge with frozen bearings.

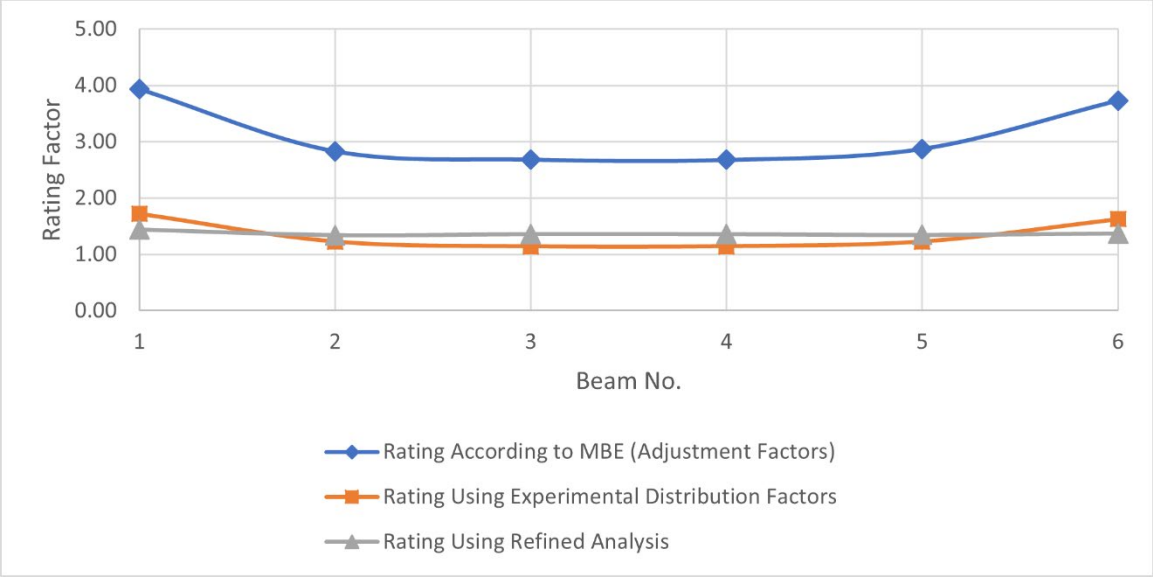

Source: FHWA.

Figure 11. Graph. Comparison of Service III rating factors for prestressed bridge with frozen bearings.

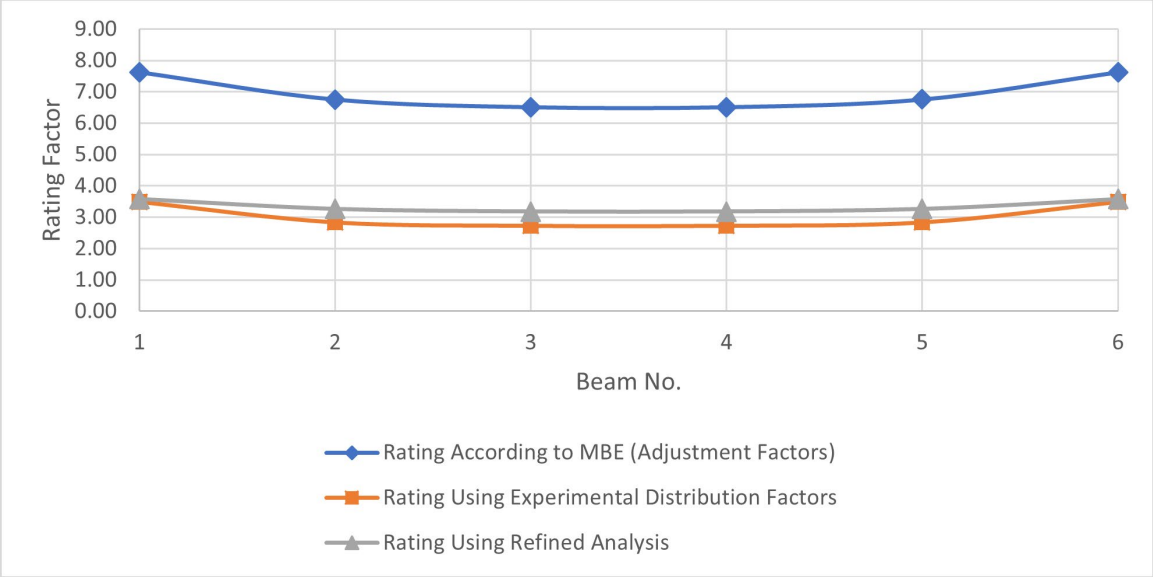

Source: FHWA.

Figure 12. Graph. Comparison of strength rating factors for steel bridge with frozen bearings.

The method provided in the MBE offers no means of negating this effect and will, in general, produce nonconservative results. This effect is primarily due to the assumed strain distribution which assumes the stress is only due to applied moment while the actual strain distribution includes net compression (in addition to bending moment). Experimental DFs, however, are much less susceptible to this type of error as the relative responses are scaled to ensure the entire load applied to the bridge is assigned to a girder.

INFLUENCE OF LOCALIZED DETERIORATION

The research team also investigated the influence of local deterioration on demands to determine if there might be a valid strategy for integrating NDE data into demand estimation. Using the 3D FEMs of the two notional designs, the team performed a series of sensitivity studies to evaluate the influence of local deterioration on demands. Appendix C contains further details about these models. The team examined the following types of deterioration:

- Deck surface delamination.
- Local loss of composite action (associated with significant deck deterioration).
- Loss of prestressing strands.

Deteriorations were simulated by changing the properties of appropriate elements, including geometry and material properties (i.e., modulus of elasticity).

Deck delaminations were simulated by reducing the thickness of the deck in a localized area by an amount corresponding to the delamination depth. Delaminations were positioned over exterior girders (centered), between the exterior and first interior girder, and over the first interior girder (centered). Delaminations with an 8-ft width and 8-ft length, as well as 40-ft length, were considered.

Loss of composite action (on a compositely designed structure) was simulated by removing the stiffness of elements (i.e., links) that enforced longitudinal compatibility between the girder elements and deck elements. Composite action loss was simulated at the ends of girders (at one-third of the length) for single girders (i.e., interior and exterior), half of the girders, and all girders.

The loss of prestressing strands serves to reduce the stiffness of the girder as the corresponding steel area no longer contributes to the section's flexural rigidity. Therefore, the research team investigated the effect of girder stiffness (i.e., moment of inertia) as a proxy for loss of prestressing. Appendix C contains the details of this and the other studies that examined the effect of local deteriorations on demands.

The following plot summarizes the worst-case effects of local deterioration on member demands. In many cases, deterioration serves to shift load away from the affected area. In these cases, adjacent girders present the worst-case scenario as they would experience an increase in demands.

Figure 13 shows that composite action is the only one of the three defects that significantly increases demands. However, loss of composite action softens the longitudinal stiffness of the girder section and shifts load to adjacent girders that remain composite. The degree of composite action cannot be directly measured, and thus the effect on load distribution is best determined through field testing (or FE simulation).

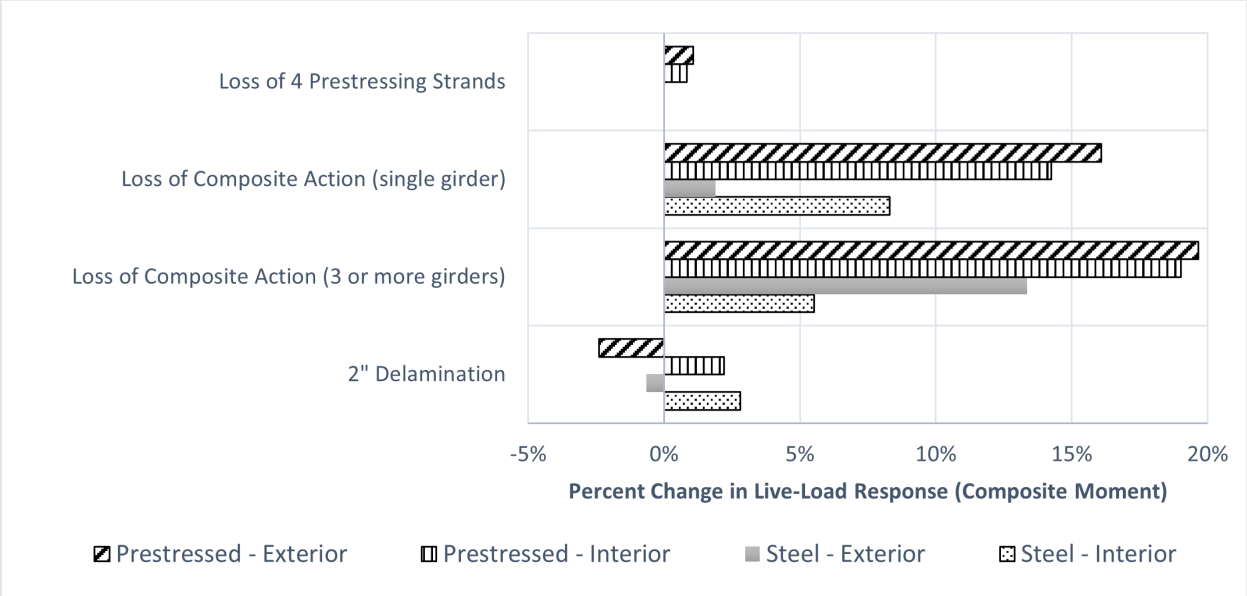

Source: FHWA.

Figure 13. Chart. Maximum effect of deterioration on girder flexural demands.

Therefore, the research team's investigations concluded that the type and extent of defects commonly detected and characterized through NDE techniques are not likely to have significant effect on member demands or load distribution. Ultimately, SHM techniques (e.g., load testing, dynamic testing, operational monitoring, and others) can more effectively capture the load

distribution characteristics of an in situ structure and are recommended for reducing uncertainty in demand models. Characterization of local deteriorations is still important for estimating capacity and remaining service life.

SUMMARY OF DEMAND ESTIMATION FINDINGS

Figure 14 and figure 15 summarize the difference between the MBE approach and the experimental DF method. A positive percentage represents the error of the load ratings relative to those determined using refined analysis; therefore, a positive percentage is considered nonconservative (i.e., overestimating reserve capacity), while a negative percentage is conservative.

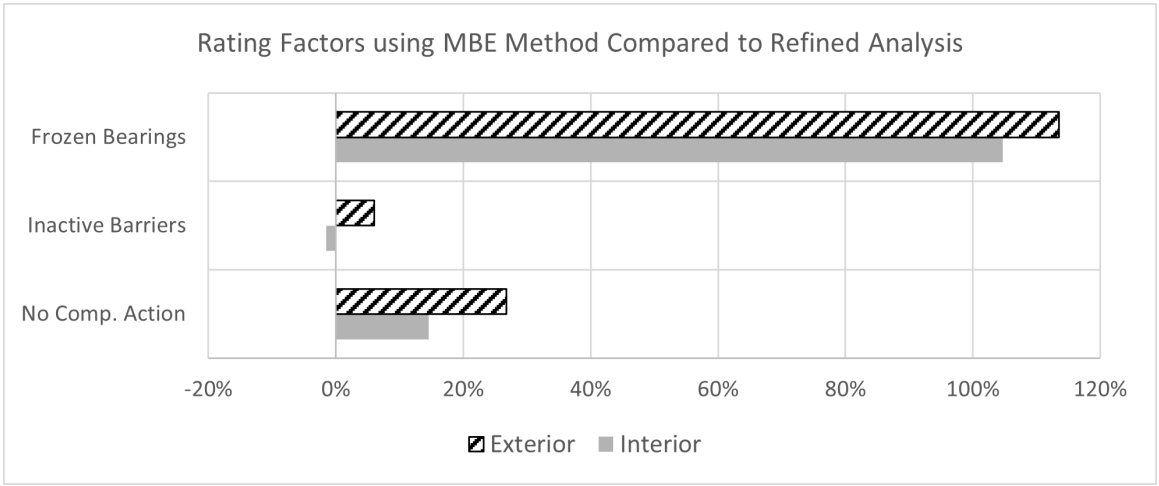

Source: FHWA.
Comp. = composite.

Figure 14. Chart. Performance of MBE methods for load rating with unreliable mechanisms.

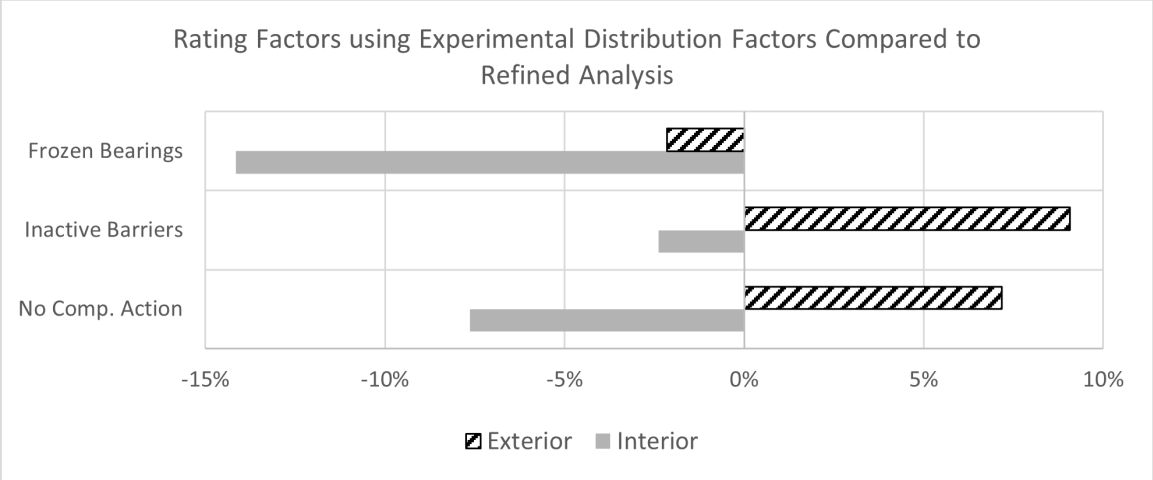

Source: FHWA.
Comp. = composite.

Figure 15. Chart. Performance of experimental DFs for load rating with unreliable mechanisms.

The MBE explicitly states that stiffness contribution from nonstructural members should not be relied on at ultimate load conditions; however, MBE methods cannot account for any differences between observed and expected responses and fail to provide a conservative estimate of load rating in cases where unreliable mechanisms are carrying load or causing significant change in stress distribution (AASHTO 2018).

Use of experimental DFs is a better alternative as it only revises the load distribution assumptions inherent to the SLG analysis method; however, even this method cannot account for the effect of unreliable mechanisms on load distribution. This shortcoming is especially seen in the exterior girders, where any global softening serves to increase load distribution to exterior girders. Therefore, it is recommended that refined analysis with FEMs be used when possible as this method permits explicit consideration of all influential mechanisms.

CHAPTER 5. INTEGRATION OF NDE IN CAPACITY ESTIMATION

NDE technologies and data types are numerous. However, many of them (indirectly) measure material properties (e.g., modulus of elasticity), geometry (e.g., deck thickness, location of reinforcing), or defects (e.g., delaminations, voids), which are just local deviations in material property or geometry. Therefore, many of the NDE technologies are well suited to informing capacity estimation.

The existing LRFD specifications provide detailed equations for determining the capacity of a given bridge member (AASHTO 2017). The section and material properties may be revised based on NDE results and the member capacity recalculated. Extensive simulation studies, presented in the following section and appendix B, showed that the standard capacity equations can adequately account for deteriorations in this manner.

For instance, the plastic moment capacity is calculated as the moment of the plastic forces about the plastic neutral axis. The plastic forces are a function of material strength and geometry. If NDE results indicate deviations of either from assumed values, they may simply be revised accordingly.

The list of NDE technologies presented in table 4, while not exhaustive, includes those in common use on bridges at the time of this report. Each technology is paired with a material or section property that may be revised should results indicate that in situ values differ significantly from a priori values.

Table 4. NDE technologies and corresponding integration parameters.

Technology	Result	Integration Parameter
Ultrasonic surface waves	Concrete modulus of elasticity	Concrete compressive strength[1]
Hammer sound and chain drag	Delaminations	Deck thickness
Impact echo	Delaminations	Deck thickness
Ultrasonic pulse echo	Voids, delaminations, thickness of concrete	Area of concrete
Ground-penetrating radar (GPR) for detecting delaminations	Delaminations and voids	Area of concrete
Infrared thermography	Delaminations and voids	Area of concrete
Radiography (RAD) for detecting voids	Voids	Area of concrete
GPR for locating reinforcement	Reinforcement location	Composite section properties
Magnetometer	Reinforcement location	Composite section properties
Magnetic flux leakage	Corrosion and breakage of prestressing strands	Reduction of strand area
RAD for profiling tendons	Strand and tendon locations	Location and area of steel
Ultrasonic testing (UT)	Material thickness (steel)	Area of steel (section geometry)

Source: FHWA (2015).

[1]No correlation factors currently exist between modulus values obtained from ultrasonic surface waves (USWs) and the compressive strength of concrete. While the results of USW testing are representative of the concrete elastic modulus (*Ec*), care must be taken in interpreting the specific values. In general, a USW estimated *Ec* is approximately 20–30 percent higher than the *Ec* determined through standard ASTM tests. This difference is primarily a result of the low strain levels imposed by USW testing. If future research were to identify a relationship between USW-estimated modulus and compressive strength, then it may be directly incorporated (with an appropriate consideration of uncertainty) to update capacity equations.

The MBE accounts for the effect of material degradation on capacity with a general condition factor (table 5) (AASHTO 2018). The shortcoming with this approach is that it does not explicitly consider the location of the degradation (e.g., steel web versus steel flange), which can have a significant influence over how it impacts capacity.

Table 5. LRFD condition factors.

Structural Condition of Member	ϕ_c
Good or satisfactory	1.00
Fair	0.95
Poor	0.85

ϕ_c = condition factor.

To overcome this shortcoming, NDE techniques aim to quantitatively estimate geometry and material properties that can be used directly within the capacity expressions (and thus account for the location of the degradation). This approach is consistent with the MBE's recommendation to consider deterioration when determining the resistance of a section by using the "gross cross section less that portion which has deteriorated" (AASHTO 2018, section C6.1.2).

In some cases, including NDE data may result in an increase in the capacity estimate. Even a structure that appears in poor condition may be shown through NDE to retain nearly all its capacity depending on the specific location of the deterioration, as demonstrated in appendix B. However, it may be necessary to retain the use of condition factors to account for the likely increase in future deterioration of components.

CHAPTER 6. EVALUATION OF NDE INTEGRATION STRATEGIES

The research team performed sensitivity analyses to evaluate the influence of local deterioration (e.g., deck delaminations) on capacity. For this application, the team used a cross-sectional model termed a "fiber model." This model is commonly used for nonlinear flexural analysis of complex cross sections, which it handles by discretizing the cross section into several elements referenced to specific stress–strain models. By incrementally increasing the curvature on the cross section while maintaining a linear strain profile (plane-sections-remain-plane) and iterating until equilibrium is satisfied, researchers obtained a nonlinear moment–curvature response.

This simple yet robust model is capable of simulating the nonlinear flexural behavior (in terms of both force and deformation) of general cross sections composed of multiple materials; however, it requires the use of an assumed strain profile and cannot directly simulate 3D behaviors. The schematic in figure 16 shows a section of multigirder composite bridge with a cross-sectional cut. Figure 17 provides a closer look at the fiber cross section, where all the girder and deck elements are meshed into finer 2D elements. Appendix B contains further details about this numerical model.

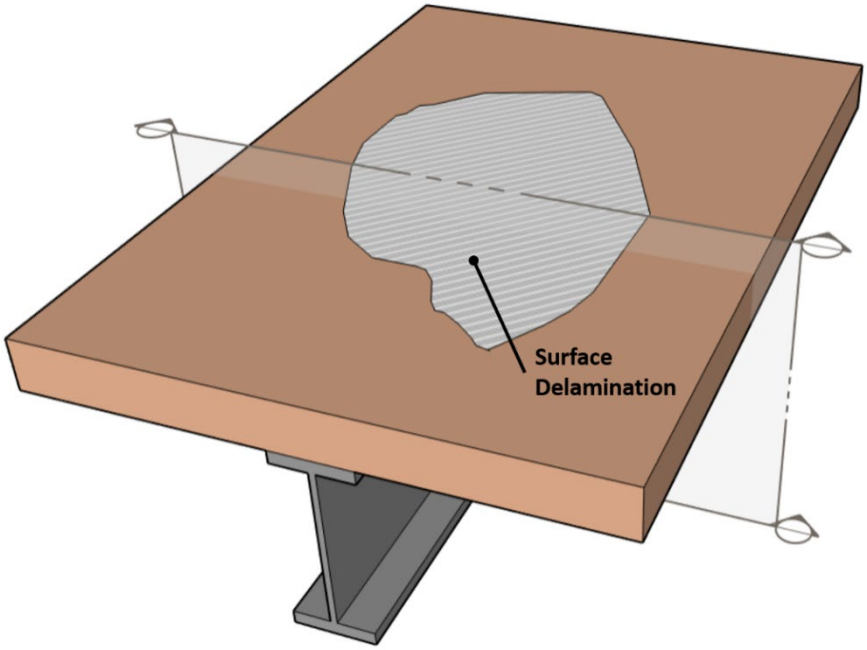

Source: FHWA.

Figure 16. Illustration. Composite section member.

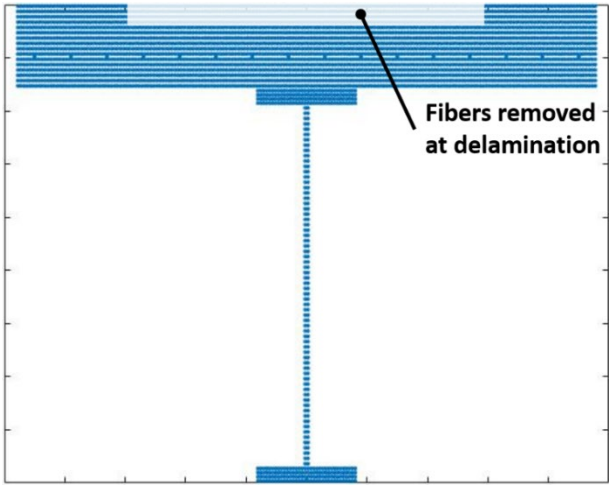

Source: FHWA.

Figure 17. Illustration. Meshed fiber cross section (at cut).

Delaminations were implemented in the fiber models by reducing the deck thickness by an amount equal to the depth of delamination, thereby removing elements within the delamination area. The research team investigated delaminations over the full effective width and up to 4 inches.

The team computed this change in ultimate moment due to delamination for each section. Figure 18 and figure 19 illustrate the effect of delamination on ultimate moment capacity.

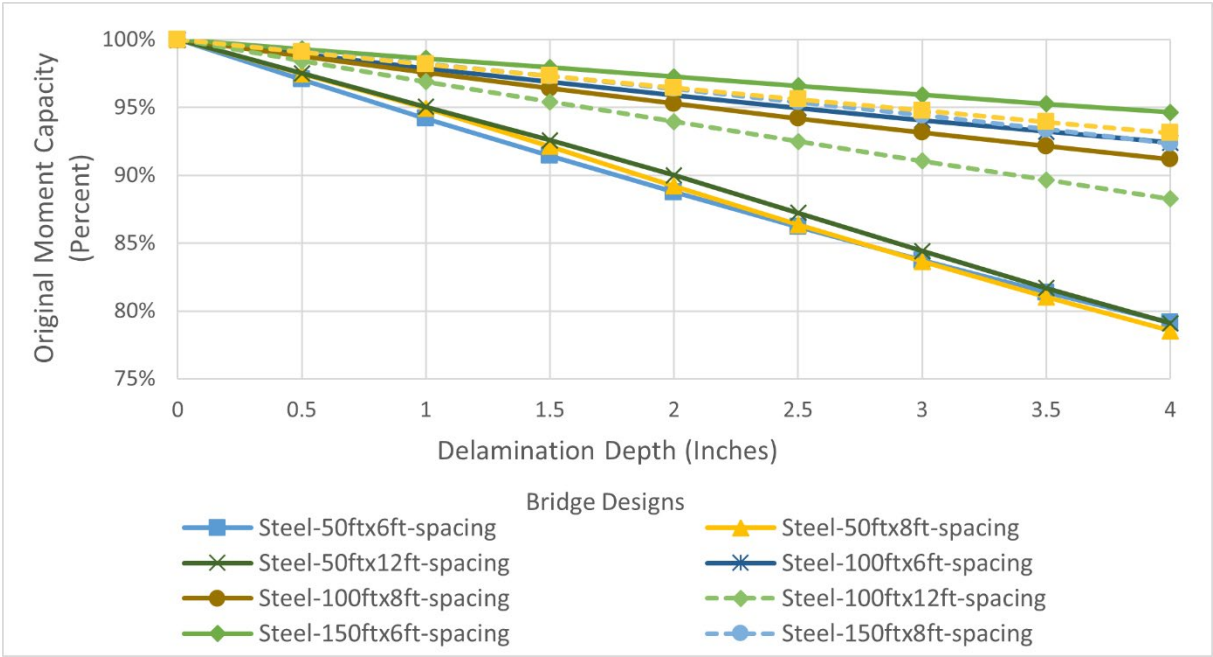

Source: FHWA.
Note: Vertical axis is abbreviated to enable visual discernment of series.

Figure 18. Graph. Effect of delaminations on ultimate moment capacity for steel composite sections.

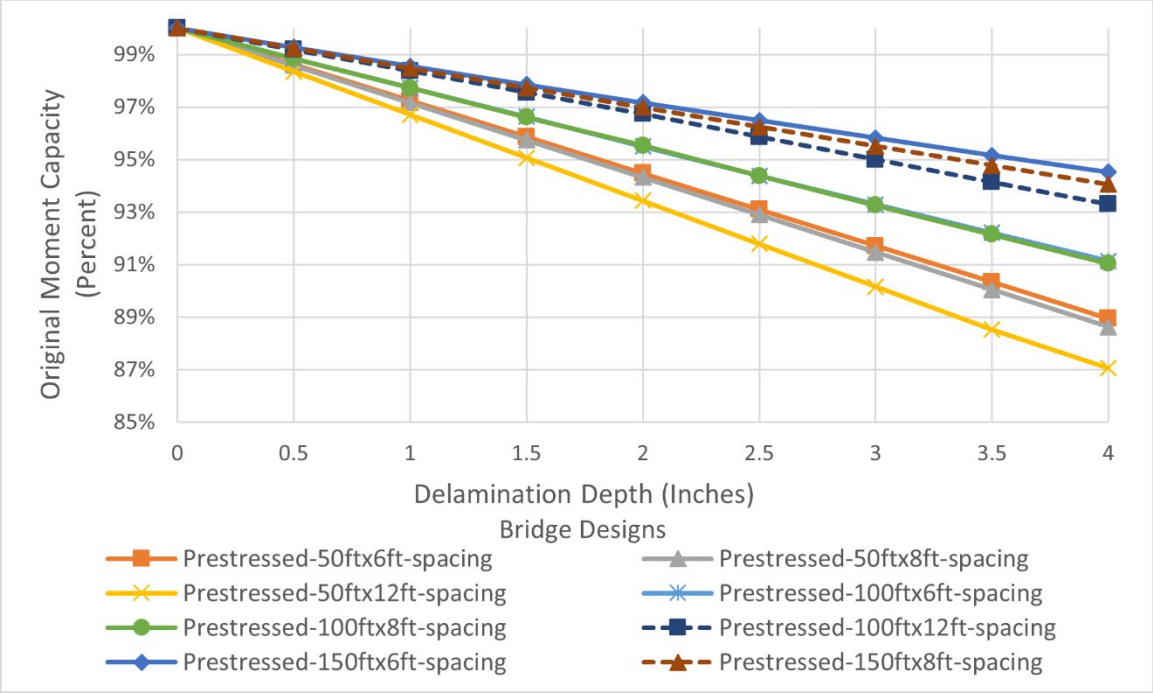

Source: FHWA.
Note: Vertical axis is abbreviated to enable visual discernment of series.

Figure 19. Graph. Effect of delaminations on ultimate moment capacity for prestressed composite sections.

The research team compared the reduction in ultimate moment as determined by the fiber model to the reduction in moment capacity as determined using LRFD equations with reduced deck thickness, as shown in figure 20.

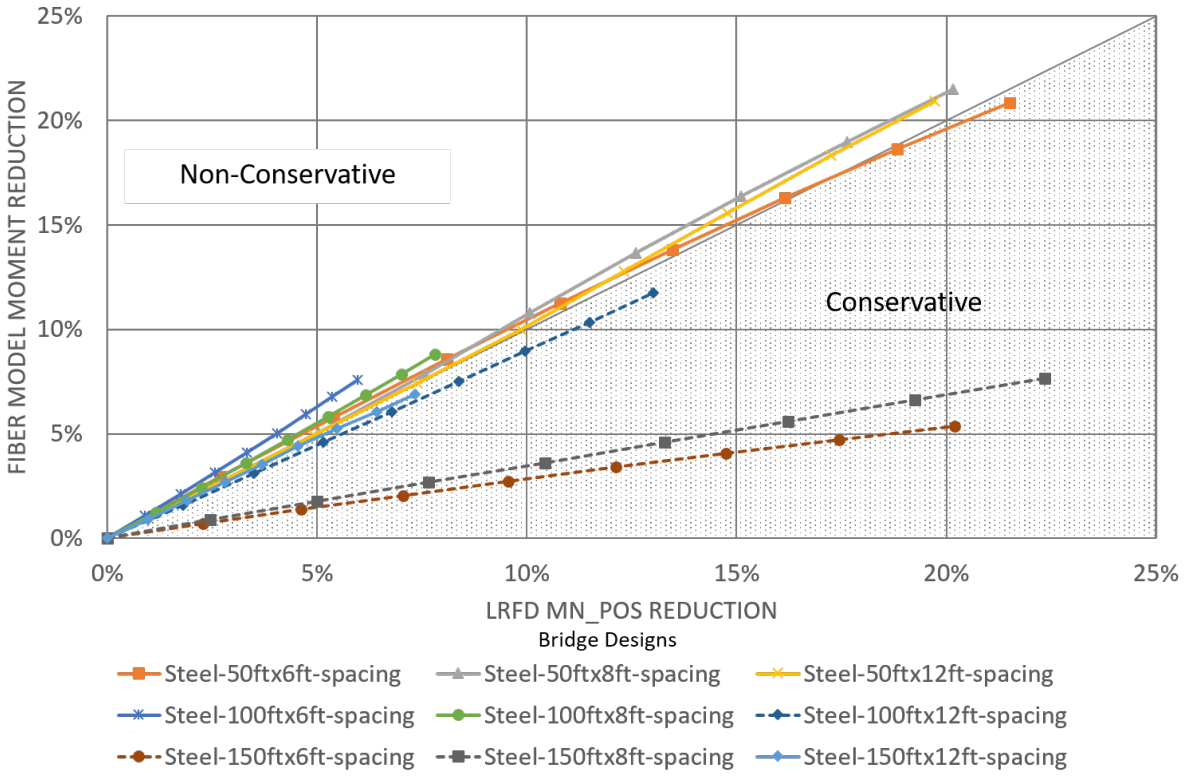

Source: FHWA.

Figure 20. Graph. Comparison of moment reduction due to delaminations according to fiber model and LRFD methods.

From the preceding plot it may be concluded that the existing LRFD capacity equations are sufficient and conservative for estimating the capacity of deteriorated sections by appropriately revising section geometry. The datasets in figure 20 that appear to be outliers (i.e., Steel-150ft×6ft-spacing and Steel-150ft×8ft-spacing) were found to have greater ultimate moment capacity through fiber model analysis than predicted by LRFD calculations. This effect is largely due to the reduction in plastic moment capacity, which is meant to prevent the deck being prematurely crushed, stipulated by LRFD specifications (AASHTO 2017, section 6.10.7.1.2). Additional details for the sensitivity studies can be found in appendix B. Sensitivity studies were also performed to characterize the effect of deterioration and defects on member demands. These studies concluded that deterioration and defects have a minor effect on member demands and that uncertainty in demand models is best reduced by integrating SHM data as described in preceding pages. Additional details regarding these sensitivity studies are in appendix C.

CHAPTER 7. VALIDATION OF INTEGRATION STRATEGIES WITH FIELD-COLLECTED DATA

The research team identified three case structures that had both NDE and SHM data suitable for the integration strategies presented:

- Paint Creek Bridge (NDE Virtual Lab project).
- Haymarket Bridge (Long-Term Bridge Performance [LTBP] Program).
- Bridge Evaluation and Accelerated Structural Testing (The BEAST®) Specimen (Long-Term Infrastructure Performance Program).

The team used various datasets to implement different integration strategies, which are compared in the following sections. Appendix A contains full details of the data integration, structural analysis, and load-rating methods.

CASE STUDY 1: PAINT CREEK BRIDGE

The Paint Creek Bridge (figure 21) in Fayette County, WV, was constructed in 1954. The three-span bridge serves as a key link, connecting numerous mines to the highway system. As such, it sees considerable heavy truck traffic. At the time of testing, the structure was recorded as being structurally deficient and was posted for load, although the posting limits were close to legal limits. The deck exhibited extensive cracking on both the topside and underside. Multiple patch repairs of the deck surface were observed. Many of the bearings were heavily corroded due to failure of the deck joint seals. The West Virginia Department of Transportation commissioned load testing and dynamic testing in 2014. Nondestructive testing was performed in 2016 as part of the FHWA NDE Virtual Laboratory project.

Figure 21. Photo. Paint Creek Bridge (elevation view).

This structure consists of three simply supported spans with five rolled-steel girders, spaced at 8 ft 1 inch on center, and a cast-in-place composite concrete deck. The center span is approximately 52-ft long with two rows of internal diaphragms oriented perpendicularly to the

girders. The two external spans are approximately 20-ft long and have diaphragms at the support locations. The out-to-out width is 35 ft. The southern end of the center span rests on steel rocker bearings, while the northern end rests on pinned bearings. These bearings are supported by reinforced concrete hammerhead piers.

Integration Summary for Case Study 1

The research team recorded midspan displacements and strains during a proof-level load test conducted in 2014. The team used these values for updating FEMs and for computing MBE adjustment factors and experimental DFs. Dynamic modal data (natural frequencies and mode shapes) were also used for model calibration.

The research team computed load ratings using refined analysis, the MBE method, and experimental DFs. Table 6 provides the various demand estimation methods for developing load ratings.

Table 6. Demand model info for rating schema (case study 1).

Method	Demand Model	Integrated Data
Refined Analysis	3D FEM	None (a priori)
Refined Analysis	3D FEM	Displacement
Refined Analysis	3D FEM	Strain
Refined Analysis	3D FEM	Modal
MBE	SLG	Strain
Experimental DF	SLG	Displacement
Experimental DF	SLG	Strain

The research team developed load ratings using refined analysis and updated the 3D FEMs with displacements, strains, and natural frequencies and mode shapes. Deck, barrier, and diaphragm stiffnesses, as well as select boundary conditions, were chosen as the updating parameters. Figure 22 shows the increase in rating (over SLG rating) achieved using the different models.

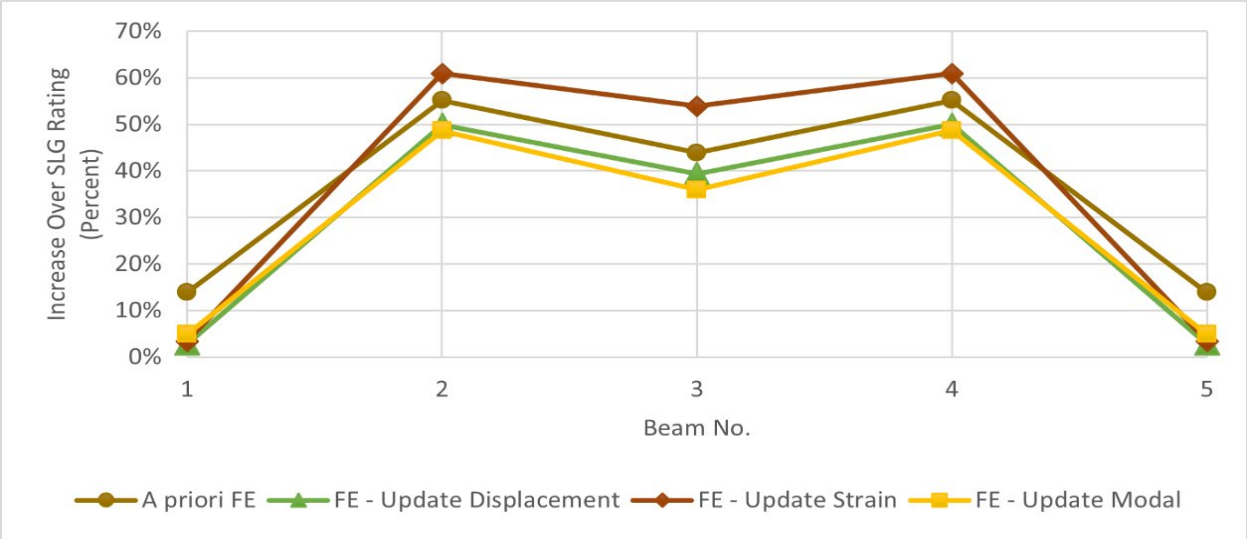

Source: FHWA.

Figure 22. Graph. Strength I load ratings from refined analysis as percentage increase over SLG ratings (case study 1).

The research team also computed ratings using the methods provided by the MBE and experimental DFs. The team implemented the MBE method with the strain readings from the proof-level load. The experimental DFs were computed using displacement and strain data under two loaded trucks. Figure 23 compares the rating factors obtained using the various methods.

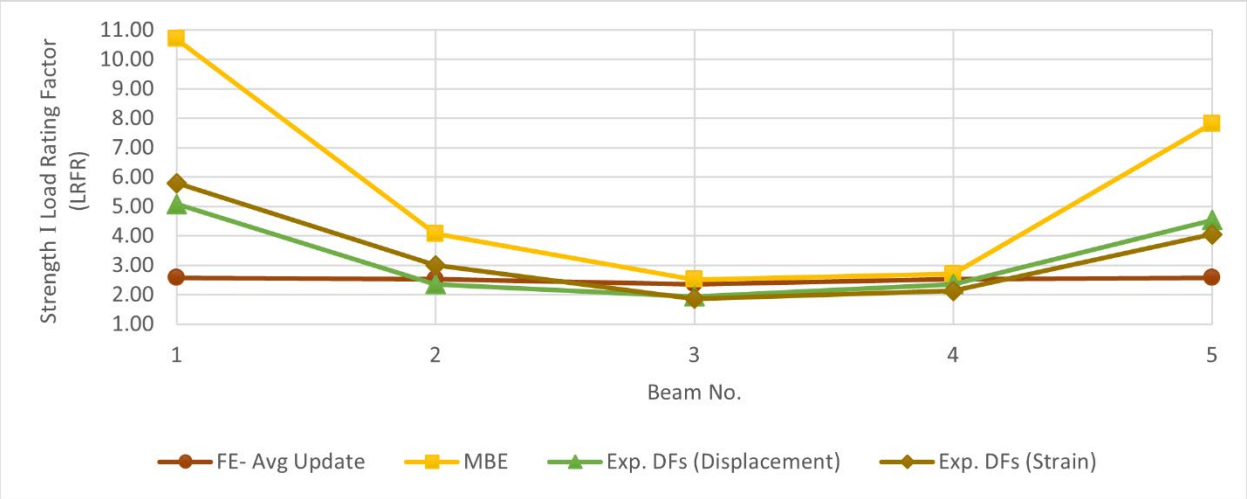

Source: FHWA.
Exp. = experimental.

Figure 23. Graph. Strength I load ratings with data integration (case study 1).

The load ratings were also performed with revised capacities based on the NDE results and a priori capacity. NDE data collection was performed in 2016 using ground-penetrating radar (GPR), impact echo (IE), and ultrasonic surface wave (USW) technologies. The processed IE data provided the most reliable information related to deck thickness and therefore were the only NDE data included in data integration (load rating). Figure 24 depicts the condition map

generated from the IE data. Note that “hot spots” appear near girders 2 and 3, indicating surface delaminations.

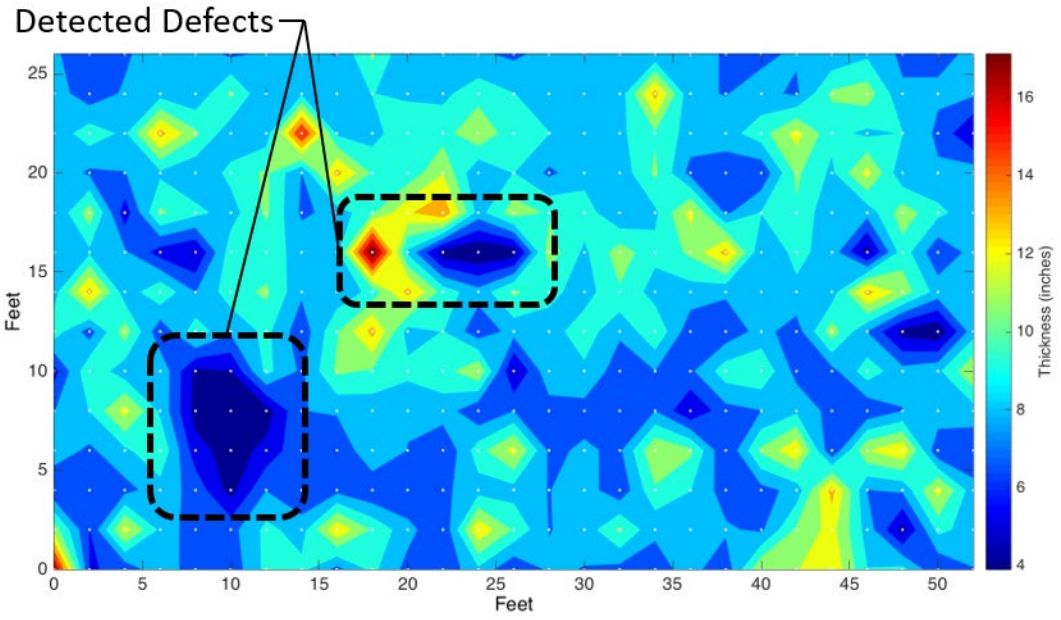

Source: FHWA.

Figure 24. Map. IE condition map (case study 1).

The beam capacities were recomputed with revised deck thickness using standard LRFD equations. The deck thickness over the exterior beams was increased to 8 inches (from the nominal value of 7.5 inches). The deck thickness over beams 3 and 4 was reduced to 6 inches, while that over beam 2 was reduced to 4.5 inches. These changes served to reduce capacity and ratings for interior girders while increasing capacity and ratings for exterior girders (figure 25).

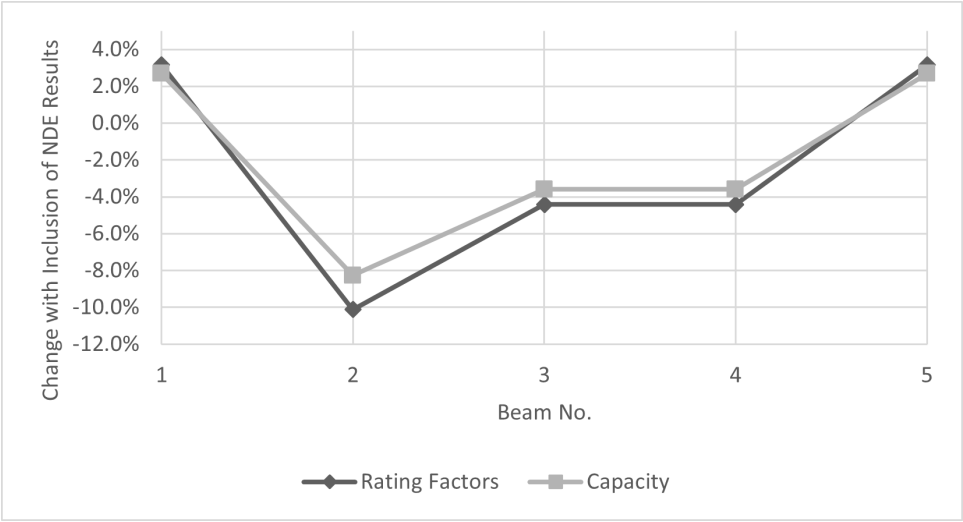

Source: FHWA.

Figure 25. Graph. Effect of NDE data integration on capacity and load ratings (case study 1).

Appendix A contains a more detailed description and demonstration of the integration process.

Summary of Findings from Case Study 1

The following list summarizes the findings from case study 1:

- The model updating schemes had relatively little impact on final load ratings, which may be attributed to the simplicity of the structure—there is relatively little uncertainty in load distribution mechanisms. However, even though updating had little effect on load ratings, the process is still essential as a validation tool.
- Both refined analysis and rating through the use of experimental DFs revealed that this structure is better able to laterally distribute load than predicted by LRFD DFs, resulting in an increase in load-rating factors of approximately 40 percent for interior girders.
- The method provided by the MBE underpredicted force effects, and thus produced nonconservative rating factors for outer girders. The underprediction of force effects can be partially attributed to the sidewalk and barrier stiffness that was active at the time of the load test but was withheld from refined analysis. This effect was also evident in the experimental DFs, but to a lesser extent.
- The integration of NDE results caused a 10-percent reduction in load rating for beam 2, for which the deck thickness had been reduced from 7 to 4.5 inches (−35 percent).

CASE STUDY 2: HAYMARKET BRIDGE

The Haymarket Bridge (figure 26) was constructed in 1979 over I-66 in Virginia. It served as the State's pilot bridge for the LTBP program. Three years of data were collected on this two-span, continuous structure before it was demolished in 2014 as part of a highway widening project.

Figure 26. Photo. Haymarket Bridge viewed from Interstate 66.

Two adjacent structures carried northbound and southbound lanes of U.S. Route 15 over Interstate 66. Each bridge carried two lanes of traffic and a shoulder. The structures had a skew of 17 degrees and consisted of two 137-ft continuous spans with six steel girders of varying depth. The girders were spaced at 7 ft 6 inches on center and braced with steel cross frames. The

superstructures were supported by pinned bearings on concrete piers at the center and rocker bearings at the concrete abutments.

Integration Summary for Case Study 2

A diagnostic load test was performed on this structure in 2009. Strain (bottom flange) and displacement were measured at 40 percent of span length (closer to the abutments) under various loading conditions. Bottom flange strain was also measured over the center support. These values were used for updating FEMs and for computing MBE adjustment factors and experimental DFs.

For this case study, the research team computed load ratings using refined analysis, the MBE method, and experimental DFs. Table 7 provides the various demand estimation methods for load ratings.

Table 7. Demand model info for rating schema (case study 2).

Method	Demand Model	Integrated Data
Refined analysis	3D FEM	None (a priori)
Refined analysis	3D FEM	Displacement
Refined analysis	3D FEM	Strain
MBE	SLG	Strain
Experimental DF	SLG	Displacement
Experimental DF	SLG	Strain

For load ratings by refined analysis, the 3D FEMs were updated with displacements and strains. The stiffness of deck, barrier, diaphragm, and haunch elements were selected as the updating parameters. Load ratings were computed for girders at locations at 40 percent of span length (0.4L) from abutments (commonly considered the controlling location for continuous, two-span structures). Figure 27 shows the increase in rating (over SLG rating) achieved using the different models.

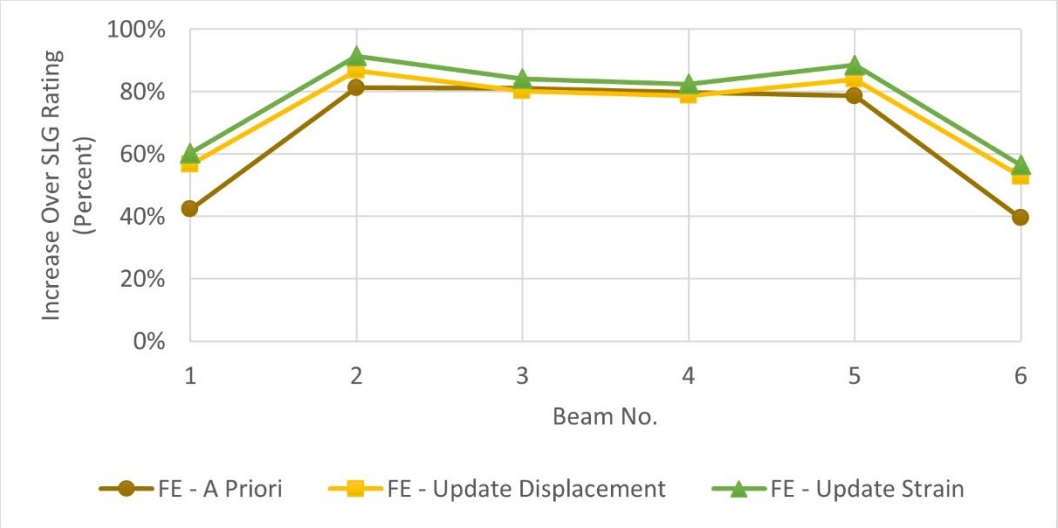

Source: FHWA.

Figure 27. Graph. Load ratings from refined analysis (0.4L) as percentage increase over SLG ratings (case study 2).

The team also computed ratings using the methods provided by the MBE and using experimental DFs. The MBE method was implemented with the strain readings from the proof-level load, and experimental DFs were computed using displacement data under two loaded trucks. Figure 28 compares the rating factors obtained using the various methods.

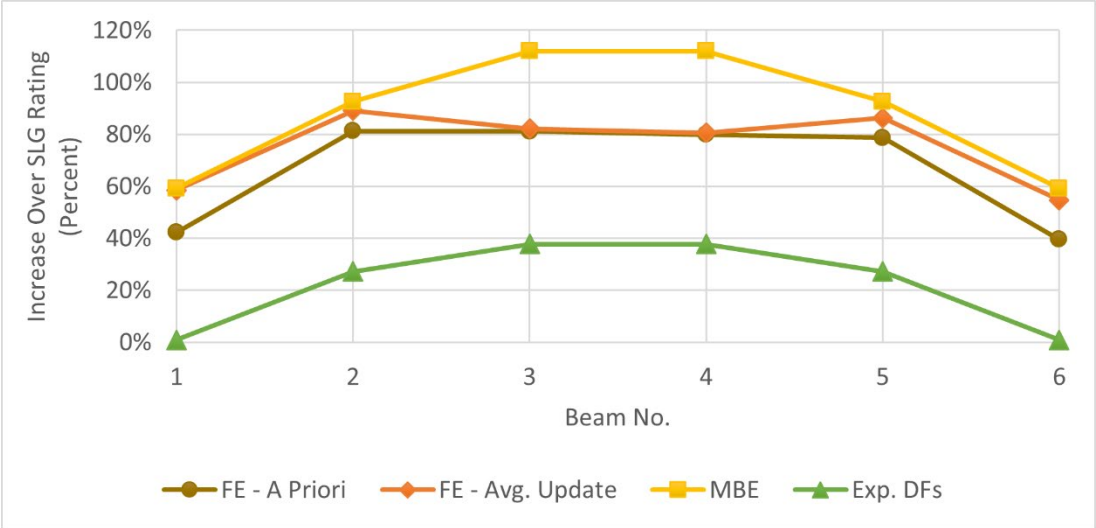

Source: FHWA.
Exp. = experimental.

Figure 28. Graph. Load ratings (0.4L) with data integration as percentage increase over SLG ratings (case study 2).

NDE technologies implemented on this structure included GPR, IE, electrical resistivity (ER), USW, and half-cell potential (HCP). Again, IE provided the best indication of deck thickness and was therefore the only technology whose results were chosen for data integration.

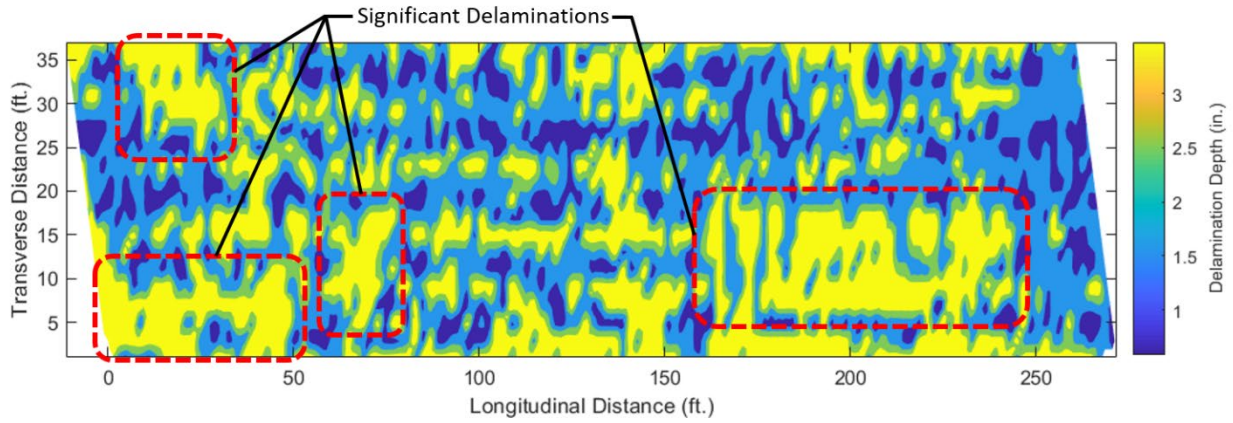

Source: FHWA.

Figure 29. Heat Map. IE condition map (case study 2).

From the condition map generated from IE data (figure 29), one can deduce that the concrete deck is in poor condition with widespread and significant delaminations. Based on these results, it would be prudent to consider the worst-case scenario for load-rating calculations. Therefore, for this demonstration and for computing member capacity, deck thickness was reduced to 5 inches. This reduction in thickness served to reduce capacity and ratings, as depicted in figure 30.

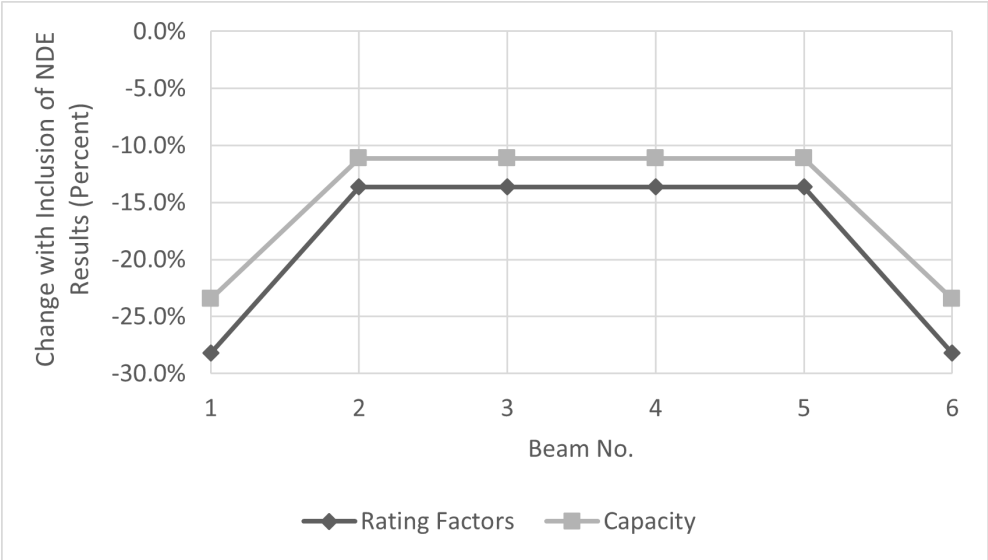

Source: FHWA.

Figure 30. Graph. Effect of NDE data integration on capacity and load ratings (case study 2).

Appendix B contains a detailed description and demonstration of the integration process.

Summary of Findings from Case Study 2

The following list summarizes the findings from case study 2:

- The refined analysis with a priori and updated FEMs yielded similar load ratings, resulting in a load-rating increase of approximately 50 percent for exterior girders and approximately 80 percent for interior girders.
- The use of experimental DFs resulted in lower ratings than the refined analysis produced; however, this method still resulted in a 20−40 percent increase in load ratings for interior girders compared to standard SLG analysis while remaining conservative.
- The method provided by the MBE for incorporating experimental data again produced nonconservative rating factors compared to refined analysis.
- The integration of NDE results caused a load-rating reduction of more than 25 percent for exterior beams and more than 10 percent for interior beams. These reductions can be attributed to a similar decrease in capacity due to a reduction in deck thickness to 5 inches.

CASE STUDY 3: THE BEAST

The BEAST is an accelerated testing laboratory that was constructed in 2015 at the Rutgers University Center for Advanced Infrastructure and Transportation. The laboratory can accommodate a 50-ft long bridge and provide loading of up to 60,000 lb traveling at up to 20 mph. The specimen is contained in an environmental chamber that can cycle temperatures from 0 to 100°F. Construction of the first bridge specimen (figure 31) was completed in 2019. Material samples were taken during construction for testing, and NDE and SHM data collection is ongoing.

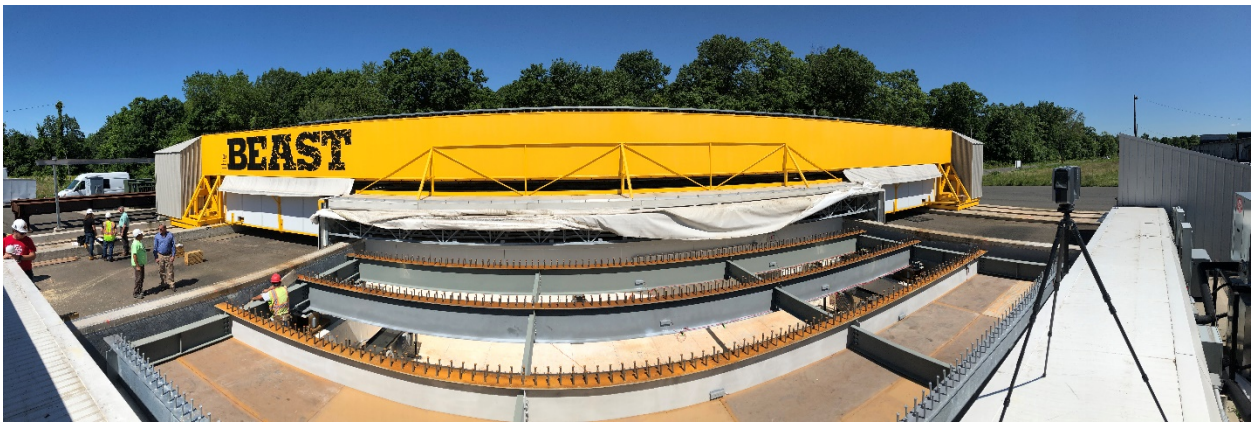

Source: FHWA.

Figure 31. Photo. The BEAST bridge specimen during construction.

The specimen consists of a single, 50-ft, simply supported span. It is composed of four rolled-steel girders and a cast-in-place concrete deck. Bracing is provided between the girders with channel sections.

Integration Summary for Case Study 3

Continuous loading of the specimen is already in progress. Slow-speed passes of the loading carriage occur periodically and provide quasi-static load-response conditions. The midspan strains for four different load-path locations (lateral position) were compiled for use in this case study.

The research team developed load ratings using several different demand estimation methods, as summarized in table 8. The 3D FEMs were updated with strain, with the chosen parameters being deck stiffness, curb thickness, and diaphragm stiffness. The first two updates (using deck stiffness, curb thickness, and diaphragm stiffness) adjusted the parameters globally, while the third update adjusted the thickness of different regions of the deck independently. Figure 32 shows the increase in rating (over SLG rating) achieved using the different models.

Table 8. Demand model info for rating schema (case study 3).

Method	Demand Model	Integration Data
Refined analysis	3D FEM	None (a priori)
Refined analysis	3D FEM	Strain (global)
Refined analysis	3D FEM	Strain (global)
Refined analysis	3D FEM	Strain (local)
MBE	SLG	Strain
Experimental DF	SLG	Strain

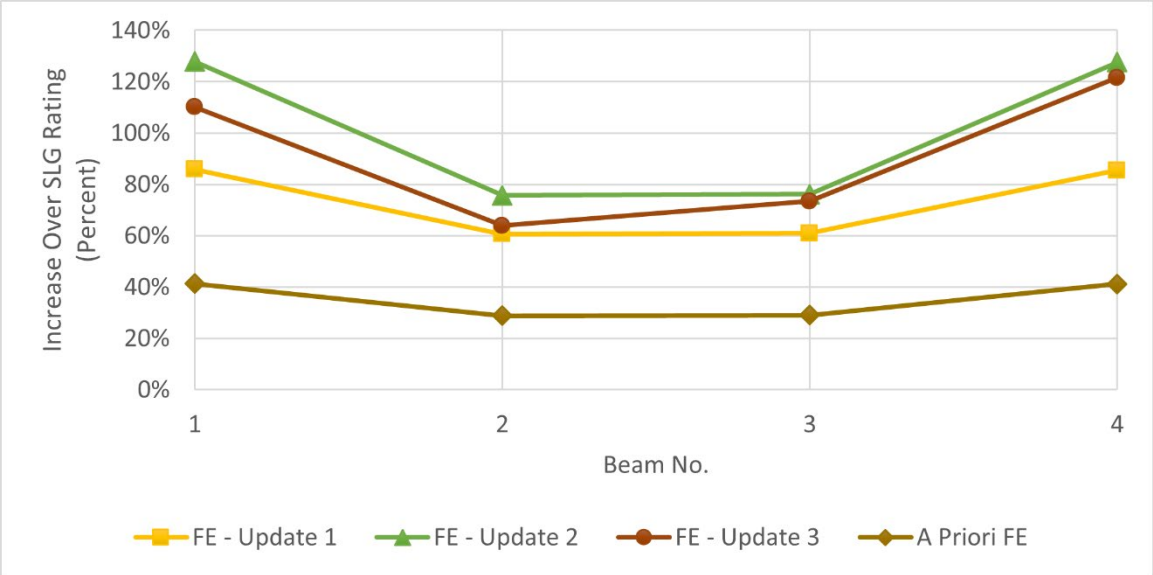

Source: FHWA.

Figure 32. Graph. Strength I load ratings from refined analysis as percentage increase over SLG ratings (case study 3).

The team also computed ratings using the methods provided by the MBE and experimental DFs. The experimental data were not well suited to experimental DFs as the loading paths were partially overlapping. Therefore, in this case, the experimental DFs will overestimate the portion

of load an individual girder is expected to experience. The rating results are still included in figure 33, even though this is not an ideal use case.

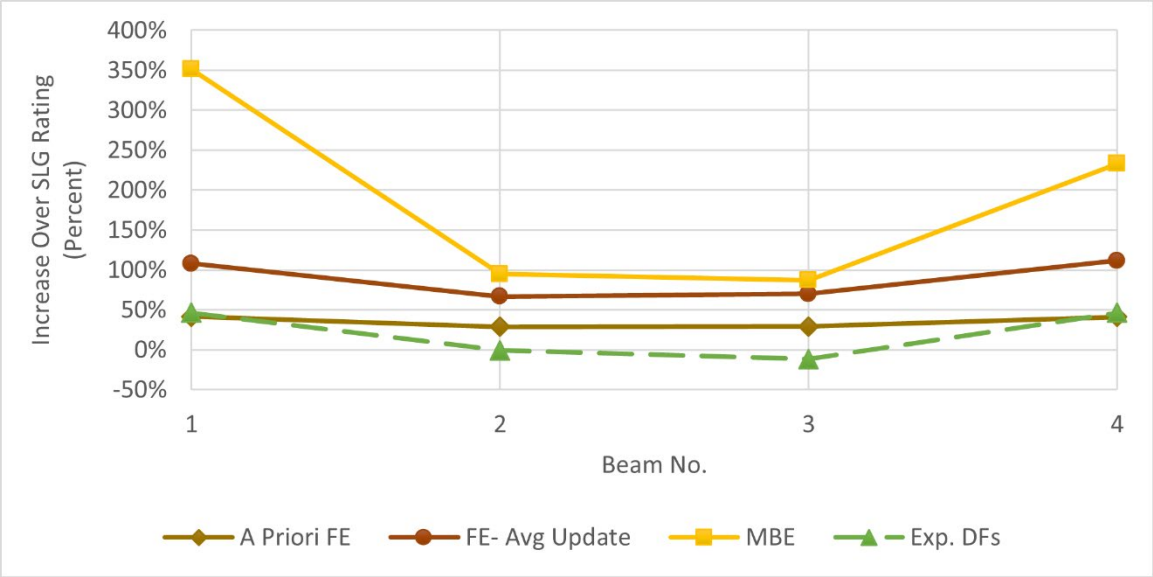

Source: FHWA.

Figure 33. Graph. Strength 1 load ratings with data integration as percentage increase over SLG ratings (case study 3).

For the load ratings presented in the previous plots, the research team revised capacities based on NDE results. GPR scans of the deck revealed that the concrete cover over rebar was only 1.25 inches in the center portion of the deck rather than the specified 2-inch cover, as seen in the condition map shown in figure 34. This construction error was confirmed by a LiDAR scan of the top and bottom surfaces of the structure. The data were processed to produce a point-cloud representation of the in situ geometry of the structure. Deck thickness measurements were made by simply computing the distance between points at the top and bottom surface of the deck.

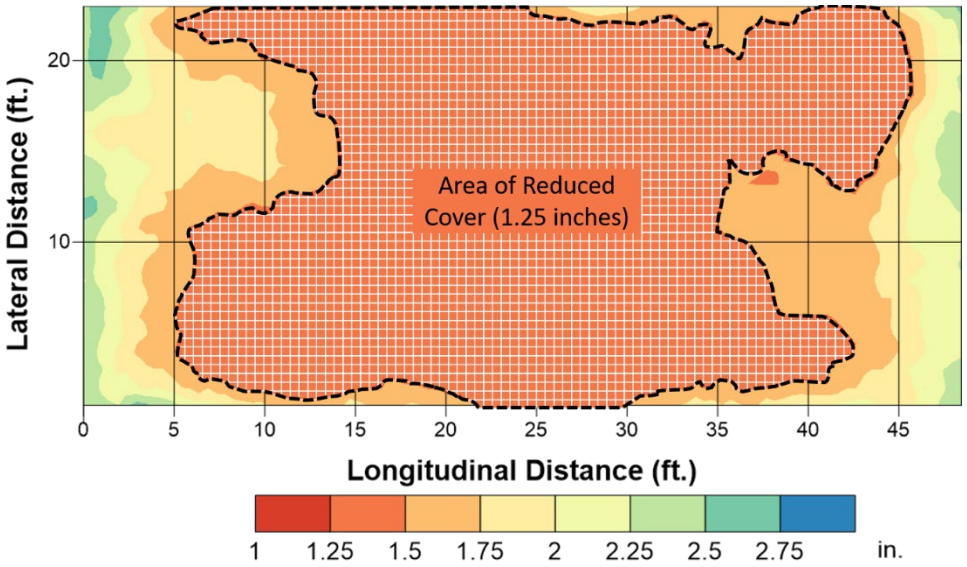

Source: FHWA.

Figure 34. Heat Map. Depth of concrete cover as determined by GPR scanning.

Furthermore, the team performed extensive material testing to determine the mechanical properties of the deck concrete, including compressive strength, modulus of elasticity, modulus of rupture, and splitting tensile strength. The compressive strength data was selected as most suitable for data integration. The team recomputed capacity estimates using a deck thickness of 7.25 inches (compared to specified 8-inch-thick deck) and a compressive strength of 4,936 psi. The NDE data integration resulted in a 2- to 3-percent decrease in capacity estimates, which resulted in similar reductions in load ratings, as shown in figure 35.

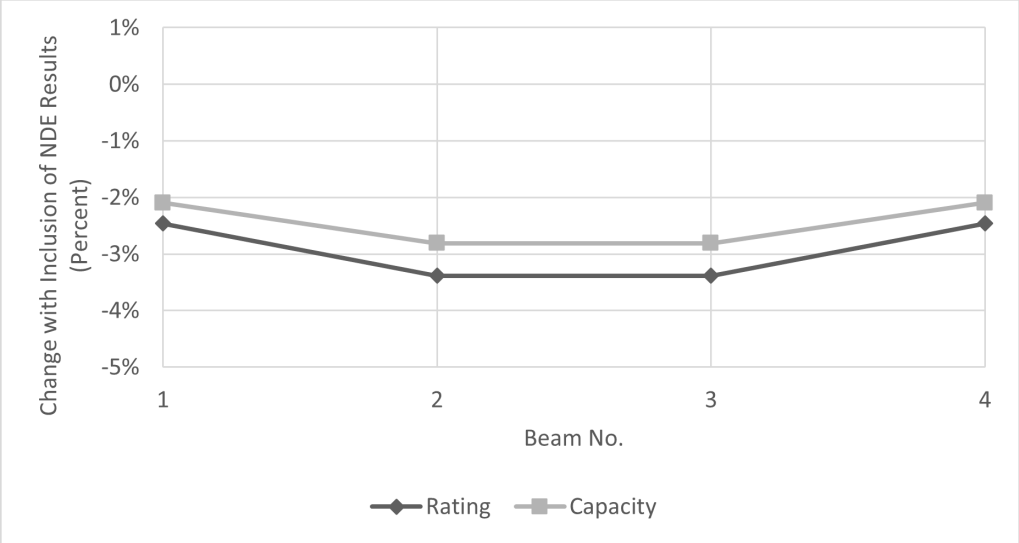

Source: FHWA.

Figure 35. Graph. Effect of NDE data integration on capacity and load ratings.

Further description and demonstration of the integration process can be found in appendix A.

Summary of Findings for Case Study 3

The following list summarizes the findings from case study 3:

- The refined analysis with updated FEMs resulted in a load-rating increase of approximately 75 percent for interior girders and approximately 100 percent for exterior girders. This change in rating can be attributed to an increase in lateral load distribution compared to that assumed by SLG methods.
- Model calibration had a significant effect on demand estimation and load ratings. Refined analysis with the updated FEMs yielded higher load ratings than those performed with the a priori model. This result is because the stiffness of lateral-load-transfer mechanisms in the updated models was increased to match the load distribution reflected in the experimental results.
- The method provided by the MBE for incorporating experimental data again produced nonconservative rating factors compared to refined analysis, especially for exterior girders. This can be attributed to the additional stiffness contributed by the concrete curb and the bias of loading toward the middle (centerline) of the bridge. The experimental loads were positioned along or near the longitudinal centerline of the bridge, and thus relatively little load was distributed to the exterior girders compared to what would likely occur under rating-load configurations.
- The use of experimental DFs resulted in lower ratings than the refined analysis produced; however, the experimental data (i.e., overlapping loading paths) were ill-suited to this method and would not be recommended. When performing load testing for the purposes of load rating with experimental DFs, loads should be positioned as specified by applicable load-rating standards.
- The integration of NDE results caused a load-rating reduction of less than 4 percent. This reduction can be attributed to a similar decrease in capacity due to the reduction of deck thickness to 7.25 inches.

CHAPTER 8. RECOMMENDATIONS FOR INTEGRATING NDE AND SHM DATA IN LOAD RATINGS

Based on the results of the research presented herein, the research team developed a series of recommendations for including both sensor data and NDE data within the load-rating process. These recommendations are organized into those related to data collection and those related to integration approaches, as detailed in the following two sections.

DATA COLLECTION

To ensure the appropriate integration of experimental data within the load-rating process, it is first necessary to begin with complete and reliable experimental data. It is important to recognize that if a flawed experimental program (either due to poor quality or incompleteness) is used to acquire data, it is not possible to make up for these flaws within the integration process. As a result, it is imperative that an experimental design be carried out to ensure the objectives of the effort can be met with the type, density, quality, and other characteristics of the data to be gathered. Many others have developed rigorous recommendations for data collection efforts, and the goal of this discussion is not to repeat their suggestions (Çatbaş, Kijewski-Correa, and Aktan 2013; Alampalli 2019). Rather, the items in the following lists are meant to supplement those other recommendations and highlight the importance of various factors that, based on the research team's experience, are important for obtaining useful data and are commonly overlooked.

When performing static-load testing for the purpose of computing load ratings, the following is recommended:

- The load level (magnitude) should be as close to the rating-load level as practical.
- The lanes should be loaded in the same manner as is assumed for load rating (i.e., the "design lanes" should be loaded if possible, not the travel lanes).
- When only a single loading vehicle is available, the vehicle should be placed in each rating lane and positioned to produce maximum response in controlling members.
- All primary load-carrying members should be instrumented at controlling locations (i.e., locations expected to exhibit maximum response or have the least reserve capacity).
- All primary members should be instrumented to provide insight into the way the element is carrying load (e.g., strain profile, composite action).

When performing dynamic testing for the purposes of identifying modal parameters and calibrating the model for refined analysis and load rating, keep in mind the following:

- Care should be taken to ensure that the longitudinal and transverse stiffness of the structure are properly captured. At a minimum, this means that the first bending, first torsion, and first butterfly mode shapes should be captured.
- Sensors should be spatially distributed to sufficiently characterize the shape of all modes of interest. In general, this should be done by deploying a minimum of 9 accelerometers per span.

When conducting NDE of a structure for the purpose of revising capacity for load ratings, consider the following:

- Technologies that provide information of element (i.e., girder, deck) geometry, degradation, and material strength should be chosen.
- For concrete decks, NDE should aim to capture deck thickness (i.e., presence of delaminations) and the compressive strength of the concrete.

DATA INTEGRATION

Once data of sufficient completeness and quality have been obtained, the integration approaches for including these data within the load process can be implemented. In general, this involves reducing uncertainties within both demand and capacity estimates. Although in most cases this process lowers demand estimates, thus increasing rating factors, this is not always true, and one should recognize that there is a potential for demand estimates to remain unchanged or even increase. In the case of capacity estimates, the use of NDE data will generally reduce capacity estimates compared with the use of nominal dimensions and material properties, but may increase capacity estimates when material strength is shown to be higher than initially assumed or when components are found to be larger than specified in construction documents. The following recommendations are offered to guide these efforts:

- Live-load demands for in situ bridges should be estimated using calibrated refined-analysis models whenever feasible, as they are most capable of representing the numerous mechanisms present on real structures and are the only analysis tools that allow for consideration and removal of the effects of unreliable mechanisms.
- When experimental data are available but FEM is impractical, data may be incorporated into SLG analysis methods by using experimental DFs. This approach is applicable to relatively simple structures for which SLG methods are valid.
- Incorporation of experimental data using the methods provided by the MBE is not recommended until the MBE approach provides some means of quantifying and discounting the effect of unreliable mechanisms, especially when the behavior of the structure is complex or poorly understood.
- NDE data may be incorporated into the load-rating process when the data provide information about the component geometry (e.g., deck thickness) or material properties (e.g., compressive strength). The NDE results may be directly incorporated into the LRFD capacity equation by substitution. This method provides a more quantitative measure of remaining capacity and a better reduction in the associated uncertainty than condition factors alone.

APPENDIX A. DEMONSTRATIONS IN INTEGRATION

CASE STUDY 1: PAINT CREEK BRIDGE

Experimental Data

A proof-level load test was performed on this bridge in 2014. The test trucks were filled to varying levels to provide a variety of load levels. A total of eight load stages were performed, ranging from a single empty truck to four fully loaded trucks totaling 299 kilopounds (kips). This progressive loading ensures that the structure can be safely monitored for any unexpected behavior or nonlinear deformation.

Figure 36 and figure 37 depict the two fully loaded trucks positioned at midspan, and figure 38 shows the midspan strains (on girder bottom flanges) and displacements. This dataset will be used for the demonstration of all integration methods.

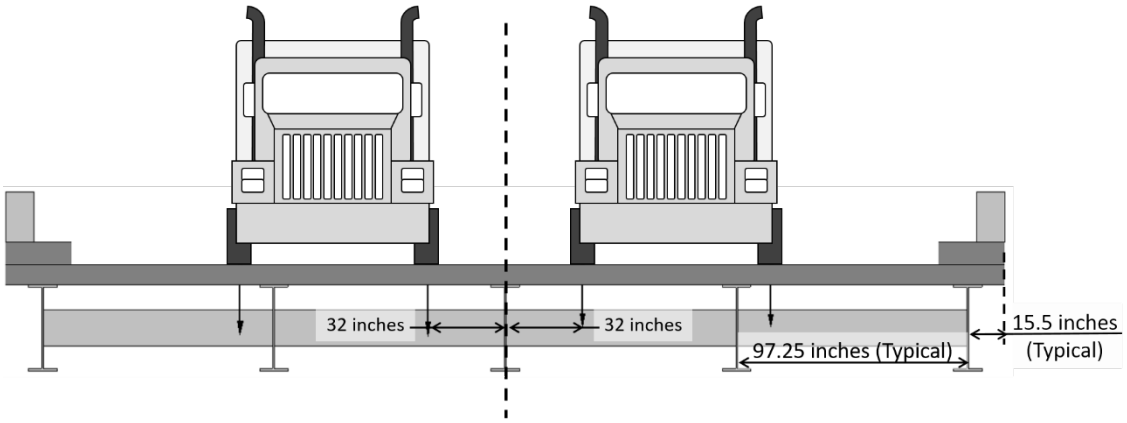

Source: FHWA.

Figure 36. Illustration. Section view of bridge with lateral load position (case study 1).

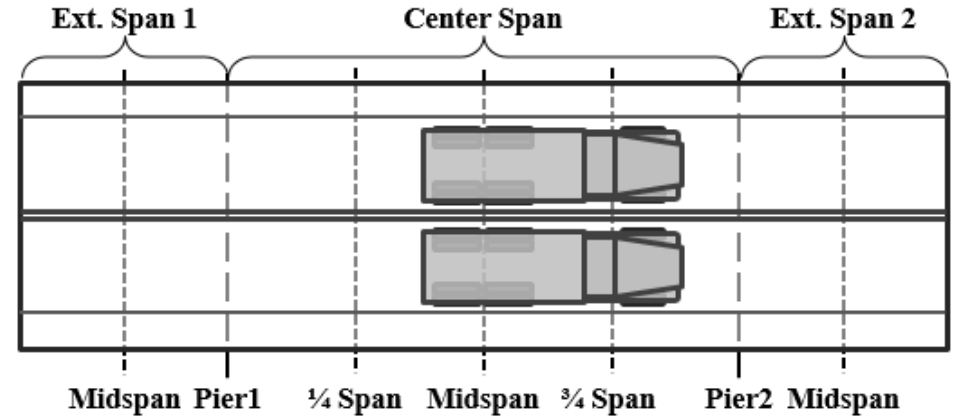

Source: FHWA.

Figure 37. Illustration. Load configuration for presented dataset (case study 1).

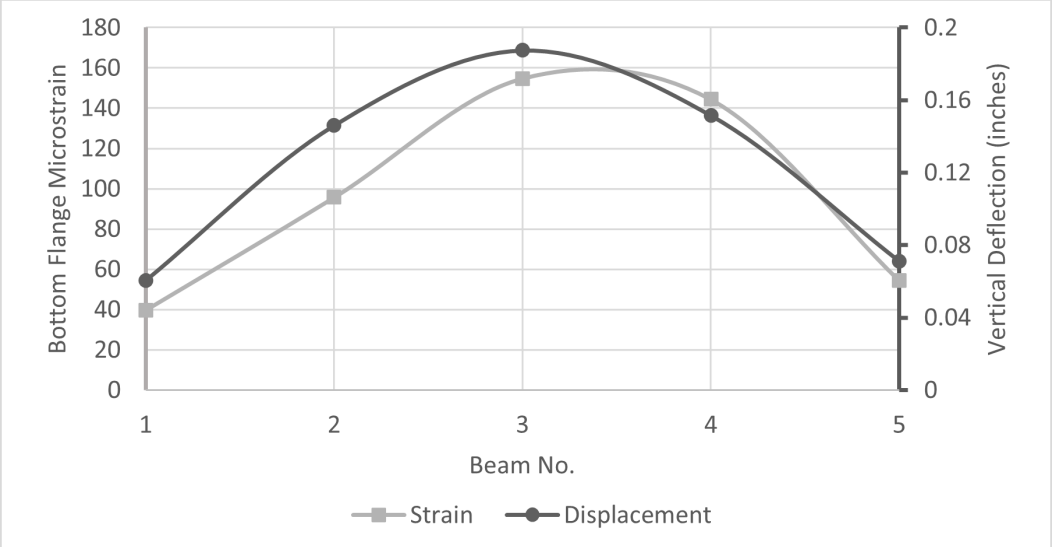

Source: FHWA.

Figure 38. Graph. Integration dataset: midspan strain and displacement (case study 1).

Impact (forced vibration) testing was also performed at the time of the load test. Acceleration was recorded by distributed sensors while impacts were performed at multiple locations. The data were processed to obtain the following natural frequencies and mode shapes, as shown in figure 39 through figure 44.

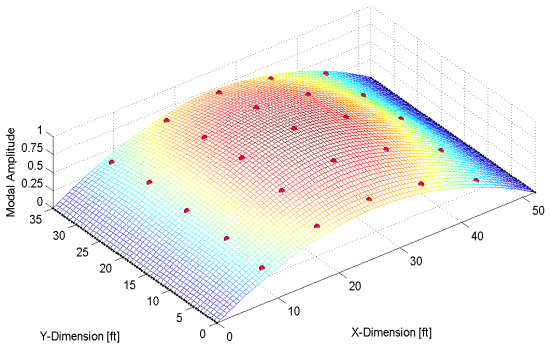

Source: FHWA.

Figure 39. Surface Plot. Experimental mode 1: 8.75 Hz (case study 1)

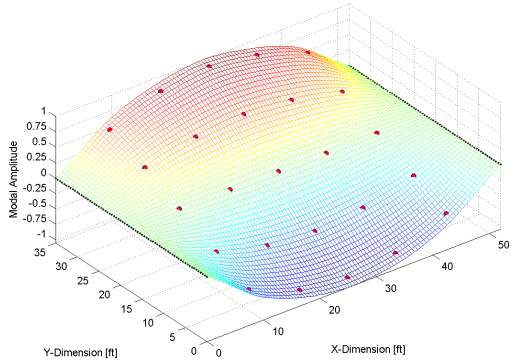

Source: FHWA.

Figure 40. Surface Plot. Experimental mode 2: 9.4 Hz (case study 1)

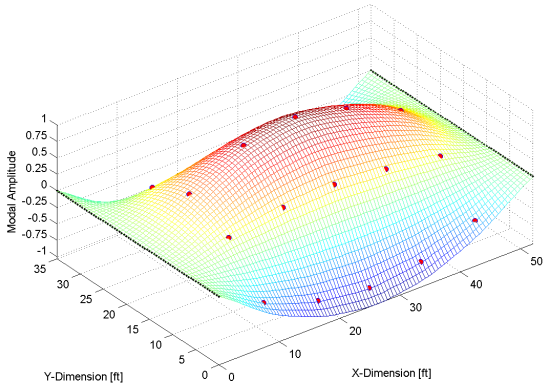

Source: FHWA.

Figure 41. Surface Plot. Experimental mode 3: 13.5 Hz (case study 1).

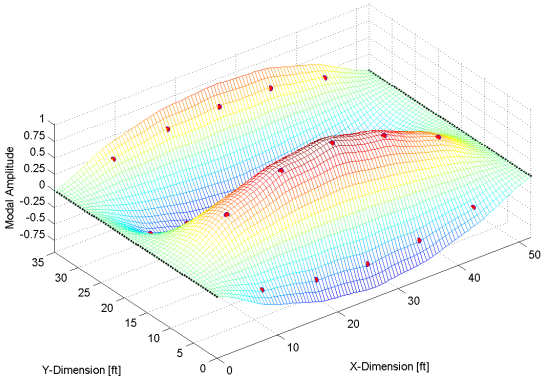

Source: FHWA.

Figure 42. Surface Plot. Experimental mode 4: 21.6 Hz (case study 1).

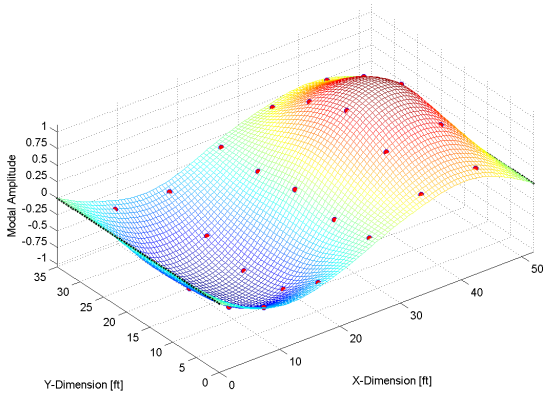

Source: FHWA.

Figure 43. Surface Plot. Experimental mode 5: 27.7 Hz (case study 1).

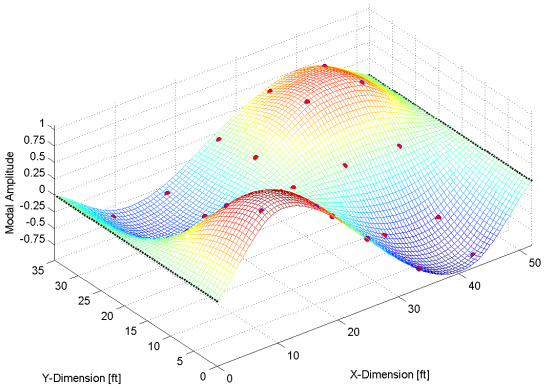

Source: FHWA.

Figure 44. Surface Plot. Experimental mode 6: 29.8 Hz (case study 1).

NDE data collection was performed in 2016 using GPR, IE, and USW. The processed IE data provided the most reliable information related to deck thickness and therefore were the only NDE data included in the data integration (load rating). Figure 24 depicts the condition map generated from the IE data.

From this IE data, the research team determined the deck thickness over the exterior beams was 8 inches, while the deck thickness over beams 3 and 4 was only 6 inches, and that over beam 2 was only 4.5 inches.

Integration Process

SLG Analysis

The research team first computed demands based on SLG analysis. They used these values for comparison, for the MBE method, and for use in conjunction with experimental DFs.

The team applied dead load and superimposed dead load as distributed loads to compute the moment at midspan. They then applied LRFD HL-93 design loading (single lane with a dynamic load allowance and lane load of 33 percent) to produce member actions under live-load conditions (AASHTO 2017, section Cl 3.6.1.2).

Table 9 summarizes the SLG demands.

Table 9. SLG demands (moment: lb-inches) (case study 1).

Girder Location	Dead Load	Superimposed Dead Load	Wearing Surface	Live Load
Interior Girder	4.26E+06	7.15E+05	0	1.31E+07
Exterior Girder	3.07E+06	7.15E+05	0	1.31E+07

The live-load demands were apportioned to individual girders according to the LRFD DFs (table 10).

Table 10. LRFD moment DFs (case study 1).

Girder Location	Single Lane	Multiple Lanes
Interior Girder	0.54	0.73
Exterior Girder	0.36	0.47

FE Analysis

Using the commercial software Strand7, the research team constructed an element-level FEM (figure 45) based on bridge geometry and assumed material properties provided in construction documents (Strand7 2013). This model employed one-dimensional, two-node beam elements for girders, diaphragms, and barriers. Each node had six degrees of freedom (DOF) to permit all translations and rotations. This type of element can account for axial, bending, torsional, and shear deformations. The team used two-dimensional (2D), four-node shell elements to model the deck and sidewalk and rigid links to enforce compatibility between girder and deck elements (thereby enforcing composite action).

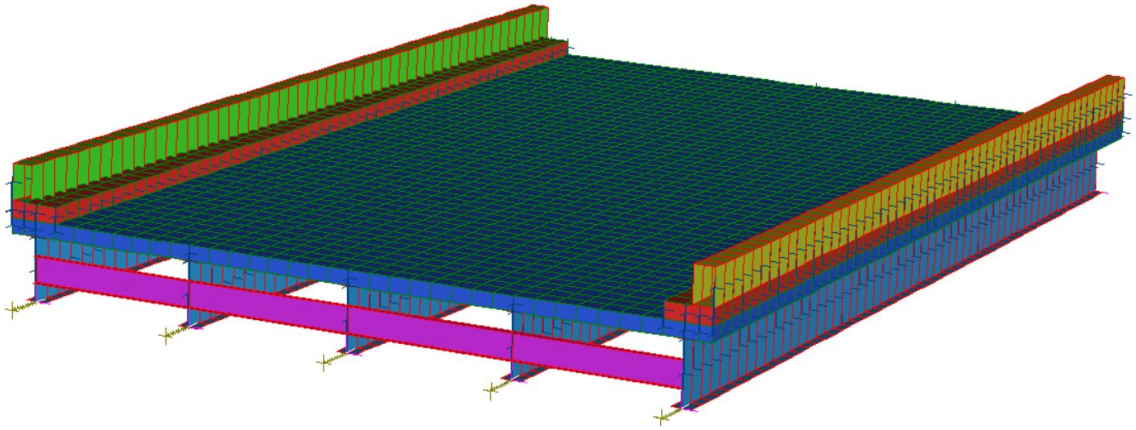

Source: FHWA.

Figure 45. Illustration. 3D FEM of bridge (case study 1).

The team updated and calibrated the model with strain data, displacement data, and modal data (frequencies and mode shapes). They then matched experimental data points with model responses for comparison and evaluation of model fit. Simulated responses to load-test configurations were obtained by positioning loads in the model to match the locations depicted in figure 37. The team chose parameters that were uncertain (e.g., concrete stiffness) or influential to the responses being monitored. They manipulated the model with an application program interface that allowed communication between MATLAB and the FE software (Strand7). Calibration was completed with the aid of a nonlinear optimization algorithm (MATLAB function: lsqnonlin), which sought to minimize the difference between model responses and experimental data by adjusting parameter values in the model.

Table 11 contains the final parameter values resulting from the model calibration process.

Table 11. Updated model parameter values (case study 1).

Parameter	Original Value	Update 1: Modal	Update 2: Displacement	Update 3: Strain
Deck E (psi)	3.60E+06	3.40E+06	3.05E+06	8.19E+06
Diaphragm E (psi)	2.90E+07	7.42E+06	2.27E+07	—
Right barrier E (psi)	3.60E+06	2.96E+06	—	1.33E+07
Left barrier E (psi)	3.60E+06	2.96E+06	—	3.60E+07
BC spring stiffness (lb/inch)	1.00E+05	2.23E+03	—	—

—Parameter not altered during updating run.

The team used a priori and updated models to perform refined analyses to obtain load ratings. They removed the stiffness of barrier and sidewalk elements before solving for live-load demands. The model was rated with HL-93 loading positioned to create maximum force effect at midspan of the girders (AASHTO 2017, section Cl 3.6.1.2). The team calculated composite moment under live-load conditions according equation 7:

$$M_C = M_1 + F_A * \frac{D+t_D}{2} \quad (7)$$

Where:

M_C = composite moment.
M_1 = principle bending moment.
F_A = axial force.
D = girder depth.
t_D = deck thickness.

Table 12 summarizes the demands as determined from refined (i.e., FE) analysis.

Table 12. FE analysis demands (moment: lb-inches) (case study 1).

Beam No.	Dead Load	Superimposed Dead Load	*LL*: A Priori	*LL*: Update 1	*LL*: Update 2	*LL*: Update 3
Beam 1	2.84E+06	1.25E+06	4.00E+06	5.74E+06	5.86E+06	5.82E+06
Beam 2	4.38E+06	6.45E+05	5.17E+06	6428879	6.37E+06	5.94E+06
Beam 3	4.04E+06	4.58E+05	6.16E+06	7.20E+06	7.02E+06	6.36E+06
Beam 4	4.38E+06	6.45E+05	5.17E+06	6.43E+06	6.37E+06	5.94E+06
Beam 5	2.84E+06	1.25E+06	4.00E+06	5739542	5.86E+06	5.82E+06

MBE Method

The MBE allows for experimental data to be considered in the load-rating process by applying an adjustment factor (K) to the theoretical (SLG) rating, as described by equation 2 (AASHTO 2018, section 8.8.2.3).

The magnitude of the rating load for this bridge is 144 kips. The load test applied over 147 kips; therefore, the ratio of test load to rating load is greater than 1, and K_b is equal to 1.0. Table 13 provides the recorded midspan strain, the corresponding theoretical strain as determined by SLG methods (SLG *LL* moment divided by the short-term composite-section modulus), and the resulting MBE adjustment factors.

Table 13. MBE adjustment factors (case study 1).

Beam No.	Experimental Strain	Theoretical Strain	K_a	K
Beam 1	39.699	1.73E+02	3.35	4.35
Beam 2	95.695	2.62E+02	1.73	2.73
Beam 3	154.76	2.62E+02	0.690	1.69
Beam 4	144.36	2.62E+02	0.812	1.81
Beam 5	54.3345	1.73E+02	2.18	3.18

Experimental DFs

Using equation 5, the team computed experimental DFs for a load case in which two fully loaded trucks were positioned at midspan. This bridge had two rating lanes, and the corresponding multiple presence factor is 1.0. Table 14 provides the DFs computed from both strain and displacement responses.

Table 14. Experimental DFs (case study 1).

Beam No.	Experimental DF: Strain	Experimental DF: Displacement	LRFD DF
Beam 1	0.20	0.23	0.47
Beam 2	0.40	0.51	0.73
Beam 3	0.65	0.62	0.73
Beam 4	0.57	0.51	0.73
Beam 5	0.29	0.26	0.47

Capacity

The research team calculated member capacities according to appropriate LRFD equations. For the Strength I limit state, capacity is defined as the plastic moment capacity of the composite section, which is computed as the sum of section plastic forces. The girder stress limit for the Service II limit state is defined as 95 percent of the yield strength.

The team integrated NDE results into the capacity calculations by revising the deck thickness to that determined through IE testing. Table 15 and table 16 summarize the composite member capacities. All values were determined using appropriate LRFD equations.

Table 15. A priori member capacities (case study 1).

Beam No.	Deck Thickness (Inches)	SB_{st} (Inches^3)	M_n (lb-Inches)	F_y (psi)
Beam 1	7	781.2	3.12E+07	33,000
Beam 2	7	809.6	3.39E+07	33,000
Beam 3	7	809.6	3.39E+07	33,000
Beam 4	7	809.6	3.39E+07	33,000
Beam 5	7	781.2	3.12E+07	33,000

F_y = flange yield strength; M_n = nominal moment capacity (positive bending); SB_{st} = short-term composite-section modulus for the bottom fiber.

Table 16. Revised member capacities (case study 1).

Beam No.	Deck Thickness (Inches)	SB_{st} (Inches^3)	M_n (lb-Inches)	F_y (psi)
Beam 1	8.0	805.3	3.21E+07	33,000
Beam 2	4.5	746.7	3.11E+07	33,000
Beam 3	6.0	784.8	3.27E+07	33,000
Beam 4	6.0	784.8	3.27E+07	33,000
Beam 5	8.0	805.3	3.21E+07	33,000

F_y = flange yield strength; M_n = nominal moment capacity (positive bending); SB_{st} = short-term composite-section modulus for the bottom fiber.

Load Ratings

The research team computed load ratings according to MBE equation 6A.4.2.1-1. Table 17 summarizes the various load and resistance factors used.

Table 17. Load and resistance factors for inventory load ratings (case study 1).

Limit State	System Factor	Condition Factor	Resistance Factor	*DC*	*DW*	*LL* + *IM*
Strength I	1	1	1	1.25	1.5	1.75
Service II	1	1	1	1.00	1.0	1.30

Table 18 summarizes the load rating factors computed using SLG analysis without any adjustment factors applied. Table 19 provides the SLG rating factors for which capacity estimates were revised based on NDE data using the recommendations provided in section 5.

Table 18. A priori SLG rating factors (case study 1).

Beam No.	Strength I	Service II
Beam 1	2.48	2.46
Beam 2	1.65	1.49
Beam 3	1.65	1.49
Beam 4	1.65	1.49
Beam 5	2.48	2.46

Table 19. SLG rating factors using revised capacity.

Beam No.	Strength I	Service II
Beam 1	2.56	2.53
Beam 2	1.48	1.37
Beam 3	1.58	1.45
Beam 4	1.58	1.45
Beam 5	2.56	2.53

Table 20 summarizes the load-rating factors when adjusted using the factors provided in the MBE (AASHTO 2018).

Table 20. MBE rating factors (case study 1).

Beam No.	Strength I	Service II
Beam 1	10.79	10.69
Beam 2	4.51	4.07
Beam 3	2.79	2.52
Beam 4	2.99	2.70
Beam 5	7.88	7.81

Table 21 through table 24 summarize the load-rating factors when experimental DFs are used.

Table 21. Rating factors using experimental DFs from strain data and a priori capacity (case study 1).

Beam No.	Strength I	Service II
Beam 1	5.79	5.75
Beam 2	3.00	2.71
Beam 3	1.86	1.68
Beam 4	2.13	1.93
Beam 5	4.05	4.02

Table 22. Rating factors using experimental DFs from strain data and revised capacity (case study 1).

Beam No.	Strength I	Service II
Beam 1	5.97	5.93
Beam 2	2.70	2.50
Beam 3	1.78	1.63
Beam 4	2.04	1.87
Beam 5	4.18	4.15

Table 23. Rating factors using experimental DFs from displacement data and a priori capacity (case study 1).

Beam No.	Strength I	Service II
Beam 1	5.08	5.04
Beam 2	2.36	2.13
Beam 3	1.94	1.75
Beam 4	2.36	2.13
Beam 5	4.53	4.50

Table 24. Rating factors using experimental DFs from displacement data and revised capacity (case study 1).

Beam No.	Strength I	Service II
Beam 1	5.24	5.20
Beam 2	2.12	1.97
Beam 3	1.85	1.70
Beam 4	2.26	2.07
Beam 5	4.68	4.64

The load ratings obtained through refined analysis are summarized in table 25 through table 28.

Table 25. Strength I FEM rating factors with a priori capacities (case study 1).

Beam No.	FE: A Priori	FE: Update Modal	FE: Update Displacement	FE: Update Strain
Beam 1	2.82	2.60	2.55	2.56
Beam 2	2.56	2.45	2.48	2.66
Beam 3	2.37	2.24	2.30	2.54
Beam 4	2.56	2.45	2.48	2.66
Beam 5	2.82	2.60	2.55	2.56

Table 26. Service II FEM rating factors with a priori capacities (case study 1).

Beam No.	FE: A Priori	FE: Update Modal	FE: Update Displacement	FE: Update Strain
Beam 1	2.59	2.42	2.32	2.60
Beam 2	2.24	2.15	2.14	2.43
Beam 3	2.17	2.05	2.09	2.41
Beam 4	2.24	2.15	2.14	2.43
Beam 5	2.59	2.42	2.32	2.60

Table 27. Strength I FEM rating factors with revised capacities (case study 1).

Beam No.	FE: A Priori	FE: Update Modal	FE: Update Displacement	FE: Update Strain
Beam 1	2.91	2.68	2.63	2.65
Beam 2	2.30	2.21	2.22	2.39
Beam 3	2.27	2.14	2.20	2.43
Beam 4	2.45	2.35	2.37	2.54
Beam 5	2.91	2.68	2.63	2.65

Table 28. Service II FEM rating factors with revised capacities (case study 1).

Beam No.	FE: A Priori	FE: Update Modal	FE: Update Displacement	FE: Update Strain
Beam 1	2.59	2.42	2.32	2.60
Beam 2	2.24	2.15	2.14	2.43
Beam 3	2.17	2.05	2.09	2.41
Beam 4	2.24	2.15	2.14	2.43
Beam 5	2.59	2.42	2.32	2.60

CASE STUDY 2: HAYMARKET BRIDGE (LTBP VIRGINIA PILOT BRIDGE)

Experimental Data

A diagnostic load test was performed on this structure in 2009. Strain and displacement were measured at 40 percent of span length under various loading conditions. Strain was also measured over the center support. Test vehicles were positioned as depicted in figure 46. For

load cases involving two test vehicles, trucks were spaced with 36 inches between the centerlines of adjacent front tires.

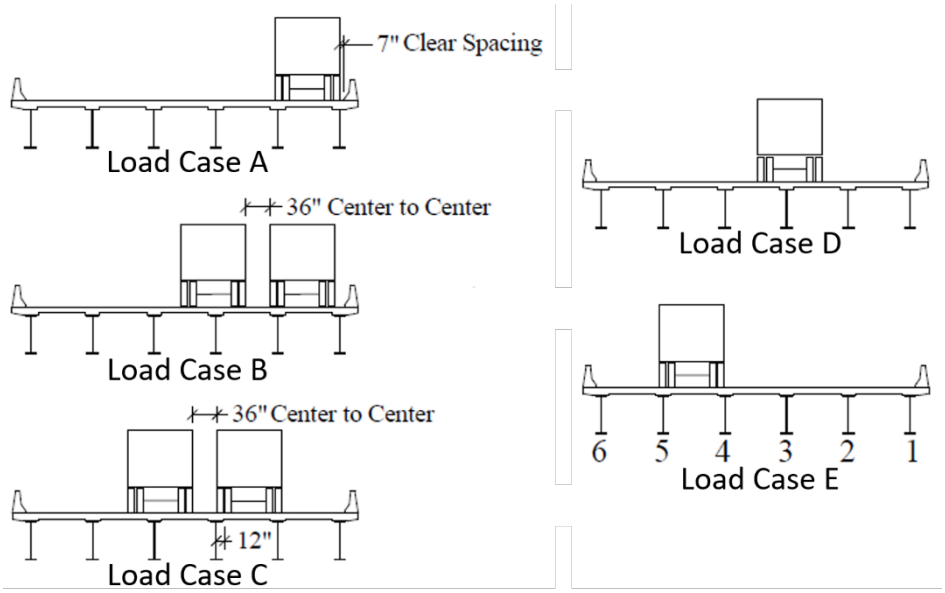

Source: FHWA.

Figure 46. Illustration. Diagnostic load test load configuration (case study 2).

The research team used data from load cases B and C to update FEMs and compute MBE adjustment factors. They also used data from load cases A, D, and E for computing experimental DFs. Table 29 through table 32 contain the maximum responses at 40 percent of span length for each load case.

Table 29. Experimental data: microstrain, span 1 (case study 2).

Load Case	A	B	C	D	E
Beam 1	84.23	110.00	57.80	29.00	9.35
Beam 2	59.70	106.00	81.50	41.90	16.43
Beam 3	27.80	84.53	95.28	55.63	27.53
Beam 4	13.30	46.60	76.25	38.93	49.63
Beam 5	0.97	22.05	43.68	20.90	54.95
Beam 6	0.00	11.78	30.05	12.58	41.88

Table 30. Experimental data: microstrain, span 2 (case study 2).

Load Case	A	B	C	D	E
Beam 1	72.68	91.45	48.35	25.20	8.03
Beam 2	61.25	105.00	75.90	38.78	14.25
Beam 3	29.95	85.00	90.75	54.90	26.28
Beam 4	15.23	50.05	81.58	40.23	50.75
Beam 5	3.25	24.15	46.85	21.75	56.03
Beam 6	0.00	8.75	28.25	14.60	42.85

Table 31. Experimental data: displacement (inches), span 1 (case study 2).

Load Case	A	B	C	D	E
Beam 1	0.317	0.409	0.268	0.137	0.044
Beam 2	0.250	0.392	0.331	0.186	0.089
Beam 3	0.143	0.265	0.262	0.178	0.127
Beam 4	0.093	0.278	0.368	0.186	0.227
Beam 5	0.036	0.129	0.185	0.103	0.174
Beam 6	0.003	0.068	0.161	0.073	0.208

Table 32. Experimental data: displacement (inches), span 2 (case study 2).

Load Case	A	B	C	D	E
Beam 1	0.320	0.427	0.277	0.149	0.044
Beam 2	0.252	0.383	0.323	0.189	0.087
Beam 3	0.179	0.391	0.397	0.228	0.149
Beam 4	0.102	0.265	—	0.192	0.216
Beam 5	0.037	0.132	0.207	0.107	0.193
Beam 6	0.000	0.069	0.170	0.081	0.222

—Data not available due to sensor malfunction.

NDE technologies implemented on this structure included GPR, IE, ER, USW, and HCP. IE provided the best indication of deck thickness and was therefore the only technology chosen for data integration. From the condition map generated from IE data (figure 29), the research team deduced that the concrete deck was in poor condition with widespread and significant delaminations. They therefore decided to err on the conservative side and reduce the deck thickness to 5 inches for all capacity calculations.

Integration Process

SLG Analysis

The research team first computed demands based on SLG analysis. The team applied loading as described in case study 1 and computed the moment at 0.4L and over the central support (negative-moment region). They used these values for comparison, for the MBE method, and for use in conjunction with experimental DFs.

Table 33 summarizes the demands as determined by SLG analysis.

Table 33. SLG demands (moment: lb-inches) (case study 2).

Response Location	Dead Load	Superimposed Dead Load	*LL + IM*
Interior girder, 0.4L	1.62E+07	2.04E+06	4.21E+07
Exterior girder, 0.4L	1.47E+07	2.04E+06	4.21E+07
Interior girder, negative moment	−2.89E+07	−3.64E+06	−4.76E+07
Exterior girder, negative moment	−2.62E+07	−3.64E+06	−4.76E+07

The team apportioned live-load demands to individual girders according to the following LRFD DFs (table 34).

Table 34. LRFD moment DFs (case study 2).

Girder Location	Single Lane	Multiple Lanes
Interior girder	0.4835	0.6635
Exterior girder	0.4933	0.5534

FE Analysis

Using the commercial software Strand7, the research team constructed an element-level FEM (figure 47) based on bridge geometry and assumed material properties provided in construction documents (Strand7 2013). This model employed one-dimensional, four-node beam elements for girders, diaphragms, and barriers. Each node had six DOF to permit all translations and rotations. This type of element can account for axial, bending, torsional, and shear deformations. The team discretized girders into 132 beam elements per girder per span. Cross-frame diaphragms were also modeled with beam elements. The team used 2D, four-node shell elements to model the deck and rigid links to enforce compatibility between girder and deck elements (thereby enforcing composite action).

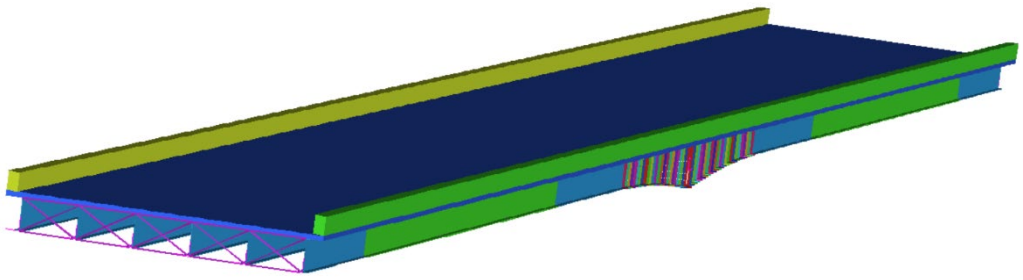

Source: FHWA.

Figure 47. Illustration. 3D FEM of bridge (case study 2).

The research team updated and calibrated the model with strain and displacement data. They then matched experimental data points with model responses to compare and evaluate model fit. They obtained simulated responses to load test configurations by positioning loads in the model to match the locations depicted in figure 46. The research team chose parameters that were uncertain (i.e., concrete stiffness) or influential to the responses being monitored. The team performed the calibration process as described in case study 1.

Table 35 contains the final parameter values that resulted from the model calibration process.

Table 35. Updated model parameter values (case study 2).

Parameter	Original Value	Update 1: Displacement	Update 2: Strain
Deck E (psi)	3.60E+06	5.06E+06	8.53E+06
Diaphragm E (psi)	2.90E+07	5.36E+06	2.90E+05
Barrier E (psi)	3.60E+06	1.50E+06	1.54E+06
Haunch stiffness (psi)	—	—	1.44E+04

—Parameter not altered during updating run.

The research team added a new beam element for the second updating run to represent the concrete haunch over the girders. The element was assigned geometry matching the width of the girder top flange and the average depth of the concrete haunch. The research team allowed stiffness to vary to account for uncertainty in both geometry and material properties.

The team used a priori and updated models to perform refined analyses to obtain load ratings. The stiffness of barrier and sidewalk elements was removed before solving for live-load demands. The model was rated with HL-93 loading positioned to create maximum force effect in the girders at 40 percent of span length and over the central support (AASHTO 2017, section Cl 3.6.1.2). The live-load composite moment was calculated according to equation 7.

Table 36 and table 37 summarize the demands as determined from refined analysis (i.e., finite-element analysis [FEA]).

Table 36. FEA positive-moment demands (lb-inches; 0.4L) (case study 2).

Beam No.	Dead Load	Superimposed Dead Load	*LL*: A Priori	*LL*: Update 1	*LL*: Update 2
Beam 1	1.23E+07	3.66E+06	1.65E+07	1.50E+07	1.47E+07
Beam 2	1.26E+07	2.62E+06	1.60E+07	1.55E+07	1.51E+07
Beam 3	1.28E+07	2.02E+06	1.61E+07	1.62E+07	1.58E+07
Beam 4	1.28E+07	2.01E+06	1.62E+07	1.63E+07	1.60E+07
Beam 5	1.26E+07	2.62E+06	1.62E+07	1.57E+07	1.54E+07
Beam 6	1.23E+07	3.63E+06	1.69E+07	1.54E+07	1.50E+07

Table 37. FEA negative-moment demands (lb-inches) (case study 2).

Beam No.	Dead Load	Superimposed Dead Load	*LL*: A Priori	*LL*: Update 1	*LL*: Update 2
Beam 1	−3.16E+07	−1.11E+07	−2.65E+07	−2.43E+07	−2.43E+07
Beam 2	−3.32E+07	−5.76E+06	−2.44E+07	−2.45E+07	−2.45E+07
Beam 3	−3.38E+07	−3.79E+06	−2.42E+07	−2.51E+07	−2.51E+07
Beam 4	−3.38E+07	−3.88E+06	−2.40E+07	−2.49E+07	−2.49E+07
Beam 5	−3.32E+07	−6.00E+06	−2.41E+07	−2.39E+07	−2.39E+07
Beam 6	−3.16E+07	−1.10E+07	−2.56E+07	−2.30E+07	−2.30E+07

MBE Method

The MBE allows for experimental data to be considered in the load-rating process by applying K to the theoretical (SLG) rating, as described by equation 2 (AASHTO 2018, Section 8.8.2.3).

The magnitude of the rating load for this bridge is 216 kips, but the load test applied only 98.2 kips; therefore, the ratio of test load to rating load is 0.45, and K_b is equal to 0.8. Table 38 provides the recorded strain (at 0.4L), the corresponding theoretical strain as determined by SLG methods (LL moment divided by the short-term, composite-section modulus for positive-moment region and LL moment divided by the noncomposite-section modulus for the negative-moment region), and the resulting MBE adjustment factors.

Table 38. MBE adjustment factors (case study 2).

Beam No.	Experimental Strain ($\mu\varepsilon$)	Theoretical Strain ($\mu\varepsilon$)	K_a	K
Beam 1	110.00	191.26	0.74	1.59
Beam 2	106.00	228.62	1.16	1.93
Beam 3	95.28	228.62	1.40	2.12
Beam 4	81.58	228.62	1.80	2.44
Beam 5	46.85	228.62	3.88	4.10
Beam 6	30.05	191.26	5.36	5.29

$\mu\varepsilon$ = microstrain.

Experimental DFs

Using equation 6, the research team computed experimental DFs based on responses from the three load cases in which a single truck was placed on the bridge. Because each lane was loaded individually, the experimental DF was calculated using the sum of response ratios from each load case. Table 39 and table 40 provide those response ratios.

Table 39. Strain responses ($\times 10^6$) and response ratios for calculating experimental DFs (case study 2).

Beam No.	Strain ($\mu\varepsilon$) (A)	Response Ratio	Strain ($\mu\varepsilon$) (D)	Response Ratio	Strain ($\mu\varepsilon$) (E)	Response Ratio	Response Ratio Sum
Beam 1	84.23	0.45	29.00	0.15	9.35	0.05	0.65
Beam 2	59.70	0.32	41.90	0.21	16.43	0.08	0.61
Beam 3	27.80	0.15	55.63	0.28	27.53	0.14	0.57
Beam 4	13.30	0.07	38.93	0.20	49.63	0.25	0.52
Beam 5	0.97	0.01	20.90	0.11	54.95	0.28	0.39
Beam 6	0.00	0.00	12.58	0.06	41.88	0.21	0.27

$\mu\varepsilon$ = microstrain.

Table 40. Displacement responses (inches) and response ratios for calculating experimental DFs (case study 2).

Beam No.	Displace-ment (A)	Response Ratio	Displace-ment (D)	Response Ratio	Displace-ment (E)	Response Ratio	Response Ratio Sum
Beam 1	0.317	0.38	0.137	0.16	0.250	0.05	0.59
Beam 2	0.250	0.30	0.186	0.22	0.143	0.10	0.62
Beam 3	0.143	0.17	0.178	0.21	0.093	0.15	0.52
Beam 4	0.093	0.11	0.186	0.22	0.036	0.26	0.59
Beam 5	0.036	0.04	0.103	0.12	0.003	0.20	0.36
Beam 6	0.003	0.00	0.073	0.08	0.208	0.24	0.33

There are three rating lanes for this bridge, and the corresponding multiple presence factor is 0.85. The response-ratio sums need only be multiplied by this multiple presence factor to obtain the experimental DFs, as summarized in table 41. Because the loading was not symmetrical about the centerline (longitudinal), the research team used the maximum of the DFs for exterior girders for both exterior girders to provide a more conservative estimate of demand distribution.

Table 41. Experimental DFs (case study 2).

Beam No.	Experimental DF: Strain	Experimental DF: Displacement	LRFD DF (Moment)
Beam 1	0.55	0.50	0.553
Beam 2	0.52	0.52	0.664
Beam 3	0.48	0.50	0.664
Beam 4	0.48	0.50	0.664
Beam 5	0.52	0.52	0.664
Beam 6	0.55	0.50	0.553

Capacity

The research team calculated the member capacities according to appropriate LRFD equations (AASHTO 2017). For the Strength I limit state, the positive-moment region capacity is defined as the plastic moment capacity of the composite section, which is computed as the sum of section plastic forces. In the negative-moment region, as well as positive-moment region for Service State II, the team checked the girders for yielding of the extreme fiber.

The team then integrated NDE results into the capacity calculations by revising the deck thickness to that determined through IE testing. Table 42 and table 43 summarize member capacities.

Table 42. A priori member capacities (case study 2).

Beam No.	Deck Thickness (Inches)	SB_{st} (Inches^3)	M_n (lb-Inches)	F_y (psi)
Beam 1	8.625	1.96E+03	1.24E+08	50,000
Beam 2	8.625	1.96E+03	1.24E+08	50,000
Beam 3	8.625	1.96E+03	1.24E+08	50,000
Beam 4	8.625	1.96E+03	1.24E+08	50,000
Beam 5	8.625	1.96E+03	1.24E+08	50,000
Beam 6	8.625	1.96E+03	1.24E+08	50,000

F_y = flange yield strength; M_n = nominal moment capacity (positive bending); SB_{st} = short-term composite-section modulus for the bottom fiber.

Table 43. Revised member capacities (case study 2).

Beam No.	Deck Thickness (Inches)	SB_{st} (Inches^3)	M_n (lb-Inches)	F_y (psi)
Beam 1	5	1.88E+03	9.51E+07	50,000
Beam 2	5	1.88E+03	1.10E+08	50,000
Beam 3	5	1.88E+03	1.10E+08	50,000
Beam 4	5	1.88E+03	1.10E+08	50,000
Beam 5	5	1.88E+03	1.10E+08	50,000
Beam 6	5	1.88E+03	9.51E+07	50,000

F_y = flange yield strength; M_n = nominal moment capacity (positive bending); SB_{st} = short-term composite-section modulus for the bottom fiber.

Load Ratings

The research team computed load ratings according to MBE equation 6A.4.2.1-1 (AASHTO 2018). Table 44 summarizes the various load and resistance factors used.

Table 44. Load and resistance factors for inventory load ratings (case study 2).

Limit State	System Factor	Condition Factor	Resistance Factor	*DC*	*DW*	*LL+IM*
Strength I	1	1	1	1.25	1.5	1.75
Service II	1	1	1	1.00	1.0	1.30

Table 45 and table 46 summarize the load-rating factors computed using SLG analysis without any adjustment factors applied.

Table 45. SLG inventory rating factors with a priori capacity (case study 2).

Beam No.	Strength I, Pos. Mom.	Service II, Pos. Mom.	Strength I, Neg. Mom.	Service II, Neg. Mom.
Beam 1	2.54	2.46	2.93	3.15
Beam 2	2.08	2.01	2.38	2.56
Beam 3	2.08	2.01	2.38	2.56
Beam 4	2.08	2.01	2.38	2.56
Beam 5	2.08	2.01	2.38	2.56
Beam 6	2.54	2.46	2.93	3.15

Pos. Mom. = positive-moment region; Neg. Mom. = negative-moment region.

Table 46. SLG inventory rating factors with revised capacity (case study 2).

Beam No.	Strength I, Pos. Mom.	Service II, Pos. Mom.	Strength I, Neg. Mom.	Service II, Neg. Mom.
Beam 1	1.82	2.37	2.93	3.15
Beam 2	1.79	1.93	2.38	2.56
Beam 3	1.79	1.93	2.38	2.56
Beam 4	1.79	1.93	2.38	2.56
Beam 5	1.79	1.93	2.38	2.56
Beam 6	1.82	2.37	2.93	3.15

Pos. Mom. = positive-moment region; Neg. Mom. = negative-moment region

Table 47 summarizes the load-rating factors when adjusted using the factors provided in the MBE (AASHTO 2018). A priori capacity values are used since the MBE does not provide recommendations for integrating field data in capacity estimates.

Table 47. MBE inventory rating factors (case study 2).

Beam No.	Strength I, Pos. Mom.	Service II, Pos. Mom.	Strength I, Neg. Mom.	Service II, Neg. Mom.
Beam 1	4.03	3.91	4.66	5.02
Beam 2	4.00	3.87	4.58	4.94
Beam 3	4.40	4.26	5.05	5.43
Beam 4	5.07	4.91	5.81	6.26
Beam 5	8.52	8.25	9.77	10.52
Beam 6	13.42	13.01	15.50	16.69

Pos. Mom. = positive-moment region; Neg. Mom. = negative-moment region.

Table 48 through table 51 summarize the load-rating factors when experimental DFs are used.

Table 48. Rating factors using experimental DFs from strain data and a priori capacity (case study 2).

Beam No.	Strength I, Pos. Mom.	Service II, Pos. Mom.	Strength I, Neg. Mom.	Service II, Neg. Mom.
Beam 1	2.56	2.48	2.95	3.18
Beam 2	2.64	2.56	3.03	3.26
Beam 3	2.86	2.77	3.28	3.53
Beam 4	2.86	2.77	3.28	3.53
Beam 5	2.64	2.56	3.03	3.26
Beam 6	2.56	2.48	2.95	3.18

Pos. Mom. = positive-moment region; Neg. Mom. = negative-moment region.

Table 49. Rating factors using experimental DFs from strain data and revised capacity (case study 2).

Beam No.	Strength I, Pos. Mom.	Service II, Pos. Mom.	Strength I, Neg. Mom.	Service II, Neg. Mom.
Beam 1	1.84	2.39	2.95	3.18
Beam 2	2.28	2.56	3.03	3.26
Beam 3	2.47	2.77	3.28	3.53
Beam 4	2.47	2.77	3.28	3.53
Beam 5	2.28	2.56	3.03	3.26
Beam 6	1.84	2.39	2.95	3.18

Pos. Mom. = positive moment region; Neg. Mom. = negative moment region.

Table 50. Rating factors (inventory) using experimental DFs from displacement data and a priori capacity (case study 2).

Beam No.	Strength I, Pos. Mom.	Service II, Pos. Mom.	Strength I, Neg. Mom.	Service II, Neg. Mom.
Beam 1	2.82	2.73	3.26	3.51
Beam 2	2.63	2.55	3.02	3.25
Beam 3	2.76	2.67	3.17	3.41
Beam 4	2.76	2.67	3.17	3.41
Beam 5	2.63	2.55	3.02	3.25
Beam 6	2.82	2.73	3.26	3.51

Pos. Mom. = positive moment region; Neg. Mom. = negative moment region.

Table 51. Rating factors (inventory) using experimental DFs from displacement data and revised capacity (case study 2).

Beam No.	Strength I, os. Mom.	Service II, Pos. Mom.	Strength I, Neg. Mom.	Service II, Neg. Mom.
Beam 1	2.02	2.63	3.26	3.51
Beam 2	2.28	2.45	3.02	3.25
Beam 3	2.38	2.57	3.17	3.41
Beam 4	2.38	2.57	3.17	3.41
Beam 5	2.28	2.45	3.02	3.25
Beam 6	2.02	2.63	3.26	3.51

Pos. Mom. = positive moment region; Neg. Mom. = negative moment region.

The load ratings obtained through refined analysis are summarized in table 52 through table 54.

Table 52. FEM rating factors for positive moment (inventory) with a priori capacities (case study 2).

Beam No.	A Priori: Strength I	Update Displacement: Strength I	Update Strain: Strength I	A Priori: Service II	Update Displacement: Service II	Update Strain: Service II
Beam 1	3.61	3.97	4.07	3.34	3.79	4.01
Beam 2	3.76	3.88	3.98	3.72	3.87	3.98
Beam 3	3.76	3.74	3.82	3.72	3.74	3.86
Beam 4	3.73	3.71	3.79	3.69	3.72	3.83
Beam 5	3.71	3.82	3.91	3.65	3.82	3.93
Beam 6	3.54	3.88	3.97	3.29	3.70	3.91

Negative-moment capacity remained unchanged; therefore, FEM ratings for the negative-moment region were as provided in table 53.

Table 53. FEM rating factors for negative moment (inventory) with a priori capacities (case study 2).

Beam No.	A Priori: Strength I	Update Displacement: Strength I	Update Strain: Strength I	A Priori: Service II	Update Displacement: Service II	Update Strain: Service II
Beam 1	2.81	3.08	3.14	3.03	3.31	3.39
Beam 2	3.14	3.17	3.24	3.38	3.42	3.49
Beam 3	3.09	3.05	3.13	3.33	3.28	3.37
Beam 4	3.06	3.05	3.15	3.30	3.28	3.40
Beam 5	2.94	3.06	3.18	3.17	3.30	3.42
Beam 6	2.77	3.17	3.37	2.98	3.42	3.63

Table 54. FEM rating factors for positive moment (inventory) with revised capacities (case study 2).

Beam No.	A Priori: Strength I	Update Displacement: Strength I	Update Strain: Strength I	A Priori: Service II	Update Displacement: Service II	Update Strain: Service II
Beam 1	2.60	2.86	2.93	3.34	3.79	4.01
Beam 2	3.27	3.37	3.45	3.72	3.87	3.98
Beam 3	3.27	3.25	3.32	3.72	3.74	3.86
Beam 4	3.25	3.22	3.29	3.69	3.72	3.83
Beam 5	3.22	3.32	3.40	3.65	3.82	3.93
Beam 6	2.55	2.79	2.86	3.29	3.70	3.91

CASE STUDY 3: THE BEAST (FIRST SPECIMEN)

Experimental Data

The BEAST live-load system performs continuous loading of the specimen. The test loading consists of a carriage with the same wheelset as would be on a truck. The carriage is able to exert 60 kips of downward force on the bridge deck while moving at speeds up to 20 mph. Periodically, the carriage will make a slow pass (<3 mph), at which point the data acquisition system is automatically triggered to record data at a sampling rate of 20 Hz. This low-speed loading provides quasi-static load-response conditions.

The travel path of the carriage has been repositioned several times over the past several months of testing. Those four load path positions are described in figure 48.

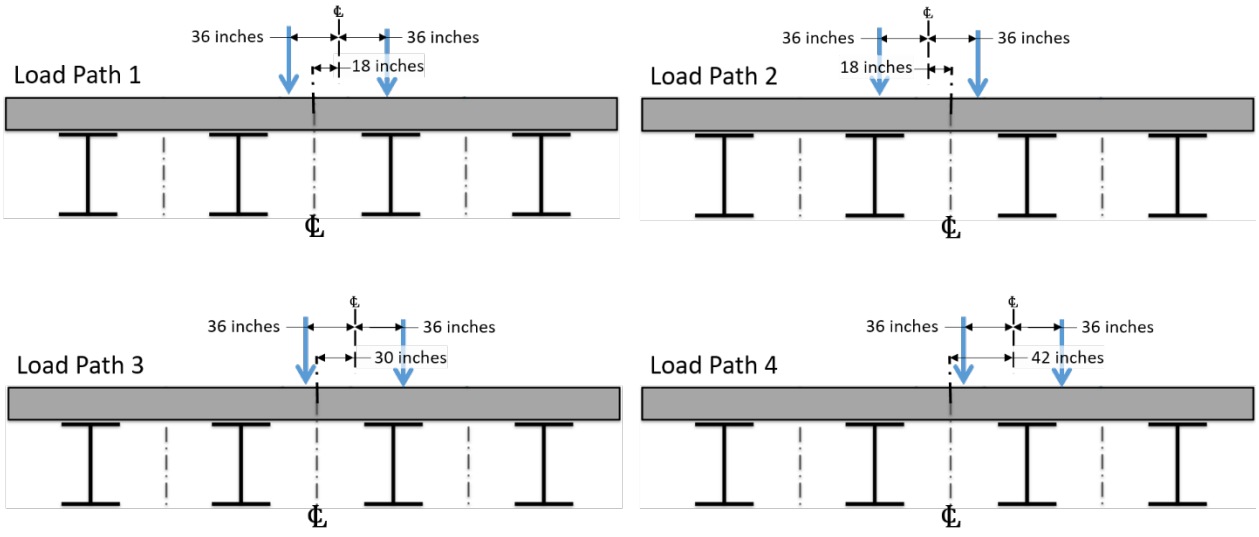

Source: FHWA.
℄ = centerline.

Figure 48. Illustration. Load path positions (case study 3).

Table 55 indicates the midspan strain responses due to the carriage traversing the bridge along these load paths.

Table 55. Microstrain on the bottom flange at midspan (case study 3).

Beam No.	LP 1	LP 2	LP 3	LP 4
Beam 1	60.06	96.78	52.90	43.46
Beam 2	133.54	167.43	125.78	113.31
Beam 3	166.03	139.67	169.75	175.19
Beam 4	106.40	68.19	115.85	133.38

LP = load path.

GPR scans of the deck revealed that the concrete cover over rebar was only 1.25 inches in the center portion of the deck rather than the specified 2-inch cover, as evidenced by the GPR condition map shown in figure 34.

The compressive strength of the deck concrete was also tested. As per ASTM C39, three specimens per truck were tested at 3, 7, 28, and 56 days. The results of these tests are provided in table 56 (ASTM International 2020). The minimum value reported for the 56-day results was used for revising capacity estimates.

Table 56. Compressive strength of deck concrete specimens (case study 3).

Truck No.	Avg. f'_c 3 Days (psi)	Stand. Dev.	Avg. f'_c 7 Days (psi)	Stand. Dev.	Avg. f'_c 28 days (psi)	Stand. Dev.	Avg. f'_c 56 Days (psi)	Stand. Dev.
Truck 1	3,235	456	4,136	319	4,868	105	5,149	218
Truck 2	3,566	380	4,260	301	5,402	561	5,931	122
Truck 3	3,040	340	3,946	77	4,717	191	4,936	129
Truck 4	3,914	72	4,542	196	5,269	276	5,887	142

f'_c = compressive strength.

Integration Process

SLG Analysis

The research team first computed demands based on SLG analysis. The team applied loading as described in case study 1 and computed the moment at midspan. They used these values for comparison, for the MBE method, and for use in conjunction with experimental DFs.

Table 57 summarizes SLG demands.

Table 57. SLG demands (moment: lb-inches) (case study 3).

Response Location	Dead Load	Superimposed Dead Load	Wearing Surface	Live Load
Interior girder	3.18E+06	3.15E+05	0	1.23E+07
Exterior girder	2.62E+06	3.15E+05	0	1.23E+07

The research team apportioned live-load demands to individual girders according to the LRFD DFs provided in table 58.

Table 58. LRFD moment DFs (case study 3).

Girder Location	Single Lane	Multiple Lanes
Interior girder	0.444	0.592
Exterior girder	0.630	0.549

FE Analysis

Using the commercial software Strand7, the research team constructed an element-level FEM (figure 49) based on bridge geometry and assumed material properties provided in construction documents (Strand7 2013). This model employed one-dimensional, two-node beam elements for girders and diaphragms. Each node had six DOF to permit all translations and rotations. This type of element can account for axial, bending, torsional, and shear deformations. The team discretized each girder into 60 beam elements and used 2D, four-node shell elements to model the deck and curbs. The deck was discretized into 2,160 shell elements. The team used rigid links to enforce compatibility between girder and deck elements (thereby enforcing composite action).

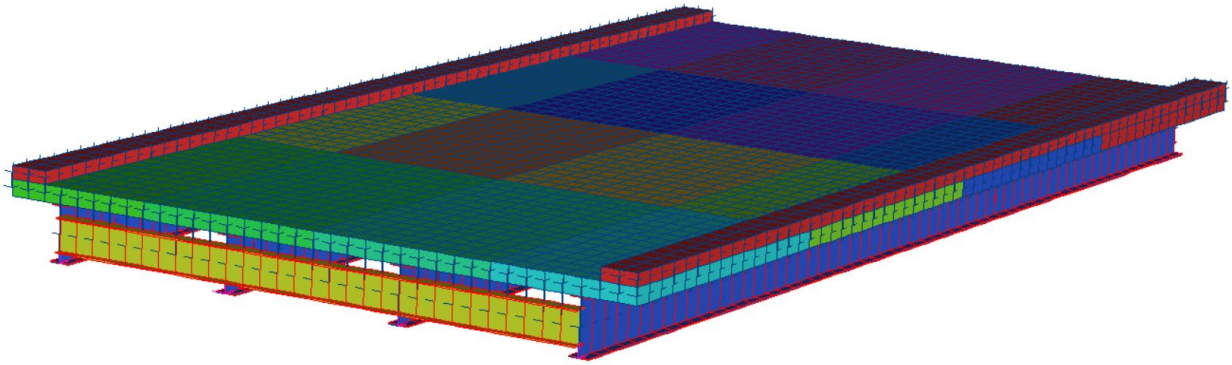

Source: FHWA.

Figure 49. Illustration. 3D FEM of bridge (case study 3).

The team updated and calibrated the model with strain data from all four load paths. They then matched the experimental data points with model responses to compare and evaluate model fit. Simulated responses to rolling live-load configurations were obtained by positioning loads in the model to match the locations depicted in figure 48. The team chose and monitored parameters whose impacts were uncertain (i.e., concrete stiffness) or influential to the responses. The research team performed the calibration process as described in case study 1.

Table 59 contains the final parameter values that were obtained through the model calibration process. Note that sidewalk thickness was updated to account for a thicker deck at the overhangs.

Table 59. Updated model parameter values (case study 3).

Parameter	Original Value	Update 1	Update 2	Update 3
Sidewalk thickness (inches)	6.00	30.00	39.76	39.76
Diaphragm E (psi)	2.90E+07	2.90E+06	0	0
Deck E (psi)	4.97E+06	8.05E+06	5.87E+06	5.87E+06

For the third update, the team segmented the deck into a 4- by 4-ft grid, with the thickness of each portion able to be individually varied by the optimization algorithm. As a result, the final values for deck thickness vary based on location. The a priori model, conversely, had a deck thickness of 8 inches. Table 60 provides the updated thickness for each portion of deck.

Table 60. Update three resulting deck thicknesses (inches) (case study 3).

Transverse Location	0 to ¼ Span	¼ Span to Midspan	Midspan to ¾ Span	¾ Span to End
Over beam 4	5.13	5.95	8.32	9.38
Over beam 3	12.0	8.91	8.21	8.03
Over beam 2	9.07	8.01	7.67	4.00
Over beam 1	10.8	6.95	8.65	12.0

The study used a priori and updated models to perform a refined analysis to obtain load ratings. The stiffness of the sidewalk was discounted by reducing the thickness of the sidewalk elements by an amount equal to the measured sidewalk thickness of 6 inches before solving for live-load demands. The model was rated with HL-93 loading positioned to create maximum force effect at midspan of the girders (AASHTO 2017, section Cl 3.6.1.2). The team calculated composite moment for live loads according to equation 7.

Table 61 summarizes the demands as determined from refined (i.e., FE) analysis.

Table 61. FEA demands (moment: lb-inches) (case study 3).

Beam No.	Dead Load	Superimposed Dead Load	LL: A Priori	LL: Update 1	LL: Update 2	LL: Update 3
Beam 1	2.73E+06	2.26E+05	5.47E+06	4.16E+06	3.39E+06	3.68E+06
Beam 2	3.01E+06	1.73E+05	5.76E+06	4.62E+06	4.22E+06	4.53E+06
Beam 3	2.98E+06	1.73E+05	5.76E+06	4.62E+06	4.22E+06	4.29E+06
Beam 4	2.76E+06	2.27E+05	5.47E+06	4.16E+06	3.39E+06	3.49E+06

MBE Method

The MBE allows for experimental data to be considered in the load-rating process by applying adjustment factor K to the theoretical (i.e., SLG) rating as described by equation 2 (AASHTO 2018, section 8.8.2.3).

The magnitude of the rating load for this bridge is 144 kips. The live-load carriage applied only 60 kips. Therefore, the ratio of test load to rating load is 0.42, and K_b is equal to 0.8. Table 62 provides the enveloped midspan strain, the corresponding theoretical strain as determined by

SLG methods (*LL* moment divided by the short-term composite-section modulus), and the resulting MBE adjustment factors.

Table 62. MBE adjustment factors (case study 3).

Beam No.	Experimental Strain ($\mu\varepsilon$)	Theoretical Strain ($\mu\varepsilon$)	K_a	K
Beam 1	96.783	508.138	4.250	4.400
Beam 2	167.431	351.834	1.101	1.881
Beam 3	175.192	351.834	1.008	1.807
Beam 4	133.380	508.138	2.810	3.248

$\mu\varepsilon$ = microstrain.

Experimental DFs

The research team computed experimental DFs based on responses from load paths 2 and 4. The two load paths do overlap slightly and are therefore not good cases for experimental DFs as they will overestimate the amount of load a single girder would be expected to experience during a rating-load configuration. However, this method is still shown for demonstration purposes. The team computed factors according to equation 7. Because each lane was loaded individually, the experimental DF was calculated using the sum of response ratios from each load case. Table 63 provides those response ratios.

Table 63. Strain responses ($\times 10^6$) and response ratios for calculating experimental DFs (case study 3).

Beam No.	Strain, Load Path 2 ($\mu\varepsilon$)	Response Ratio	Strain, Load Path 4 ($\mu\varepsilon$)	Response Ratio	Response Ratio Sum
Beam 1	96.78	0.21	43.46	0.09	0.30
Beam 2	167.43	0.35	113.31	0.24	0.60
Beam 3	139.67	0.30	175.19	0.38	0.67
Beam 4	68.19	0.14	133.38	0.29	0.43

$\mu\varepsilon$ = microstrain.

There are two rating lanes for this bridge, and the corresponding multiple presence factor is 1.0. The response ratio sums need only be multiplied by this multiple presence factor to obtain the experimental DFs, as summarized in table 64. Because the loading was not symmetrical about the centerline (longitudinal), the research team used the maximum of the DFs for exterior girders for both exterior girders in attempt to provide a more conservative estimate of demand distribution.

Table 64. Experimental DFs (case study 3).

Beam No.	Experimental DF	LRFD DF (Moment)
Beam 1	0.43	0.549
Beam 2	0.60	0.592
Beam 3	0.67	0.592
Beam 4	0.43	0.549

Capacity

The research team calculated member capacities according to appropriate LRFD equations (AASHTO 2017). For the Strength I limit state, the positive moment region capacity was defined as the plastic moment capacity of the composite section, which was computed as the sum of section plastic forces. For Service State II, the girders were checked for yielding of the extreme tension fiber.

The research team integrated NDE results into the capacity calculations by revising the deck thickness to that determined through GPR and the concrete compressive strength (f'_c) to that measured through material testing. Table 65 and table 66 summarize the capacities of the composite members.

Table 65. A priori member capacities (case study 3).

Beam No.	Deck f'_c (psi)	Deck Thickness (Inches)	SB_{st} (Inches^3)	M_n (lb-Inches)	F_y (psi)
Beam 1	4,500	8	354.0	24,825,200	50,000
Beam 2	4,500	8	360.3	25,766,286	50,000
Beam 3	4,500	8	360.3	25,766,286	50,000
Beam 4	4,500	8	354.0	24,825,200	50,000

F_y = flange yield strength; M_n = nominal moment capacity (positive bending); SB_{st} = short-term composite-section modulus for the bottom fiber.

Table 66. Revised member capacities (case study 3).

Beam No.	Deck f'_c (psi)	Deck Thickness (Inches)	SB_{st} (Inches^3)	M_n (lb-Inches)	F_y (psi)
Beam 1	4,936	7.25	344.2	24,304,181	50,000
Beam 2	4,936	7.25	349.9	25,041,222	50,000
Beam 3	4,936	7.25	349.9	25,041,222	50,000
Beam 4	4,936	7.25	344.2	24,304,181	50,000

F_y = flange yield strength; M_n = nominal moment capacity (positive bending); SB_{st} = short-term composite-section modulus for the bottom fiber.

Load Ratings

The research team computed load ratings according to MBE equation 6A.4.2.1-1 (AASHTO 2018). Table 67 summarizes the various load and resistance factors used.

Table 67. Load and resistance factors for inventory load ratings (case study 3).

Limit State	System Factor	Condition Factor	Resistance Factor	DL	DLW	LL
Strength I	1	1	1	1.25	1.5	1.75
Service II	1	1	1	1.00	1.0	1.30

Table 68 summarizes the load-rating factors, which the research team computed using an SLG analysis without any adjustment factors applied.

Table 68. SLG rating factors (case study 3).

Beam No.	Strength I A Priori Capacity	Service II A Priori Capacity	Strength I Revised Capacity	Service II Revised Capacity
Beam 1	1.56	1.20	1.52	1.16
Beam 2	1.68	1.19	1.62	1.16
Beam 3	1.68	1.19	1.62	1.16
Beam 4	1.56	1.20	1.52	1.16

Table 69 summarizes the load-rating factors when adjusted using the factors provided in the MBE (AASHTO 2018).

Table 69. MBE rating factors (case study 3).

Beam No.	Strength I	Service II
Beam 1	6.868	5.261
Beam 2	3.159	2.246
Beam 3	3.034	2.157
Beam 4	5.069	3.883

Table 70 summarizes the load-rating factors when experimental DFs are used.

Table 70. Rating factors using experimental DFs from strain data (case study 3).

Beam No.	Strength I A Priori Capacity	Service II A Priori Capacity	Strength I Revised Capacity	Service II Revised Capacity
Beam 1	2.28	1.75	2.22	1.70
Beam 2	1.66	1.18	1.61	1.15
Beam 3	1.48	1.05	1.43	1.02
Beam 4	2.28	1.75	2.22	1.70

The load ratings obtained through refined analysis are summarized in table 71 and table 72.

Table 71. FEM rating factors with a priori capacities (case study 3).

Beam No.	A Priori Strength I	Update 1 Strength I	Update 2 Strength I	Update 3 Strength I	A Priori Service II	Update 1 Service II	Update 2 Service II	Update 3 Service II
Beam 1	2.21	2.90	3.56	3.28	1.55	2.09	2.52	2.24
Beam 2	2.16	2.69	2.95	2.75	1.43	1.81	1.92	1.83
Beam 3	2.17	2.70	2.96	2.91	1.43	1.81	1.93	1.92
Beam 4	2.20	2.89	3.55	3.46	1.55	2.08	2.52	2.43

Table 72. FEM rating factors with revised capacities (case study 3).

Beam No.	A Priori Strength I	Update 1 Strength I	Update 2 Strength I	Update 3 Strength I	A Priori Service II	Update 1 Service II	Update 2 Service II	Update 3 Service II
Beam 1	2.15	2.83	3.47	3.20	1.55	2.09	2.52	2.24
Beam 2	2.09	2.61	2.85	2.66	1.43	1.81	1.92	1.83
Beam 3	2.09	2.61	2.86	2.81	1.43	1.81	1.93	1.92
Beam 4	2.15	2.82	3.46	3.37	1.55	2.08	2.52	2.43

APPENDIX B. EFFECT OF LOCAL DETERIORATION ON MEMBER CAPACITY

The research team performed sensitivity studies to evaluate the influence of local deterioration on capacity. The following types of deterioration were investigated:

- Deck delamination.
- Local loss of composite action (associated with significant deck deterioration).
- Loss of prestressing strands.

For this application, the team employed a cross-sectional model termed a "fiber model." This model is commonly used for nonlinear flexural analysis of complex cross sections, which it handles by discretizing the cross section into several elements referenced to specific stress–strain models. By incrementally increasing the curvature on the cross section while maintaining a linear strain profile (plane-sections-remain-plane) and iterating until equilibrium is satisfied, researchers obtained a nonlinear moment–curvature response.

To quantify the sensitivity of capacity to local deterioration, the research team calculated the percentage difference between the capacity associated with an intact model and that for a deteriorated model. The team also considered the influence of deterioration on the ductility and failure mode of the element. In some cases, the deterioration required a change in the assumed failure mode at which the capacity was computed and, as a result, the ductility associated with that limit state changed significantly. These secondary effects were also considered.

FIBER MODELS

The process for conducting a numerical analysis with fiber models included the following steps:

1. Designing notional bridges to obtain realistic section geometry.
2. Computing permanent demands (e.g., dead load, prestressing).
3. Creating a model by discretizing the cross section into individual "fibers," with each assigned a material model (i.e., stress–strain relationship).
4. Developing a section moment–curvature relationship.

The research team completed numerous notional bridge designs according to the *AASHTO LRFD Bridge Design Specifications* (2010) to provide a variety of bridge configurations. Each design had a deck thickness of 8 inches. Bridge span length, girder spacing, and girder type varied, as described in table 73.

Table 73. Bridge design parameters.

Parameter	Values
Span length	50 ft, 100 ft, 150 ft
Girder spacing	6 ft, 8 ft, 12 ft
Girder type	Steel, prestressed concrete

Full factorial sampling of these bridge parameter sets yielded 17 design configurations (no prestressed design for 150-ft span length and 12-ft girder spacing). Table 74 summarizes the designs.

Table 74. Notional bridge designs.

Length (Inches)	Bridge Width (Inches)	Girder Spacing (Inches)	Number of Girders	Beam Type	Beam Depth (Inches)	Section Name
600	432	144	4	AASHTO	45	AASHTO3
600	504	72	8	AASHTO	36	AASHTO2
600	480	96	6	AASHTO	36	AASHTO2
1,200	432	144	4	AASHTO	63	AASHTO5
1,200	504	72	8	AASHTO	54	AASHTO4
1,200	480	96	6	AASHTO	54	AASHTO4
1,800	504	72	8	AASHTO	72	AASHTO6
1,800	480	96	6	AASHTO	72	AASHTO6
600	432	144	4	Rolled	27.3	W27X114
600	504	72	8	Rolled	26.7	W27X84
600	480	96	6	Rolled	26.7	W27X84
1,200	432	144	4	Plate	48	Plate
1,200	504	72	8	Plate	48	Plate
1,200	480	96	6	Plate	48	Plate
1,800	432	144	4	Plate	72	Plate
1,800	504	72	8	Plate	72	Plate
1,800	480	96	6	Plate	72	Plate

The research team discretized composite cross sections into ½- by ½-inch fibers. These included girders, deck, and prestressing strands (where appropriate). Deck reinforcing was not included in the fiber models. Concrete fibers were assigned a Hognestad material (1951) model with a compressive strength of 5,000 psi and an ultimate crushing strain of 0.0038. Steel fibers were assigned an elasto-plastic model with an elastic modulus of 29,000 kilopounds per square inch (ksi) and a yield strength of 36,000 psi. Prestressing steel fibers were assigned the Precast/Prestressed Concrete Institute model (2017) for low-relaxation steel with an elastic modulus of 28,500 ksi and an ultimate strength of 270 ksi.

Using MATLAB scripts, the team performed the iterative process of determining the moment associated with a specified curvature automatically. They implemented delaminations and loss of prestressing by forcing the stress in corresponding fibers to remain at zero, thereby removing the contribution of those fibers. The team implemented loss of composite action by allowing the strain profile to be discontinuous at the interface between deck and girder while limiting the total force in the deck depending upon the degree of composite action. For the case of 50 percent composite action, only 50 percent of the deck force at the capacity limit state was permitted to develop in the deck, and the girder strain profile was determined according to the specified curvature and to maintain equilibrium of the entire section (deck included).

DELAMINATIONS

The team implemented delaminations in the fiber models by reducing the deck thickness by an amount equal to the depth of delamination, thereby removing elements within the delamination area. They investigated delaminations over the full effective width and up to 4 inches.

Figure 50 and figure 51 illustrate the effect delaminations have on the moment–curvature response of a cross section.

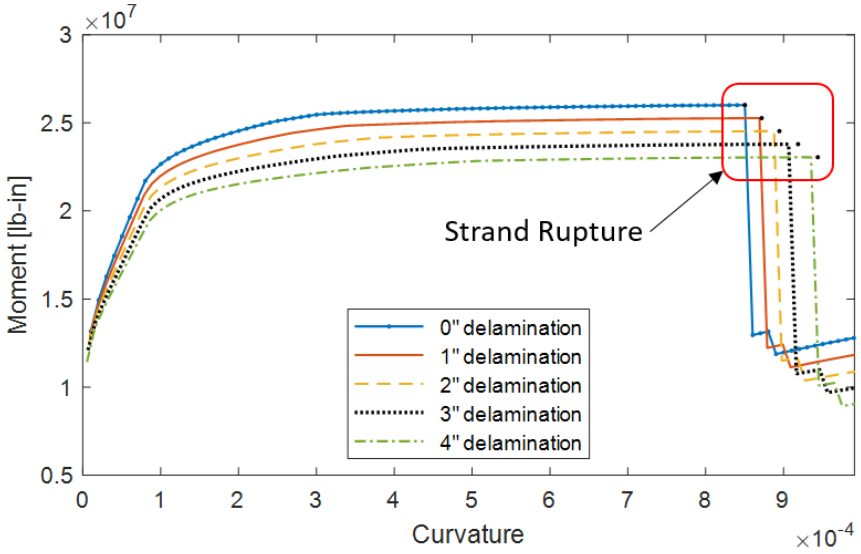

Source: FHWA.

Figure 50. Graph. Moment–curvature relationship for prestressed composite section with a 50-ft span length and 8-ft girder spacing.

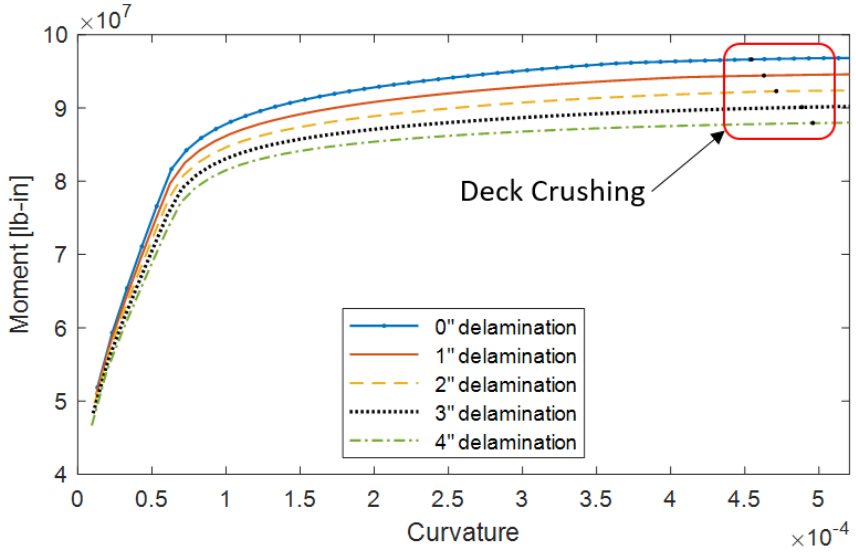

Source: FHWA.

Figure 51. Graph. Moment–curvature relationship for prestressed composite section with a 100-ft span length and 8-ft girder spacing.

The team computed this change in ultimate moment due to delamination for each section. Figure 52 and figure 53 illustrate the effect of delamination on ultimate moment capacity.

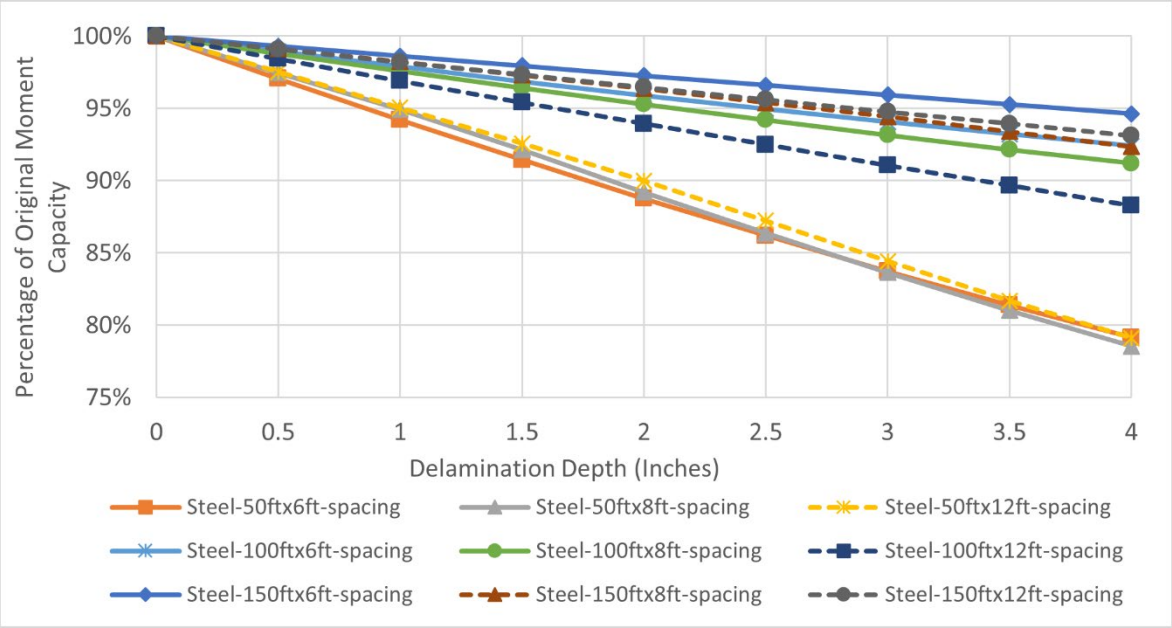

Source: FHWA.
Note: Vertical axis is abbreviated to enable visual discernment of series.

Figure 52. Graph. Effect of delaminations on ultimate moment capacity for steel composite sections.

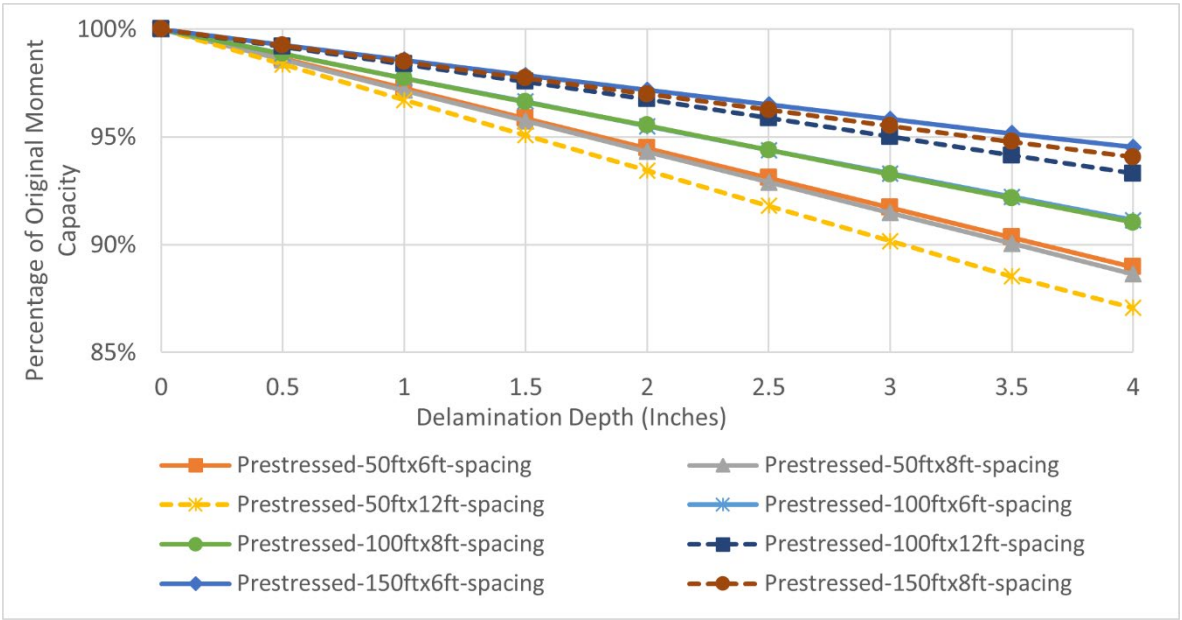

Source: FHWA.
Note: Vertical axis is abbreviated to enable visual discernment of series.

Figure 53. Graph. Effect of delaminations on ultimate moment capacity for prestressed composite sections.

The research team also examined the effect of delaminations on the curvature at ultimate moment. Figure 54 and figure 55 illustrate that effect.

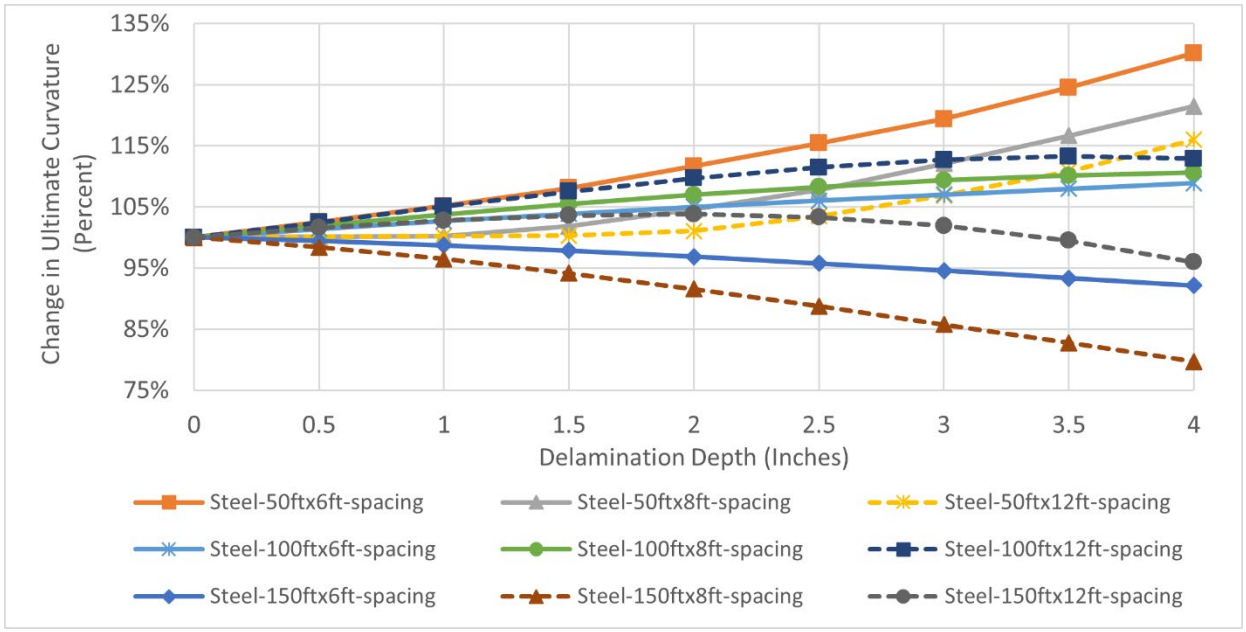

Source: FHWA.
Note: Vertical axis is abbreviated to enable visual discernment of series.

Figure 54. Graph. Effect of delaminations on curvature at ultimate moment for steel composite sections.

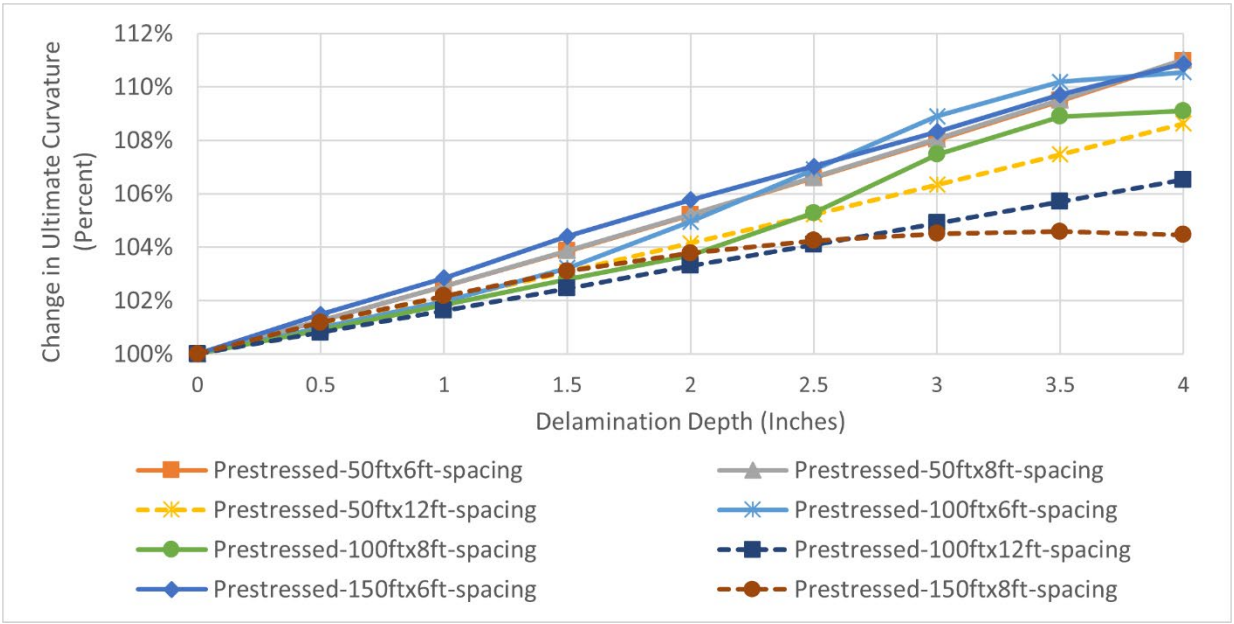

Source: FHWA.
Note: Vertical axis is abbreviated to enable visual discernment of series.

Figure 55. Graph. Effect of delaminations on curvature at ultimate moment for prestressed composite sections.

The team then compared the reduction in ultimate moment, as determined by the fiber model, to the reduction in moment capacity, as determined using LRFD equations with reduced deck thickness. From this comparison (figure 20), the research team concluded that the existing LRFD capacity equations are sufficient for estimating the capacity of deteriorated sections by appropriately revising section geometry.

LOSS OF COMPOSITE ACTION

The research team investigated composite action at levels of 0, 50, and 100 percent. These percentages corresponded to the upper limit of deck force that was permitted to be developed in the deck fibers as a percentage of maximum force for which shear studs would be designed. For steel girder sections, this maximum force was the minimum of the girder's plastic force (equation 8) and the deck plastic force (equation 9). For prestressed girder sections, this maximum deck force was the minimum of the plastic force of the strands (equation 10) and the deck plastic force (equation 9).

$$P_s = A_s \times F_y \tag{8}$$

Where:

P_s = plastic force in steel.
A_s = area of steel.
F_y = yield strength of steel.

$$P_d = 0.85 \times f'_c \times \beta \times A_d \tag{9}$$

Where:

P_d = plastic force in deck.
f'_c = compressive strength of concrete.
β = concrete property related to the depth of the stress block.
A_d = area of deck.

$$P_{PS} = A_s \times F_u \tag{10}$$

Where:

P_{PS} = plastic force in prestressing strands.
A_{PS} = area of prestressing strands.
F_u = ultimate tensile strength of steel.

The team first computed the moment–curvature relationship assuming a continuous strain profile (i.e., acting compositely): if the deck force exceeded the specified maximum force, the moment was recomputed with non-composite logic. In this process, the strain profile in the deck was first determined using an optimization algorithm that satisfied the specified curvature and resulted in a total deck force equal to the specified maximum force. The strain profile in the girder was subsequently determined according to the specified curvature, and that resulted in an equilibrium of all section forces (including deck force).

The capacity-limit states for the sections depended on the state of composite action. Because the LRFD specifications do not provide recommendations for sections with partial composite action, the team took the ultimate moment capacity at the first point of failure (e.g., yield or crushing) of the deck or girder.

Table 75 summarizes the limit states for the different bridge types and composite conditions.

Table 75. Limit states for varying degrees of composite action.

Section Type	Capacity Limit State
Steel, composite	First crushing of concrete at top of deck ($\varepsilon_C = 0.003$)
Steel, partially composite	Minimum of first deck crushing and first girder yield
Steel, noncomposite	First yield ($F_y = 36{,}000$ psi) of girder (extreme tension fiber)
Prestressed, composite	Minimum of first deck crushing or first strand rupture
Prestressed, partially composite	Minimum of first deck crushing, girder crushing or strand rupture
Prestressed, noncomposite	First crushing at top of girder

ε_C = crushing strain in concrete; F_y = yield strength.

Figure 56 and figure 57 illustrate the effect that loss of composite action may have on the moment–curvature response of a section. From these plots, it is evident that the change in capacity may be more influenced by the change in limit state than by the change in load-response behavior.

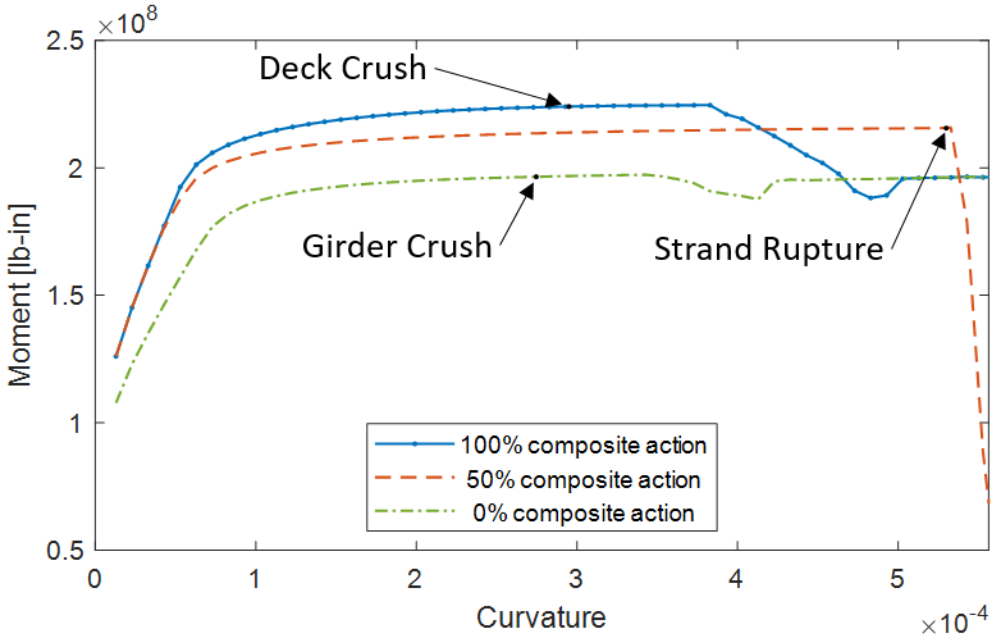

Source: FHWA.

Figure 56. Graph. Moment–curvature relationship for prestressed section with a 150-ft span length and 8-ft girder spacing subjected to loss of composite action.

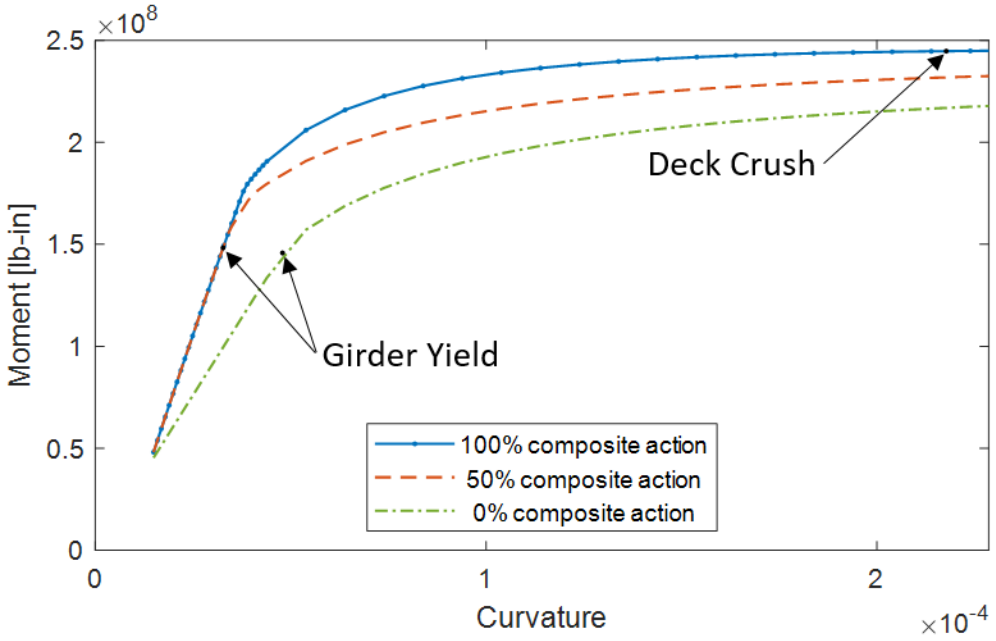

Source: FHWA.

Figure 57. Graph. Moment–curvature relationship for steel section with a 150-ft span length and 8-ft girder spacing subjected to loss of composite action.

Figure 58 summarizes the effect of loss of composite action on capacity for all steel and prestressed sections.

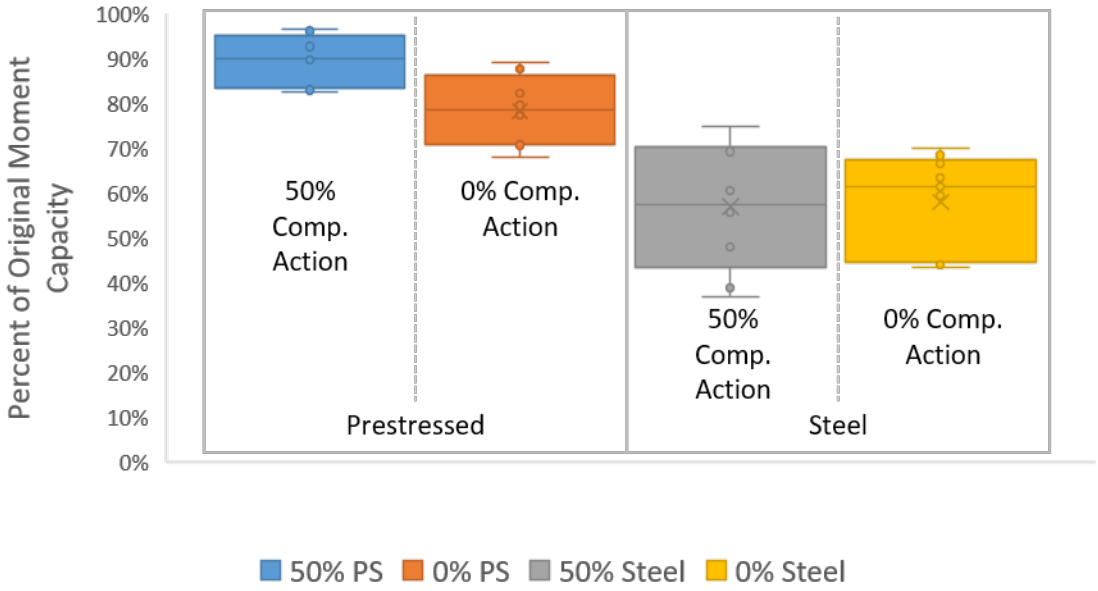

Source: FHWA.
PS = prestressed.

Figure 58. Graph. Effect of loss of composite action on ultimate moment capacity.

The change in limit state particularly affects the moment capacity for steel girder sections as the limit state becomes first yield of the steel. This change also significantly reduces ductility as the curvature at the yield-limit state is significantly less, as is evident in figure 59.

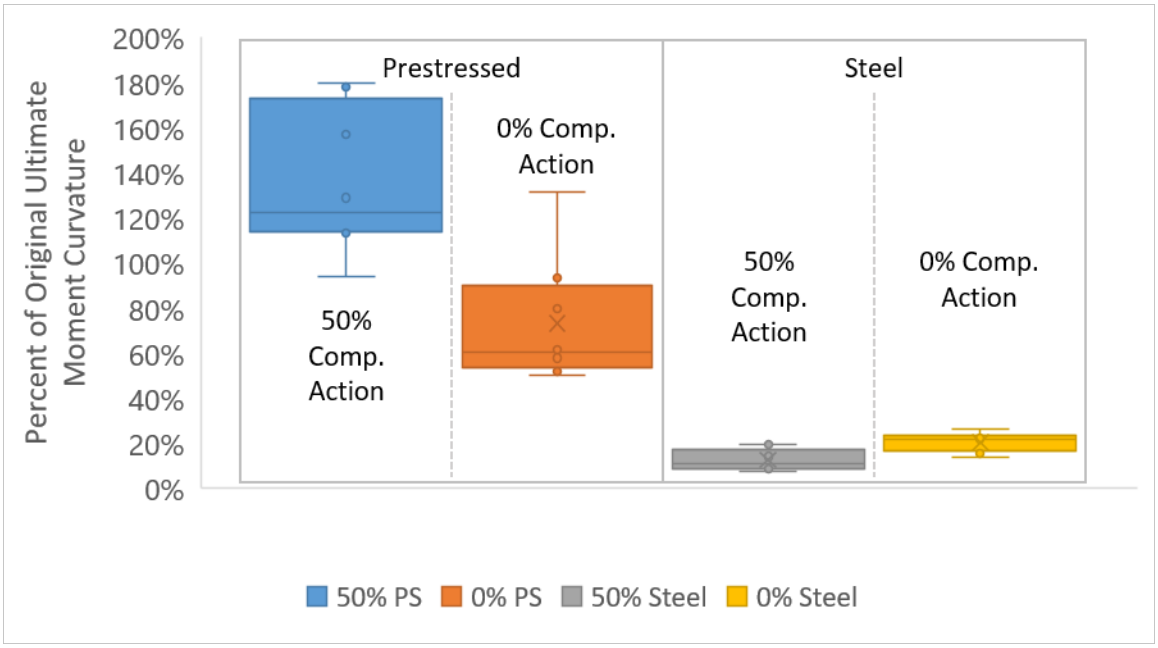

Source: FHWA.
PS = prestressed.

Figure 59. Graph. Effect of loss of composite action on curvature at ultimate moment.

LOSS OF PRESTRESSING STRANDS

Loss of up to four strands was considered for all prestressing sections. Strand loss was represented in the fiber models by removing the fibers that corresponded to the lost strands. Strands were removed from the bottom up as these strands are experiencing the greatest stress (and demands due to moisture and chloride ingress) and thus are more likely to deteriorate. Figure 60 and figure 61 illustrate the effect strand loss has on a section's moment–curvature relationship.

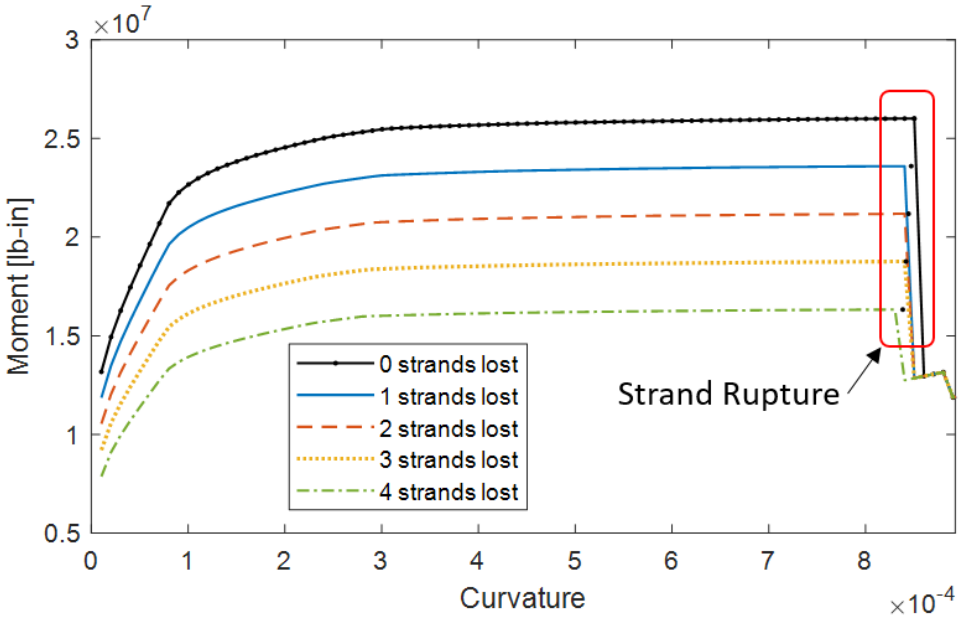

Source: FHWA.

Figure 60. Graph. Moment–curvature relationship for prestressed section with a 50-ft span length and 8-ft girder spacing subjected to loss of prestressing.

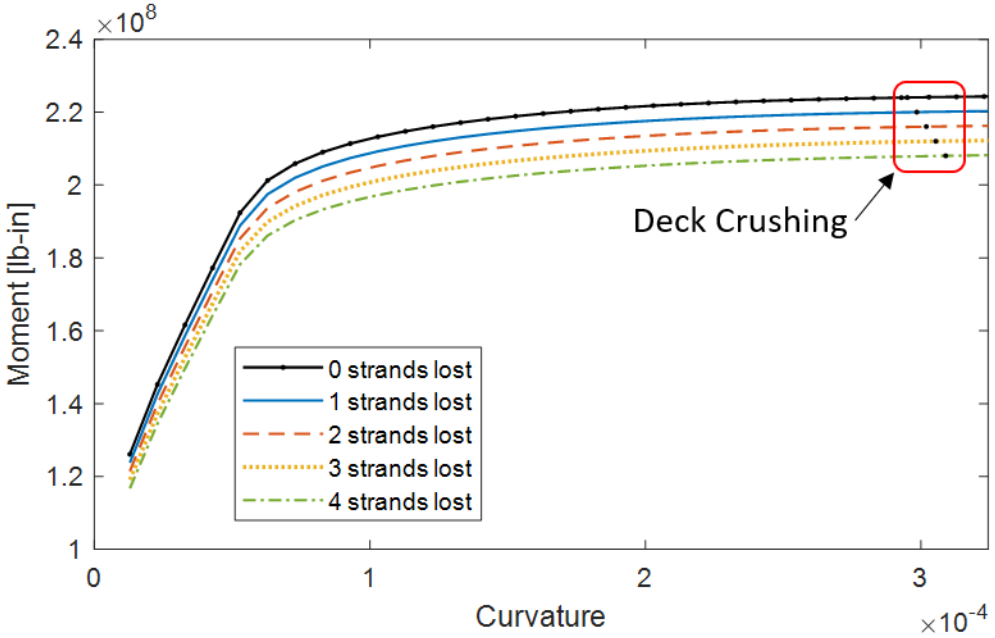

Source: FHWA.

Figure 61. Graph. Moment–curvature relationship for prestressed section with a 150-ft span length and 8-ft girder spacing subjected to loss of prestressing.

The loss of prestressing has a greater effect on those sections with the least number of prestressing strands as the lost strands represented a larger portion of total prestressing.

Figure 62 and figure 63 illustrate the effect of prestressing loss on ultimate moment capacity and the corresponding curvature. While the loss of prestressing serves to reduce ultimate moment capacity, it often results in slightly greater curvature.

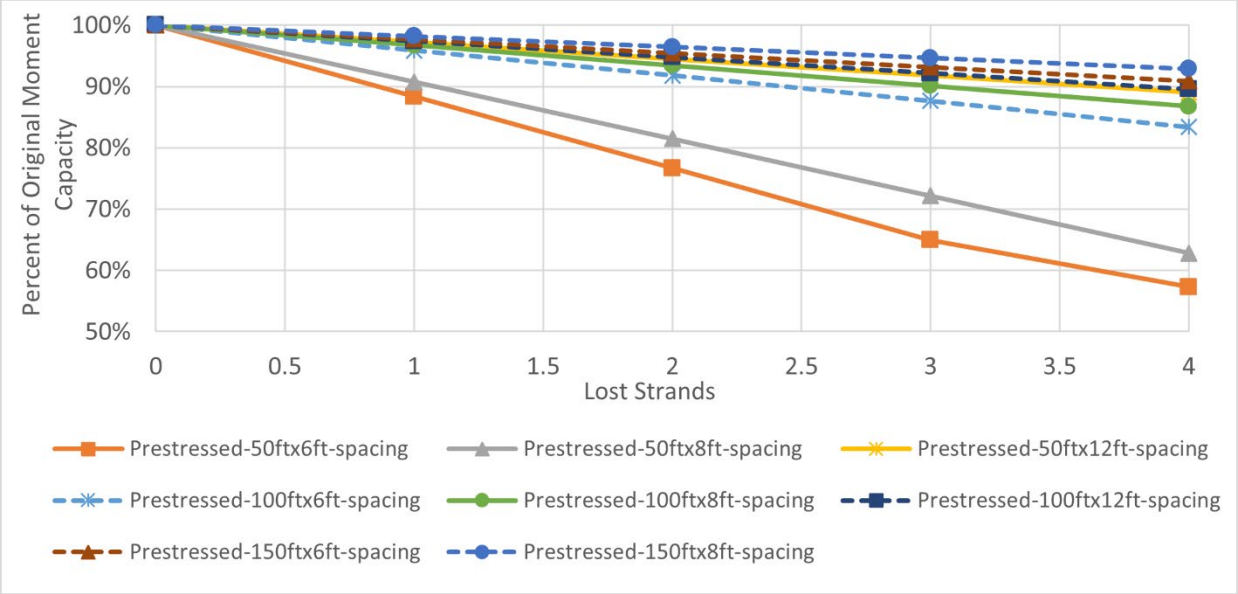

Source: FHWA.
Note: Vertical axis is abbreviated to enable visual discernment of series.

Figure 62. Graph. Effect of loss of prestressing on ultimate moment capacity for composite sections.

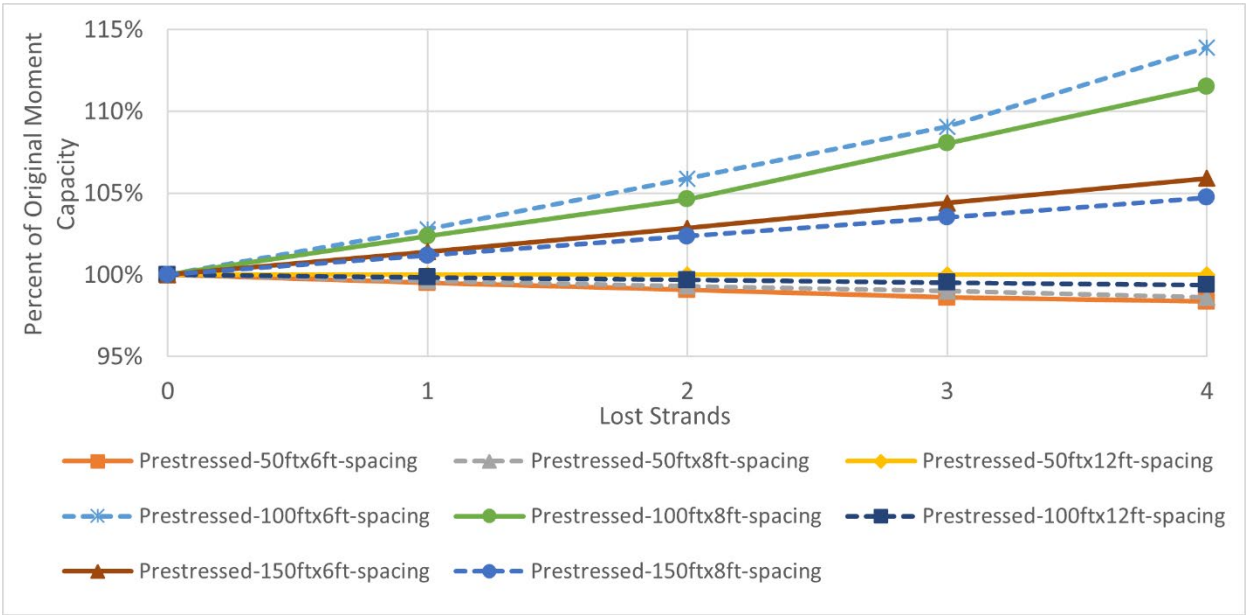

Source: FHWA.
Note: Vertical axis is abbreviated to enable visual discernment of series.

Figure 63. Graph. Effect of loss of prestressing on curvature at ultimate moment for composite sections.

The team also plotted the change in ultimate moment capacity against the percentage of strands that remain active (figure 64), revealing that it is reasonable and conservative to assume that the percentage of remaining moment capacity is equal to the percentage of strands that remain active.

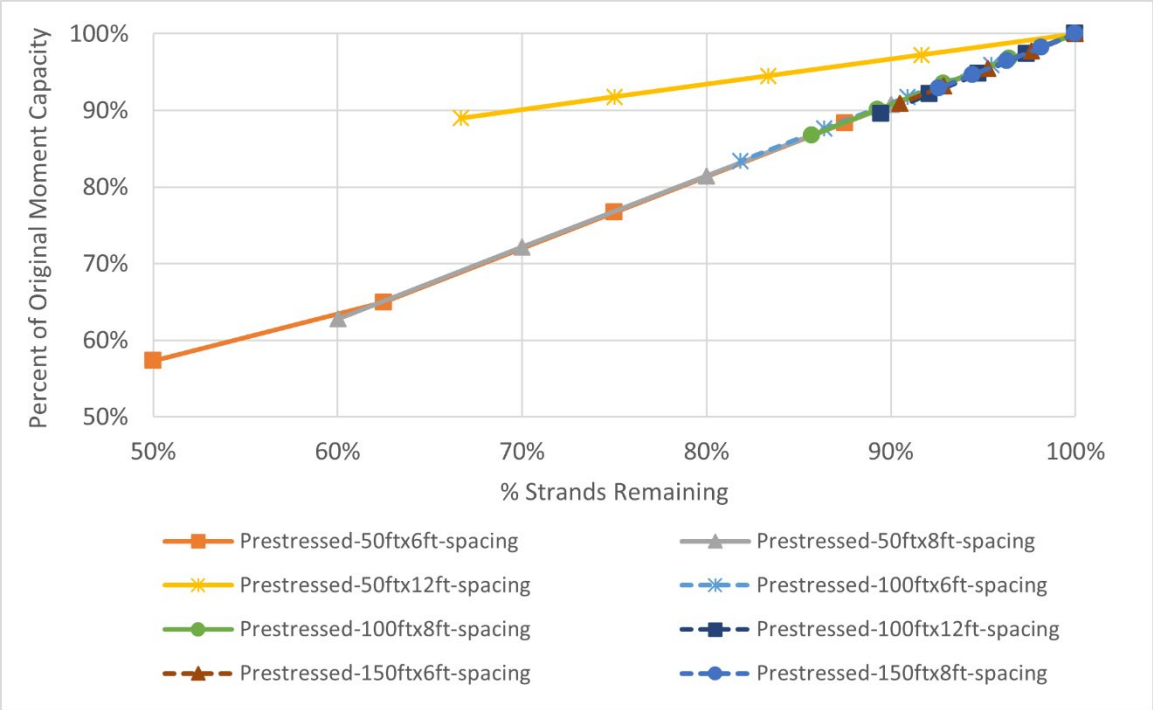

Source: FHWA.
Note: Vertical axis is abbreviated to enable visual discernment of series.

Figure 64. Graph. Relationship between strand loss and change in ultimate moment capacity.

CONCLUSIONS

The research team performed sensitivity studies to evaluate the influence of local deterioration on capacity. The types of deterioration investigated included deck delamination, local loss of composite action (associated with significant deck deterioration), and loss of prestressing strands. The results of investigations are as follows:

- Delaminations reduce capacity but can be adequately accounted for in LRFD calculations by reducing deck thickness. Expected reduction in moment capacity is generally less than 10 percent.

- Loss of composite action reduces the section's stiffness. The change in the capacity limit state (i.e., failure mode) can drastically reduce capacity. Expected reduction in moment capacity is between 10 and 50 percent.

- Loss of prestressing strands is unlikely to significantly reduce the section's capacity. The reduction in capacity may be estimated by the percentage loss of prestressing steel. Expected reduction in moment capacity is between 5 and 15 percent.

- Local deterioration can be accounted for in structural assessments by incorporating reduced section geometry or changes in conditions (e.g., loss of prestressing or composite action) in the existing LRFD capacity equations when computing load ratings.

APPENDIX C. EFFECT OF DEFECTS ON DEMANDS

Sensitivity studies were performed to evaluate the influence of local deterioration on demands. The following types of deterioration were investigated:

- Deck delamination.
- Local loss of composite action (associated with significant deck deterioration).
- Loss of prestressing strands.

For this application, the research team used Strand7 software to develop 3D FEMs. This type of model employs both one-dimensional elements (e.g., beam elements) to model girders and diaphragms, and 2D elements (e.g., plate or shell elements) to model the deck. The team employed beam elements that had six DOF at each node, which permit all translations and rotations and can account for axial, bending, torsional, and shear deformations. To remain consistent with the 3D geometry of the structure, the team also employed various link elements (to connect girders to the deck and diaphragm elements to the girders) and constraints (to simulate boundaries). This model resolution is commonly termed "element level" and is the most common class of 3D FEM employed for constructed systems (Çatbaş Kijewski-Correa, and Aktan 2013). While an element-level FEM may be unable to simulate warping deformation of girders or stress concentrations associated with geometric discontinuities, it can effectively simulate global responses and load distribution.

The research team constructed two element-level FEMs for these sensitivity studies. Steel and prestressed designs were selected from the set used in the previous studies (table 74) with the following characteristics:

- Span length: 100 ft.
- Number of girders: 6.
- Girder spacing: 8 ft.

Figure 65 through figure 68 depict the FEMs and their construction details. Beam and shell elements were meshed to achieve element lengths of 12 inches.

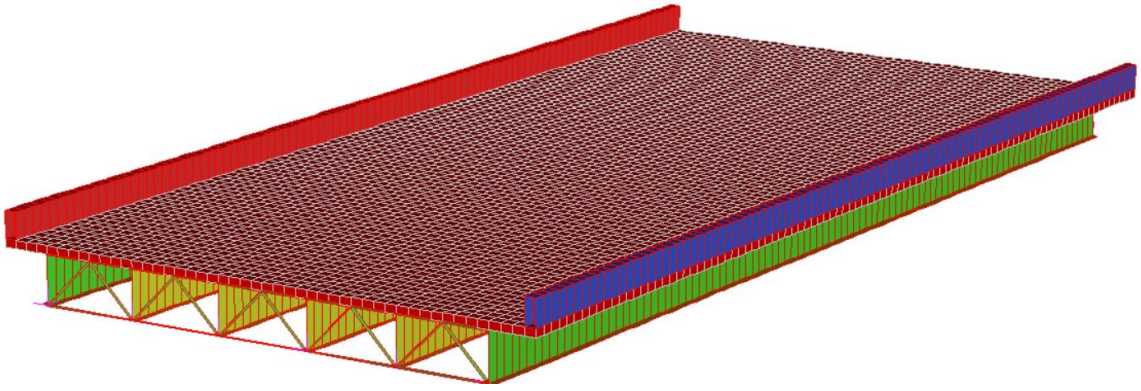

Source: FHWA.

Figure 65. Illustration. 3D FEM for nominal steel design.

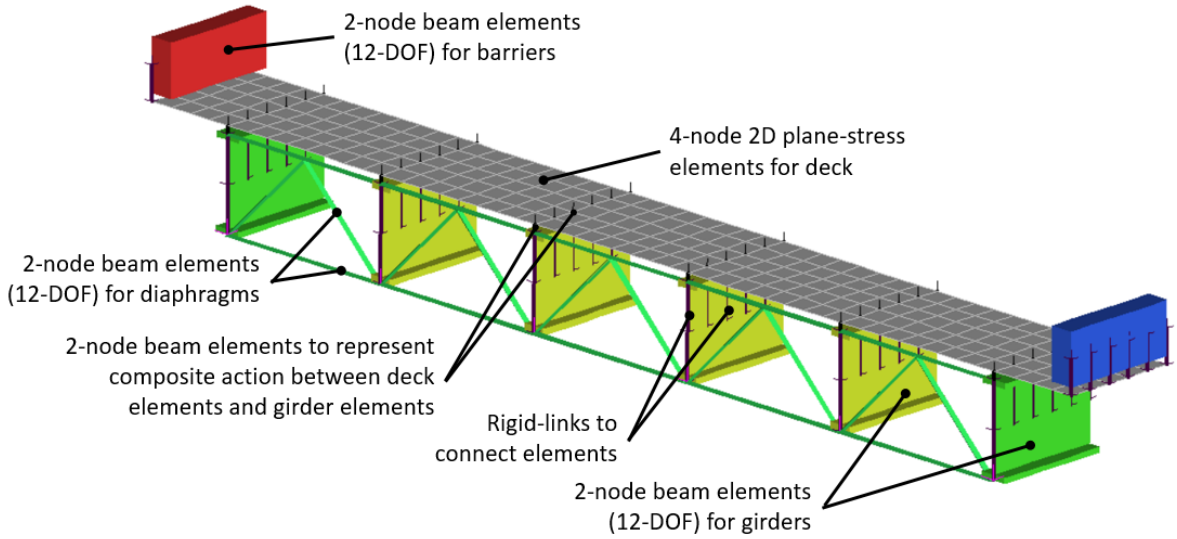

Source: FHWA.

Figure 66. Illustration. Construction detail of 3D FEM for nominal steel design.

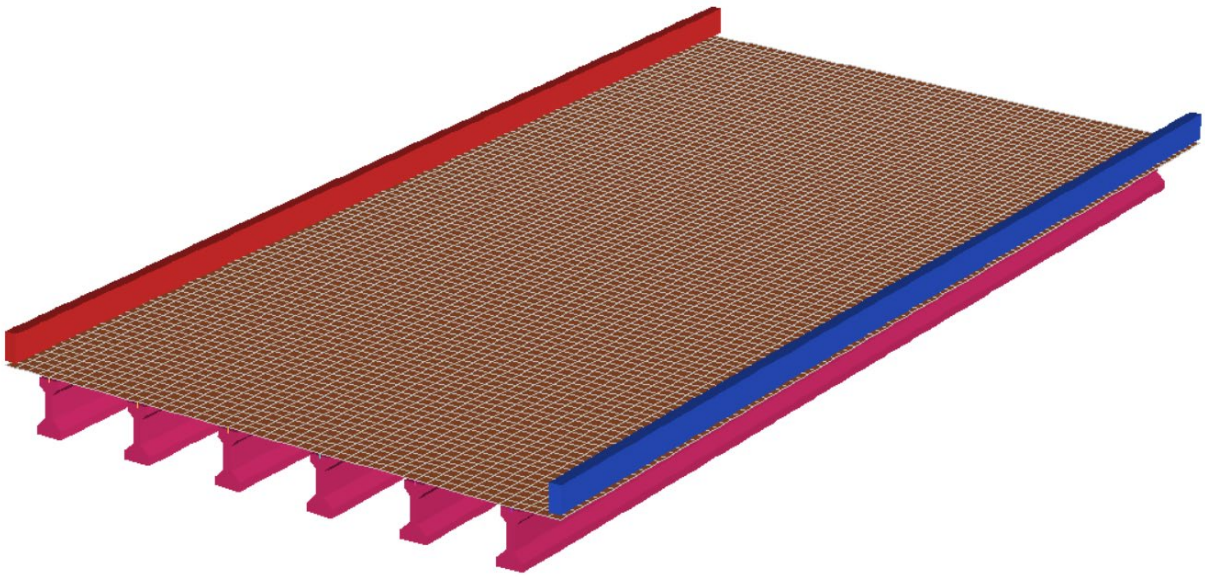

Source: FHWA.

Figure 67. Illustration. 3D FEM for nominal prestressed design.

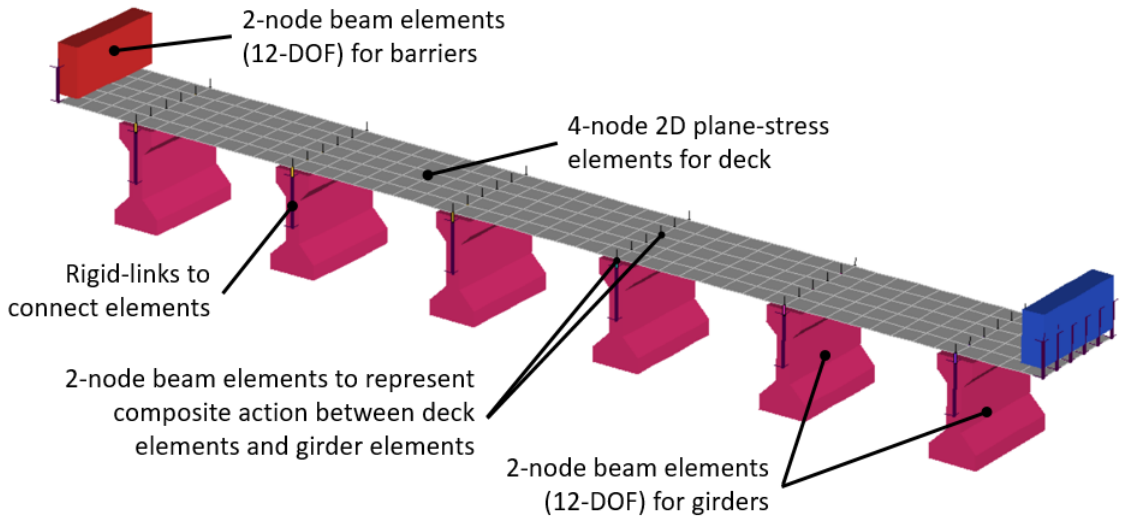

Source: FHWA.

Figure 68. Illustration. Construction detail of 3D FEM for nominal prestressed design.

The research team applied minimal nodal translational restraint at the boundaries to maintain stability of the model, as depicted in figure 8.

Deteriorations were implemented by changing the properties of appropriate elements, including geometry and material properties (e.g., modulus of elasticity).

The team obtained live-load demands by performing a linear static analysis with HL-93 loading positioned to produce maximum responses at the midspans of the girders (AASHTO 2017, section Cl 3.6.1.2).

DELAMINATIONS

The research team implemented delaminations in the FEMs by reducing the thickness of the deck in a localized area by an amount corresponding to the delamination depth. The affected deck elements were also offset by an appropriate amount to ensure the elements were located at the correct elevation.

The team positioned the delaminations over exterior girders (centered), between the exterior and first interior girder, and over the first interior girder (centered). Initially, the team applied delaminations with an 8-ft width and 8-ft length. However, as delaminations of this size had negligible effect on responses, the lengths of the delaminations were increased to 40 ft.

Figure 69 and figure 70 illustrate the effect of the delamination on the composite moment due to controlling live-load cases (HL-93; see AASHTO 2017, section Cl 3.6.1.2).

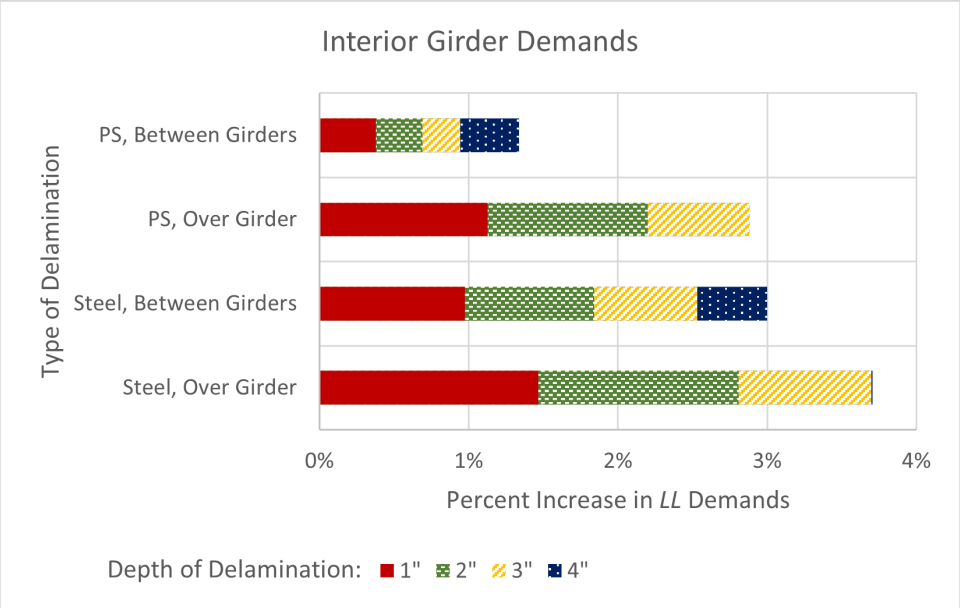

Source: FHWA.
PS = prestressed.

Figure 69. Chart. Effect of delaminations on interior girder demands.

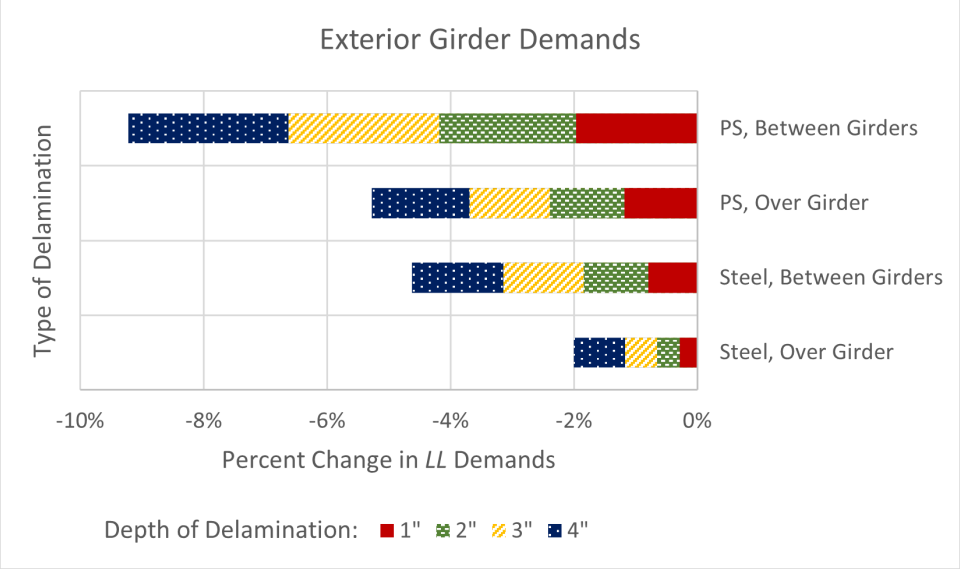

Source: FHWA.
PS = prestressed.

Figure 70. Chart. Effect of delaminations on exterior girder demands.

Delaminations in the region of interior girders serve to decrease lateral stiffness (load transfer to adjacent girders), thereby increasing demands. Loading cannot be placed directly over exterior girders and is therefore loaded by lateral-load-transfer mechanisms. As this lateral stiffness decreases, exterior girder demands also diminish. Therefore, as delamination increases, lateral load distribution capabilities decrease, and exterior girders experience less live load. This effect

is more pronounced with the prestressed bridge since there are no diaphragms, and thus the deck serves as the only lateral-load-transfer mechanism.

LOSS OF COMPOSITE ACTION

The research team implemented loss of composite action in the FEMs by removing the stiffness of elements (links) that enforced longitudinal compatibility between the girder elements and deck elements (figure 71). They did this for subsets of link elements to simulate loss of composite action in different locations. Composite action loss was simulated at the ends of girders and in the middle region. Each affected region had a length equal to one-third of the total span length. The regions extended transversely to cover the tributary area of a single girder (interior and exterior), half of the girders, and over the entire deck width.

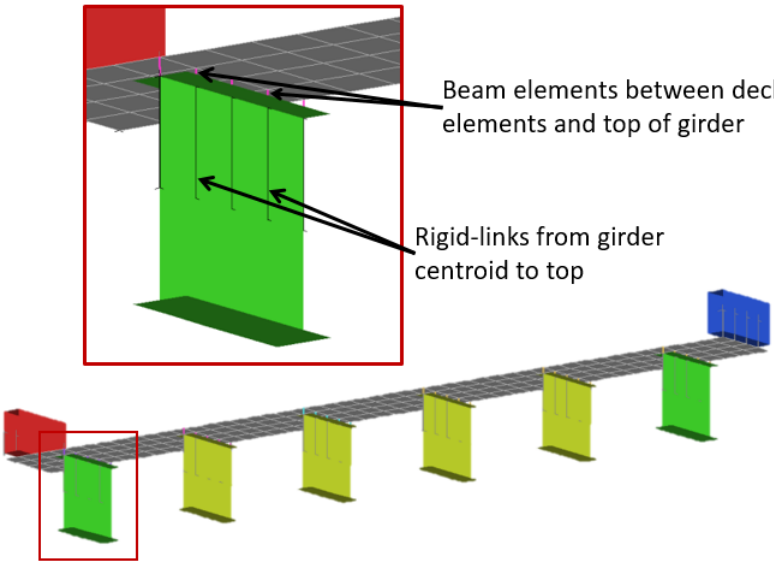

Source: FHWA.

Figure 71. Illustration. Modeling composite action.

Loss of composite action over the midspan region of girders had little effect on demands compared to when loss of composite action occurred at the ends of girders, as depicted in figure 72. This difference in effect is expected since the composite action is the transfer of shear between deck and girder, and shear is at its minimum at midspan.

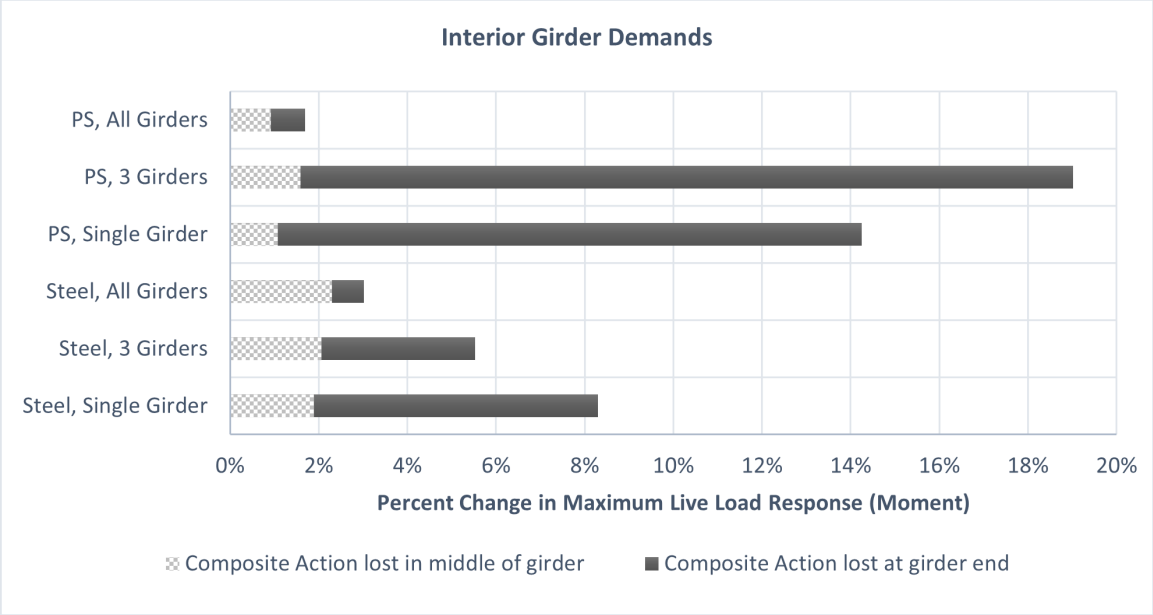

Source: FHWA.
PS = prestressed.

Figure 72. Chart. Effect of local loss of composite action on girder flexural demands.

The loss of composite action serves to shed load from the affected girder to adjacent girders, as seen in figure 73 and figure 74. This effect is most pronounced with interior girders, as there are girders on both sides to which load can be redistributed. Therefore, loss of composite action will generally reduce demands on girders that have lost composite action and increase demands on other girders.

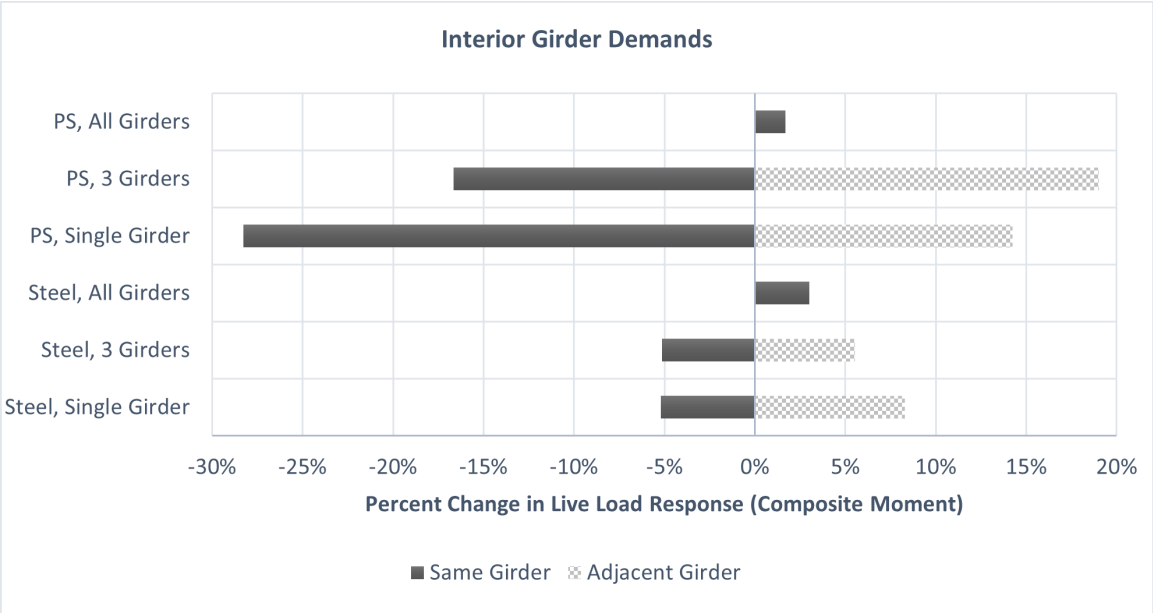

Source: FHWA.
PS = prestressed.

Figure 73. Chart. Effect of loss of composite action on interior girder demands.

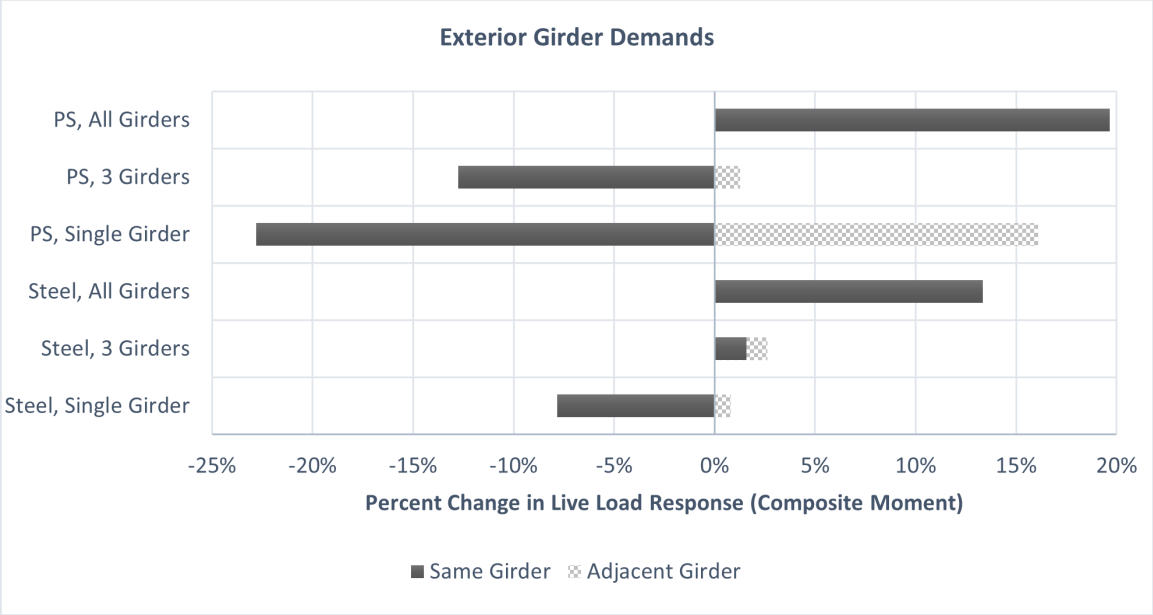

Source: FHWA.
PS = prestressed.

Figure 74. Chart. Effect of loss of composite action on exterior girder demands.

LOSS OF PRESTRESSING STRANDS

The loss of prestressing strands serves to reduce the stiffness of the girder as the corresponding steel area no longer contributes to the section's flexural rigidity. For the purposes of this sensitivity study, the change in flexural rigidity could be determined from the moment–curvature relationships developed for the capacity-sensitivity studies.

The flexural rigidity (*EI*) of the section can be expressed with equation 11:

$$EI = M/\varphi \tag{11}$$

Where ϕ is the curvature that results from an applied moment (M).

EI for a given prestressed section was determined using the secant method on the moment–curvature curve, by which *EI* is calculated by dividing the moment at first yield of the bottom strands (M_y) by the corresponding curvature (ϕ_y), as shown in equation 12:

$$EI = M_y/\varphi_y \tag{12}$$

The research team calculated flexural rigidity for each of the prestressed designs. The following plot illustrates the effect of strand loss on girder flexural rigidity.

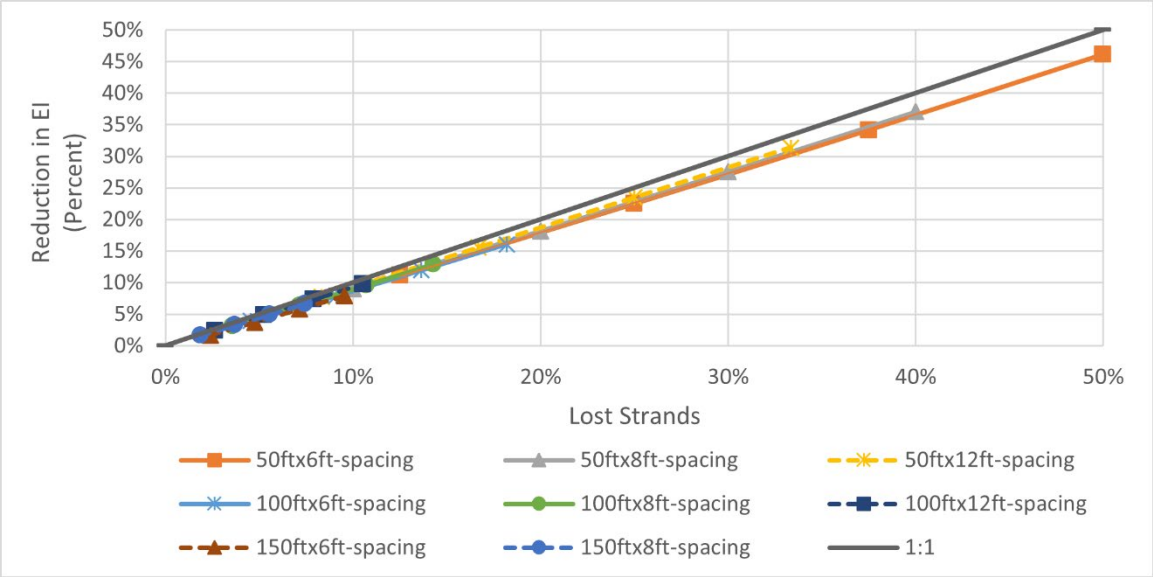

Source: FHWA.

Figure 75. Graph. Effect of loss of prestressing on girder *EI*.

As can be seen in figure 75, the percentage reduction in flexural rigidity can be conservatively estimated as the same percentage reduction in active prestressing strands. Therefore, the team investigated the effect of the loss of prestressing on demands by reducing the flexural rigidity of the girders in the FEM. The modulus of elasticity of the girders was held constant while reducing the moment of inertia. Similar to the results seen for loss of composite action, softening of a girder served to reduce demands in that girder while increasing demands in adjacent girders, as seen in figure 76.

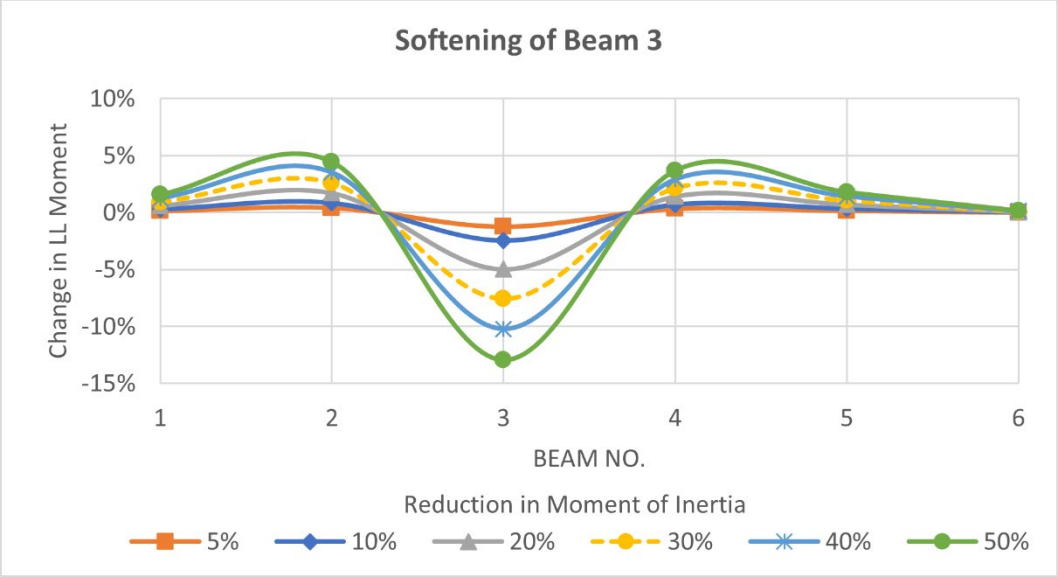

Source: FHWA.

Figure 76. Graph. Redistribution of demands due to loss of prestressing.

Figure 77 and figure 78 present the change in interior or exterior girder demands when that girder is softened or several girders are softened (including that girder whose demands are being presented). These results again suggest that softening a girder serves to reduce demands to that girder.

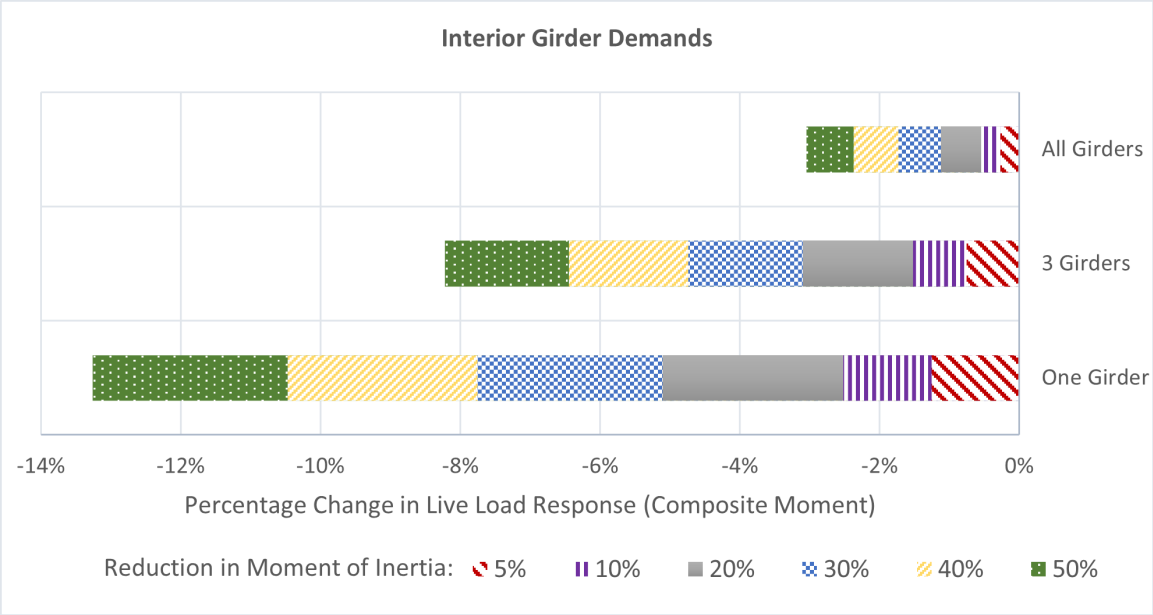

Source: FHWA.

Figure 77. Chart. Decrease in interior girder demands due to girder softening (same).

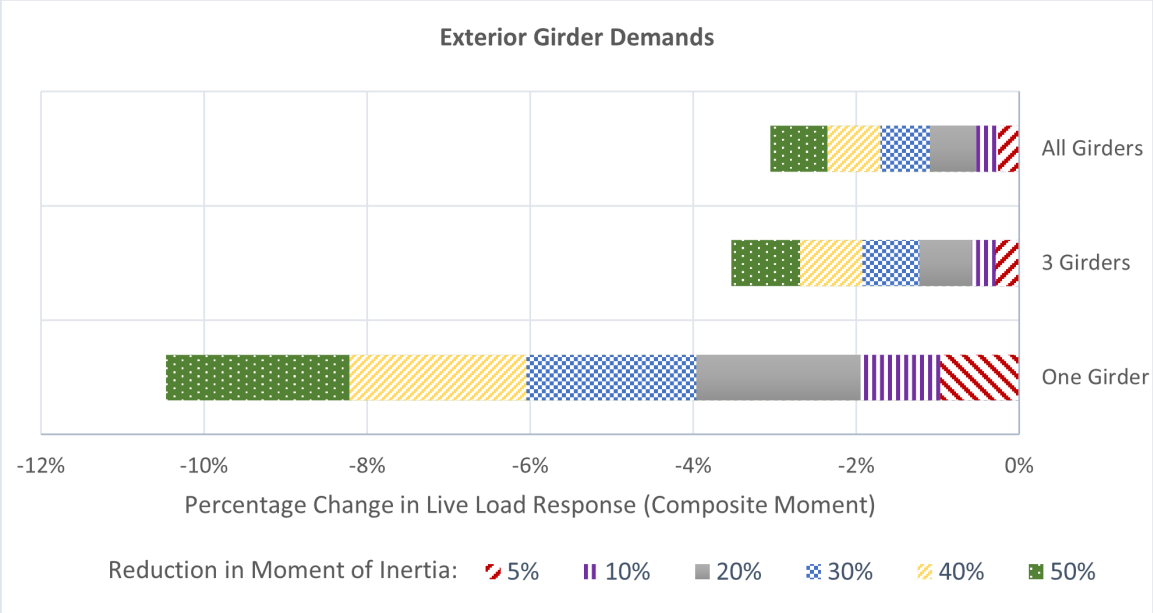

Source: FHWA.

Figure 78. Chart. Decrease in exterior girder demands due to girder softening (same).

The change in demands distributed to an unaffected girder (with full rigidity) when an adjacent girder or multiple adjacent girders experience softening is presented in figure 79.

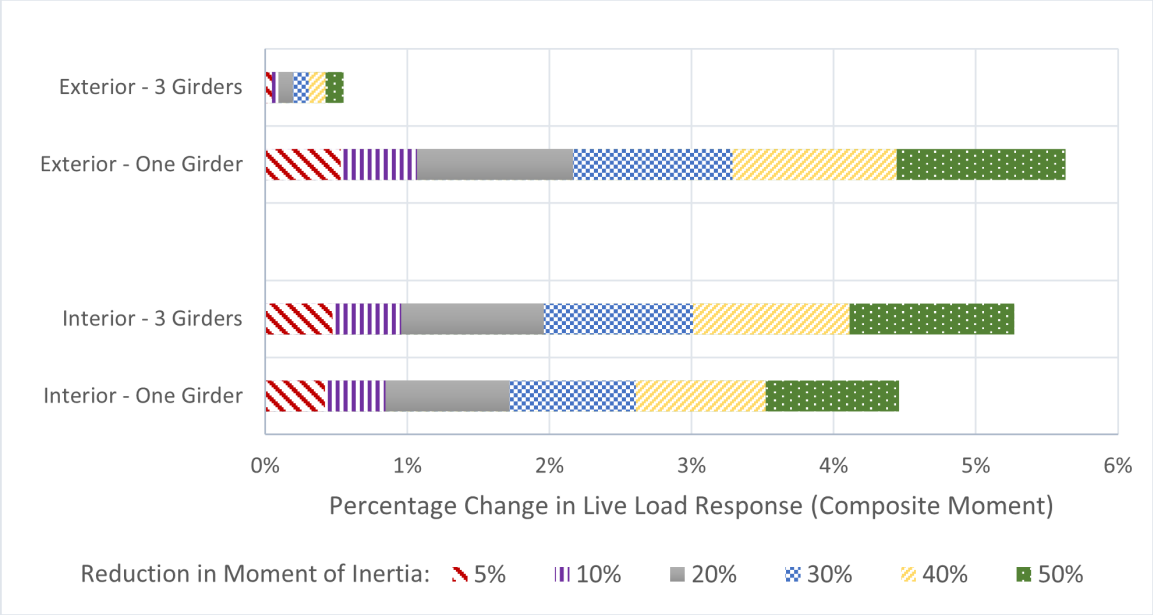

Source: FHWA.

Figure 79. Chart. Increase in girder demands due to loss of prestressing in adjacent girders.

From the previously presented plots, it is evident that even significant softening of girders has little effect on the demands presented to any given girder. Therefore, the effect from the loss of a few prestressing strands does not need to be considered when determining demands.

DYNAMIC AMPLIFICATION

The effect of deck degradation was examined in terms of depth of delamination and how that delamination affected load distribution. However, deck degradation can also affect the surface condition of the deck. Severe wearing and general degradation of the roadway surface can significantly increase the level of dynamic amplification. A poor roadway surface results in increased excitation of a traversing vehicle and, as a result, excites the mass of the bridge.

The magnitude of this dynamic amplification can only be determined by considering the dynamic interaction of vehicle and bridge as a function of the roadway profile.

CONCLUSIONS

Figure 80 summarizes the worst-case effects of deterioration. In many cases, deterioration serves to shift load away from the affected area. In these cases, adjacent girders present the worst-case as they would experience an increase in demands.

Source: FHWA.

Figure 80. Chart. Maximum effect of deterioration on girder flexural demands.

Figure 80 shows that composite action is the only defect that has an appreciable effect on demands. However, loss of composite action softens the longitudinal stiffness of the girder and shifts load to adjacent girders that remain composite. Because the degree of composite action cannot be directly measured, it is recommended that experimental testing or refined analysis with FEM be used to determine the distribution of load when a bridge is suspected to have lost composite action.

The following conclusions may also be drawn from the sensitivity studies:

- Delaminations have little effect (<5 percent) on live-load demands for bridges with other load-transfer mechanisms, such as diaphragms.
- Delaminations tend to decrease demands to exterior girders and increase demands to interior girders.
- Delaminations may have significant effect on exterior girder demands when the deck is the sole source of lateral-load transfer and may decreases demands (<15 percent).
- Loss of composite action reduces longitudinal stiffness and thereby reduces demands to girders in immediate vicinity of composite action loss while increasing demands to nearby composite girders.
- Loss of composite action at girder midspan has negligible effect on demands.
- Loss of prestressing in strands causes a reduction in girder stiffness and minor redistribution of demands (≈5 percent).

Ultimately, local defects and deterioration have relatively minor influence on distribution of live-load demands, and the load distribution in situ is best determined by leveraging SHM techniques. Characterization of local deteriorations is still important for estimating capacity and remaining service life.

REFERENCES

American Association of State Highway and Transportation Officials. *Manual for Bridge Evaluation (MBE),* 3rd ed. Washington, DC: AASHTO, 2018.

AASHTO. *AASHTO LRFD Bridge Design Specifications,* 8th Ed. Washington, DC: AASHTO, 2017.

AASHTO. *AASHTO LRFD Bridge Design Specifications,* 5th Ed. Washington, DC: AASHTO, 2010.

Adams, A., et al. *Manual for Refined Analysis in Bridge Design and Evaluation.* No. FHWA-HIF-18-046, Washington, DC: Federal Highway Administration, 2019.

Alampalli, S., et al. *Transportation Research Circular No. E-C257: Primer on Bridge Load Testing.* Washington, DC: Transportation Research Board, 2019.

Asgarieh, E., B. Moaveni, and A. Stavridis. "Nonlinear finite element model updating of an infilled frame based on identified time-varying modal parameters during an earthquake." *Journal of Sound and Vibration* 333, no. 23 (November 2014): 6057–6073. https://doi.org/10.1016/j.jsv.2014.04.064.

ASTM International. *ASTM C39 / C39M-20, Standard Test Method for Compressive Strength of Cylindrical Concrete Specimens.* West Conshohocken, PA: ASTMI, 2020.

Çatbaş, F. N., T. Kijewski-Correa, and A. E. Aktan. *Structural Identification of Constructed Systems: Approaches, Methods, and Technologies for Effective Practice of St-Id.* Reston, VA: American Society of Civil Engineers, 2013. https://doi.org/10.1061/9780784411971.

Cheung, S. H., and J. L. Beck. "Bayesian Model Updating Using Hybrid Monte Carlo Simulation with Application to Structural Dynamic Models with Many Uncertain Parameters." *Journal of Engineering Mechanics* 135, no. 4 (April 2009): 243–255. https://doi.org/10.1061/(ASCE)0733-9399(2009)135:4(243).

Christodoulou, K., and C. Papadimitriou. "Structural Identification Based on Optimally Weighted Modal Residuals." *Mechanical Systems and Signal Processing* 21, no. 1 (January 2007): 4–23. https://doi.org/10.1016/j.ymssp.2006.05.011.

Dubbs, N. C., and F. L. Moon. "Comparison and Implementation of Multiple Model Structural Identification Methods." *Journal of Structural Engineering* 141, no. 11 (November 2015): 04015042. https://doi.org/10.1061/(ASCE)ST.1943-541X.0001284.

FHWA. *Nondestructive Evaluation (NDE) Web Manual,* v 1.0. Last updated November 3, 2015. Available online: https://fhwaapps.fhwa.dot.gov/ndep, last accessed August 14, 2020.

Goulet, J. A., and I. F.C. Smith. "Predicting the Usefulness of Monitoring for Identifying the Behavior of Structures." *Journal of Structural Engineering* 139, no. 10 (October 2013): 1716–1727. https://doi.org/10.1061/(ASCE)ST.1943-541X.0000577.

Goulet, J. A., P. Kripakaran, and I. F. C. Smith. "Multimodel Structural Performance Monitoring." *Journal of Structural Engineering* 136, no. 10 (October 2010): 1309–1318. https://doi.org/10.1061/(ASCE)ST.1943-541X.0000232.

Hognestad, Eivind. *Study of Combined Bending and Axial Load in Reinforced Concrete Members*. Urbana Champaign: University of Illinois at Urbana Champaign, College of Engineering, 1951.

MATLAB. 8.6.0.958874 (R2015b). Natick, Massachusetts: The MathWorks Inc.

23 CFR 650 Subpart C. "National Bridge Inspection Standards."

Precast/Prestressed Concrete Institute. *PCI Design Handbook: Precast and Prestressed Concrete*, 8th ed. Chicago: PCI, 2017

Strand7. Release 2.4.6. Sydney, Australia: Strand7 Software, 2013.

Recycled
Recyclable

HRDI-20/01-21(WEB)E